

From Medical Radiation Physics Division,  
DEPT. ONCOLOGY-PATHOLOGY  
Karolinska Institutet, Stockholm, Sweden

**PRODUCTION OF HIGH QUALITY  $^{11}\text{C}$   
BEAMS FOR RADIATION TREATMENT AND  
ACCURATE PET-CT DOSE DELIVERY  
VERIFICATION**

Marta Lazzeroni



Stockholm 2013

## **EXAMINATION BOARD MEMBERS**

Docent Anders Montelius, Akademiska sjukhuset, Uppsala, Sweden  
Docent Mark Lubberink, Akademiska sjukhuset, Uppsala, Sweden  
Dr. Cathrine Jonsson, Karolinska Universitetssjukhuset, Stockholm, Sweden

## **OPPONENT**

Prof. Katia Parodi, Ludwig Maximilians University (LMU), Munich, Germany

## **SUPERVISORS**

Prof. Anders Brahme, Karolinska Institutet, Stockholm, Sweden  
Assoc. Prof. Iuliana Toma-Dasu, Stockholm University, Stockholm, Sweden  
Dr. Johanna Kempe, Karolinska Institutet, Stockholm , Sweden

All previously published papers were reproduced with permission from the publisher.

Published by Karolinska Institutet. Printed by Universitets service US-AB

© Marta Lazzeroni, 2013  
ISBN

978-91-7549-267-4

*To Mirko*

## ABSTRACT

Radiation therapy with external beams of positron emitter light ions offers the optimal solution for simultaneously treating and *in vivo* monitoring the delivery of the dose in 3D with Positron Emission Tomography (PET) or PET-Computed Tomography (CT) imaging. Specifically, positron emitter light ion beams merge the main distinctive advantages of light ion therapy, namely a high conformal and biological effective dose delivery to the tumor, an optimal penumbra, and sparing of the surrounding normal tissues, with the advantage of a high  $\beta^+$ -activity signal mainly produced directly by the beam itself, and therefore not primarily dependent on the specific stoichiometry of the body tissues.

The aim of this thesis is to explore a method to maximize the generally low production yield of  $^{11}\text{C}$  ion beams through in-flight fragmentation of a primary  $^{12}\text{C}$  ion beam on a dedicated decelerating target. The thesis provides a practical solution applicable to cyclotron, synchrotron and linac based hospital facilities. The study investigates the main steps from the production of the beam and the transport through the beam optics system to the purification of the beam from other potentially contaminating fragments. Analytical models of transport of ions in matter, as well as the Monte Carlo code SHIELD-HIT were used to conduct the analysis.

The proposed beam line includes a composite production target made of a 20 cm thick liquid hydrogen section followed by a variable thickness section consisting of plane parallel slabs of polyethylene. The first section is selected to maximize the  $^{11}\text{C}$  ion beam intensity, whereas, the second section is used to reduce the beam energy to the desired value, maintaining the high  $^{11}\text{C}$  ion yield. To be able to minimize the energy spread of the beam, and the contamination from other fragments, a variable wedge-shaped degrader and a Time Of Flight (TOF) Radio-Frequency driven velocity filter are included in the beam line together with dipole and quadrupole magnets.

A  $^{11}\text{C}$  ion beam intensity of about 4-6% of the primary  $^{12}\text{C}$  ion beam intensity with radial spot size confined to 0.5 cm in radius, and an energy and angular spread of about 1% and 1°, respectively, are achievable. The  $^{11}\text{C}$  ion beam purity is expected to be about 99%. The proposed system for production of high quality  $^{11}\text{C}$  ion beams contributes to the developments of an accurate PET-CT based dose delivery verification, ultimately aiming towards a biologically optimized adaptive radiation therapy.

## LIST OF PUBLICATIONS

- I. **Lazzeroni M** and Brahme A 2011 Production of clinically useful positron emitter beams during carbon ion deceleration *Phys. Med. Biol.* **56** 1585–1600;
- II. Hultqvist M\*, **Lazzeroni M\***, Botvina A, Gudowska I, Sobolevsky N and Brahme A 2012 Evaluation of nuclear reaction cross sections and fragment yields in carbon beams using the SHIELD-HIT Monte Carlo code. Comparison with experiments. *Phys. Med. Biol.* **57** 4369–85;  
\* Equal contribution, names in alphabetical order
- III. **Lazzeroni M** and Brahme A Effective source size, radial, angular and energy spread of the  $^{11}\text{C}$  beam produced by  $^{12}\text{C}$  fragmentation. *Submitted to Nuclear Instruments and Methods A*;
- IV. **Lazzeroni M** and Brahme A Production of pure quasi-monochromatic  $^{11}\text{C}$  beams for radiation therapy and dose delivery imaging. *Submitted to New Journal of Physics*.

Related work not included in the thesis:

Brahme A, **Lazzeroni M** Positron emitter irradiation system *US-Patent Appl. P861US002011*

# CONTENTS

1	Introduction.....	1
1.1	Summary of papers.....	2
1.2	Contribution to papers.....	4
2	The radiation therapy process.....	5
2.1	Rationale for radiation therapy with light ions.....	5
2.2	Dose delivery verification by means of PET.....	9
2.2.1	The autoactivation method.....	11
2.2.2	On the use of positron emitter beams for treatment.....	19
2.3	Alternatives to PET imaging for treatment verification.....	23
2.4	Biological treatment verification and optimization using PET-CT dose responsiveness imaging.....	25
3	Production of clinically useful positron emitter beams.....	29
3.1	High quality $^{11}\text{C}$ positron emitter beams.....	29
3.2	Radioactive ion beam production methods.....	30
3.3	The selection of the target material from the production efficiency point of view.....	34
3.4	Radial and angular spread of the $^{11}\text{C}$ ion beam as a function of the target material.....	42
3.5	Reduction of the energy spread.....	45
3.5.1	Energy distribution of fragments.....	45
3.5.2	The variable wedge-shaped degrader.....	47
3.6	Beam line design and purification of the $^{11}\text{C}$ ion beam from other contaminating fragments.....	50
3.6.1	Magnetic rigidity filtering.....	52
3.6.2	The Radio Frequency-driven TOF and velocity filter.....	57
4	The Monte Carlo code SHIELD-HIT.....	62
4.1	Nuclear models and Fermi break-up.....	63
4.2	Uncertainties in the production yields of the fragments due to nuclear models in SHIELD-HIT.....	64
5	Discussion and conclusions.....	67
6	Acknowledgements.....	69
7	References.....	71

## LIST OF ABBREVIATIONS

ARTFORCE	Adaptive and innovative Radiation Treatment FOR improving Cancer patients' treatment outcome
BGO	Bismuth Germanate ( $\text{Bi}_4\text{Ge}_3\text{O}_{12}$ )
BIOART	Biologically Optimized in vivo predictive Assay based Radiation Therapy
CATANA	Centro AdroTerapia e Applicazioni Nucleari Avanzate
CERN	Consil Européen pour la Recherche Nucléaire
CT	Computed Tomography
DNA	DeoxyriboNucleic Acid
DoPET	Dosimetry with a Positron Emission Tomograph
ENLIGHT	European Network for Light Ion Hadron Therapy
ENVISION	European Novel Imaging Systems for Ion Therapy
FLUKA	FLUktuierende KAskade
FOV	Field Of View
FWHM	Full Width at Half Maximum
GSI	Gesellschaft für Schwerionenforschung
HIMAC	Heavy Ion Medical Accelerator
HIT	Heidelberg Ion beam Therapy center
HU	Hounsfield Unit
IAEA	International Atomic Energy Agency
ICRU	International Commission on Radiation Units and measurements
INR RAS	Institute for Nuclear Research of the Russian Academy of Science
ISOL	Isotope Separation On Line
JINR	Joint Institute for Nuclear Research
LBL	Lawrence Berkeley Laboratory
LET	Linear Energy Transfer
LOENT	Low Energy Neutron Transport
LOR	Line Of Response
MSDM	Many Stage Dynamical Mode
NIRS	National Institute of Radiological Sciences
OER	Oxygen Enhancement Ratio
PARTNER	Particle Training Network for European Radiotherapy
PET	Positron Emission Tomography
PMMA	PolyMethyl MethAcrylate ( $\text{C}_5\text{H}_8\text{O}_2$ ) <sub>n</sub>
RBE	Relative Biological Effectiveness
RF	Radio Frequency
SHIELD-HIT	SHIELD-Heavy Ion Therapy
SiPM	Silicon Photon Multiplier
SIS	SchwerIonenSynchrotron
SOBP	Spread Out Bragg Peak
TRS	Technical Reports Series



# 1 INTRODUCTION

Radiation therapy of cancer follows a basic principle: delivering a high dose that kills malignant genomic unstable cells yet sparing intact normal cells as much as possible. Hidden underneath this simple and general principle is a high degree of complexity, which requires a close collaboration and the efforts of a large scientific community.

The thesis aims at contributing to the development of accurate PET-CT verification of treatments delivered with positron emitter light ion beams. The investigation conducted in this work resulted in a practical solution, applicable to hospital based facilities, to overcome difficulties related to the low quality and production efficiency of light ion positron emitter beams.

The use of ions as external ionizing radiation for treatment started in the 50's at the Lawrence Berkeley Laboratory (USA), when protons accelerated through a cyclotron were utilized for the first time to irradiate the pituitary gland, in 1954 (Tobias *et al.*, 1958). The increasing interest and rather fast development of the ion therapy at the Berkeley facility resulted in more than two thousand patients receiving treatment with protons, helium, carbon, neon, silicon, and argon ions (Alonso and Castro, 2002; Ma, 2012). Pioneering treatments with protons started soon after worldwide in other institutes: in Uppsala (Sweden) in 1957, at Harvard (USA) in 1961, in Dubna (Russia) in 1967, in Moscow (Russia) in 1969, etc. However, it is not until 1994 that ions heavier than proton, specifically carbon ions, were again used for therapy at the National Institute of Radiological Sciences (NIRS) in Japan and, few years later, at Gesellschaft für Schwerionenforschung (GSI) in Germany (Ma, 2012).

In comparison to conventional therapy with photons and electrons, light ions (from proton to oxygen) potentially offer numerous advantages in the treatment of solid tumors. A higher dose can be delivered to the tumor, while sparing the normal tissues in the entrance channel, a more precisely conformed dose distribution can be administered to the target volume with steeper gradients to the surrounding normal tissues and, not least, for particles heavier than proton, a higher biological effectiveness is achievable, which is especially beneficial for those tumors that are normally radioresistant to conventional treatment. Nevertheless, light ion therapy still remains nowadays an emerging technique, the main reason being the large economic investment required for the hospital care system, lack of knowledge and randomized trials.

Years after the shutdown of the Berkeley facility, some of the questions addressed still remain open and unsolved. For instance, one of the early questions was whether the verification of the treatment could be performed by Positron Emission Tomography (PET) imaging. Two main directions were followed: the verification through the activity generated by the fragmentation of stable beams in the patient (autoactivation) (Tobias *et al.*, 1977) and the verification of the treatment delivered by primary positron emitter beams (Llacer *et al.*, 1979). Both techniques

present their own advantages and limitations, which will be described in the course of this report.

The interest of this thesis is mainly centered on the use of radioactive beams, in particular  $^{11}\text{C}$  particles. Above all, one specific advantage and one limitation of this technique have triggered the idea of this work: the higher activity signal registered by the PET camera (as compared to the autoactivation method) and the difficulty in the production of positron emitter beams suitable for radiation therapy.

The aim of this work is to develop a method to maximize the yield of high quality  $^{11}\text{C}$  positron emitter beams through the in-flight fragmentation method (Kanazawa *et al.*, 2002). Specifically, it aims at selecting the optimal material to increase the yield of  $^{11}\text{C}$  projectile-like fragments, maximize the brilliance of the ion beam and keep the beam emittance as low as possible. Issues related to the minimization of the energy spread of the secondary  $^{11}\text{C}$  ion beam, as well as the purification of the  $^{11}\text{C}$  ion beam from other contaminating fragments have also been addressed.

By the use of a composite target made of a combination of two sections (20 cm of liquid hydrogen followed by polyethylene) a yield of  $^{11}\text{C}$  fragments equal to about 5% of the primary  $^{12}\text{C}$  ion beam can be achieved, with a beam purity of about 99%. The radial spread can be confined within about 0.5 cm of radius, with energy spread of approximately 1% of the mean beam energy.

The beam line proposed in this work includes a variable wedge-shaped filter in a monochromatic configuration to reduce the energy spread of the beam and a Time Of Flight Radio Frequency-driven velocity filter to increase the beam purification level achievable by simple magnetic rigidity separation.

Analytical models of ion transport in matter and Monte Carlo calculations are used to conduct the analysis and achieve the results mentioned.

The thesis is organized as follows: Chapter 2 describes the background of the work by reviewing some of the important steps in the radiation therapy process with light ions; Chapter 3 describes the main achievements of the work; Chapter 4 provides a description of the Monte Carlo code SHIELD-HIT, reviewing the physical models used in the code and the specific modification made to one of the parameters in the nuclear interaction model, which regulates the Fermi Break-up stage; and finally, discussion, conclusions and possible future applications of the work are described in Chapter 5.

## 1.1 SUMMARY OF PAPERS

### *Paper I*

The paper is devoted to the analysis of the production of  $^{11}\text{C}$  fragments by fragmentation of a stable  $^{12}\text{C}$  ion beam in different absorbing materials. The study was based on Monte Carlo calculations performed with the Monte Carlo code SHIELD-HIT07. Analytical calculations of transport of ions in matter were also used to both support and interpret the results. Build-up fluence and mean energy of the  $^{11}\text{C}$  fragments are shown as a function of the depth in the different materials. The maximum  $^{11}\text{C}$  fluence build-up is high in compounds having higher fraction by weight of hydrogen atoms, being the highest for a pure liquid

hydrogen target. The integral  $^{11}\text{C}$  production is about 8% of the incoming  $^{12}\text{C}$  primary ion intensity.

#### *Paper II*

The capability of SHIELD-HIT10 to reproduce total and partial charge changing cross sections (in water and polycarbonate) and thick target yields (in water) was studied for carbon ion beam irradiations. Comparisons with experimental results showed a general overestimation of the yield of lithium and beryllium fragments. The variation of one of the parameter in the Fermi break-up model which regulates the freeze-out volume resulted in better agreement with experimental data.

#### *Paper III*

The description of the secondary beam of  $^{11}\text{C}$  ions generated by the fragmentation of a primary beam of  $^{12}\text{C}$  particles in different targets is given in terms of the radial, angular and energy spread. The study is performed by combining the analytical models of particle transport in matter with simulations performed by the Monte Carlo code SHIELD-HIT<sup>1</sup>. Results showed that a high brilliance of the  $^{11}\text{C}$  ion beam is reached for a target made of a combination of 20 cm of liquid hydrogen followed by a polyethylene section of variable length. The intensity of the produced  $^{11}\text{C}$  ion beam ranges from about 5 to 8% depending on the exit energy and radial acceptance of the beam transport system.

#### *Paper IV*

The paper investigates a technique to maximize the purity and minimize the energy spread of an  $^{11}\text{C}$  ion beam produced by projectile fragmentation of a primary  $^{12}\text{C}$  ion beam in a target. Analytical methods of transport of ions in matter and simulations performed with the Monte Carlo code SHIELD-HIT10<sup>2</sup> were used to conduct the study. Particle yields, as well as energy, velocity and magnetic rigidity distributions of the fragments generated in a composite target (20 cm of liquid hydrogen followed by a variable section of polyethylene) are analyzed. A beam line design including a variable wedge-shaped filter and a Radio Frequency driven velocity filter is proposed. The wide energy and magnetic rigidity spectra can be confined below approximately 1% of the  $^{11}\text{C}$  ion mean value with an expected beam purity of about 99%.

---

<sup>1</sup> The symbol (+) indicates a modified version of the code able to score track length fluence differential in energy and angle.

<sup>2</sup> Ibid.

## 1.2 CONTRIBUTION TO PAPERS

### *Paper I-III-IV*

I performed the analytical and Monte Carlo calculations in the papers and analyzed the results of the simulations. I wrote about 85% of the text in the papers. In Paper IV, the beam line design and most part of its description (Section 2.1) were made by Prof. Anders Brahme.

### *Paper II*

Together with Martha Hultqvist (with equal contribution from both parts), I analyzed the results of the simulations, compared with available data in the literature and wrote the text of the paper, except Section 2.3, which was written by Prof. Alexander Botvina.

## 2 THE RADIATION THERAPY PROCESS

### 2.1 RATIONALE FOR RADIATION THERAPY WITH LIGHT IONS

Radiation therapy with external beams of light ions (i.e. ions with atomic masses  $A \leq 16$  and charge  $Z \leq 8$ ) has seen a very fast increase worldwide in the last few decades. From the very first suggestion of exploiting the favorable dose distributional properties of protons by Robert Wilson dated back in the 1946 (Wilson, 1946), the number of treated patients has exceeded 100 000 (whereof approximately the 87% treated with protons, 10% with carbon ions and the rest with other particles<sup>3</sup>) and an increasing number of planned and built facilities has been registered. The rationale for the increasing interest of the scientific community in light ion therapy lays both in their advantageous dose distributional characteristics and, most importantly, for ions heavier than protons, their increased biological effectiveness.

From a physical point of view, the energy deposition of monoenergetic narrow pencil beam of light ions exhibits a plateau region in the entrance channel followed by a steep raise at the end of the particle range, the Bragg peak (Bragg, 1905; Kraft, 2000). The placement of the Bragg peak could be shifted in depth by energy variation and should mainly be located in the tumor region.

Whereas for the lightest ions from lithium and below, the exit dose (*fragmentation tail*) after the Bragg peak is low and it has mainly a low LET character ( $< 10$  keV/ $\mu\text{m}$ ) (Kempe *et al.*, 2007), for heavier particles it leads to more complexity in treatment planning due to their increasing high LET component in the plateau and tail region (Kempe *et al.*, 2007). The fragmentation tail is due to the contribution of particles having lower mass and/or charge generated during nuclear fragmentation reactions between the incident projectiles and the atoms in the medium, which generally travel longer distances and reach undesired areas beyond the tumor volume. However, contrary to photons and electrons, a monoenergetic ion beam can only be used for a very small tumor, as shown in Figure 1. When a Spread Out Bragg Peak (SOBP) is considered to cover an extensive tumor region, the relative height of the peak-to-plateau ratio is notably reduced as compared to pristine beams (cf. Figure 1) and, at the same time, the dose beyond the distal region is increased. This effect is the direct consequence of SOBP build-up method based on the superimposition of an array of pencil beams modulated in energy. Nevertheless, the tumor control, normal tissue and organs at

---

<sup>3</sup> Mostly helium ions and pions ( $\pi^-$ ).

Data refer to the total number of patients treated with the different ion species and include also statistics of no longer active facilities (e.g. Lawrence Berkley Laboratories, USA). Statistics are update to the end of March 2013 (<http://ptcog.web.psi.ch/ptcentres.html>).

risk sparing are still more advantageous with light ions than with conventional therapy with photons and electrons.

Furthermore, light ions beyond protons have a lateral penumbra of 80-20% that ranges from 1/2 to 1/3 of the one of protons and approximately the half of that of photons (Brahme, 2003, 2009). Interestingly, the lateral penumbra and the range straggling show similar scaling properties characterized by a steep gradient from proton to helium and more flat trend from helium to carbon ions (Kempe *et al.*, 2007). Therefore, the border region between the clinical target volume and the surrounding normal tissues is as narrow as physically possible (Brahme, 2004). As a result, complications linked to the radiation toxicity in normal tissues may generally be reduced (Brahme, 2004).

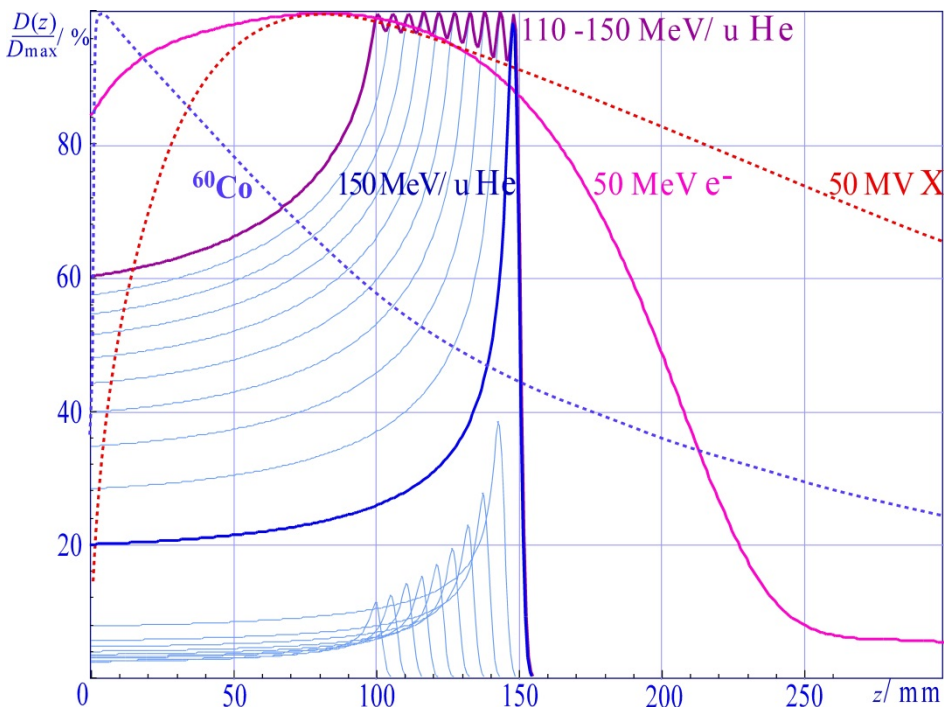


Figure 1 Comparison of the dose distribution (normalized to the dose maximum) as a function of the depth in water for helium ions (110-150 MeV/u), electrons (50 MeV), and photons (50 MV X-rays and  $^{60}\text{Co}$   $\gamma$ -rays). The favorable depth dose profile of light ions allow to deliver higher doses to the tumor while simultaneously better sparing the surrounding normal tissues. Contrary to photons and electrons, the very sharp depth dose profile of a monoenergetic ion beam can only be used for a very small tumor. In order to cover an extended area a superposition of monoenergetic ion beam profiles may be used to get a Spread Out Bragg Peak. As a consequence, the relative height of the peak-to-plateau ratio is notably reduced as compared to pristine beams and, at the same time, the dose beyond the distal region is increased.

Besides the advantageous physical properties, particles with  $Z>1$  accompany the increase in energy loss with decreasing velocity towards the end of the range by an increased biological effectiveness and, most likely, also an increased therapeutic potential. In fact, as compared to sparsely ionizing radiations (such as electrons or photons and also high energy protons), ions above proton show an increase in the local ionization density caused by higher density of low energy electrons that locally transfer their energy to the tissues. Unfortunately, beyond

boron and carbon the entrance region in normal tissues is also exposed to an increased biological effect.

The quantity conventionally used to describe the amount of transferred energy to the medium and, implicitly, the radiation quality, is the Linear Energy Transfer or restricted linear collision stopping power,  $L_A$ . By definition,  $L_A$  is equal to the average energy loss of an ion per path length, minus the sum of kinetic energies of all released electrons having kinetic energies larger than  $\Delta$  (ICRU, 1998). Being the LET a macroscopic concept, its suitability to fully describe the radiation quality is debatable, since the stochastic nature of the energy deposition following radiation interactions is not taken into account. In fact, the radiation quality is strictly related not only to the particle type but also to their energy spectrum (TRS-461, 2008). The differences in effectiveness are related to the differences in energy deposition at the level of the particle tracks and subcellular structures (TRS-461, 2008).

The Relative Biological Effectiveness (RBE) is defined as the ratio between the dose of a reference radiation (usually  $^{60}\text{Co}$  photons) and the corresponding dose of radiation under study resulting in the same effect in a given biological system under identical conditions (TRS-461, 2008). Since the radiobiological properties of protons do not differ markedly from those of photons, a constant RBE of about 1.1 is conventionally used in the clinic. For higher-Z particles instead, a substantial variation is seen. For example, for carbon ions the RBE can be as high as 2.0-3.5. The calculation of variation of the RBE and its applicability is rather complex since it depends on different factors, such as cell or tissue type, radiation energy, fractionation scheme etc. Therefore, whereas on one hand an enhanced biological effectiveness represents an advantage, it also entails an increased level of complexity in its description, particularly, when the fragmentation yields of secondary particles have to be considered. To take into account the increased biological effectiveness, the concept of biological effective dose has been introduced and defined as the product of the RBE and the physical dose. Hence, in order to achieve a uniform biological dose within the SOBP, the increase of the RBE as a function of the penetrating depth should be compensated by a decreased in the delivered dose (IAEA-TECDOC-1560, 2007).

A further advantage in the use of high LET radiation is linked to its reduced dependence on the tumor oxygen level for cell killing, which is beneficial for hypoxic tumors (Barendsen *et al.*, 1966; Chapman *et al.*, 1978; Furusawa *et al.*, 2000). In fact, the biological effect of high LET radiation is less dependent on the activation of the free radical scavengers for inducing damage to the DNA of the cell (Ito *et al.*, 2006; Hirayama *et al.*, 2009), which is considered to be the main radiation target of the cell (Ward, 1998; Kraft, 2000). The induced radiation resistance due to the lack of oxygen is often quantified in terms of the Oxygen Enhancement Ratio (OER), which is defined as the ratio between the doses under anoxic (complete absence of oxygen) and oxic (air,  $p_{\text{O}_2} \approx 20\text{mmHg}$ ) conditions leading to the same biological effect at the atmospheric pressure (Hall and Giaccia, 2006). Usually the threshold for hypoxia is  $p_{\text{O}_2} \approx 10\text{ mm Hg}$  or lower.

The OER is therefore expected to decrease as the LET of the particle increases. For carbon ion irradiation at low LET values (i.e. high energy carbon ion beams),

OER values comparable to those of photons in the range of 2.5-3 have been reported in the literature, while at very high LET ( $> 200 \text{ keV}/\mu\text{m}$ ) the OER is approximately 1 (Furusawa *et al.*, 2000; Antonovic *et al.*, 2013). The OER has been reported to decrease for LET values larger than  $100 \text{ keV}/\mu\text{m}$  (Barendsen *et al.*, 1966; Furusawa *et al.*, 2000). Given their high LET character at the proximal end towards the Bragg Peak, light ions above proton might be the preferred choice in case of treatment of tumors which exhibit macroscopic hypoxic regions and poor re-oxygenation patterns. To optimize the use of particle beams for radiation therapy, the map of the distribution of the oxygen level in the target and its associated radiation resistance would be highly beneficial (Scifoni *et al.*, 2013) and research both on the mathematical modelling, functional imaging and experimental biology side is ongoing.

Experiments with high LET radiation have also shown a reduced sensitivity of the irradiation outcome on the cell cycle phase (Brahme, 2004, 2012). This is an advantage with respect to low LET radiation, for which an increased radiation sensitivity of the cells in the mitosis phase has been reported.

Finally, systematic investigations conducted at the National Institute of Radiological Sciences (NIRS, Japan) seem to indicate that a reduction in the number of fractions with a simultaneous increase in the dose delivered per fraction during a radiation treatment with light ions above protons is possible maintaining the toxicity of the normal tissues under acceptance levels (Schultz-Ertner and Tsujii, 2007; Tsujii and Kamada, 2012). From a more practical point of view, a hypofractionation regime would be desirable since it would not only entail a less discomfort for the patient, but also an easier overall management of the facility. However, a very extreme hypofractionation scheme with a single fraction of large dose might not be optimal. For example, reoxygenation is lost and possible corrections of the treatment would be prevented.

In conclusion, light ions play an important role in the development of the modern radiation therapy with external beams and may represent the optimal tool for the treatment of inoperable, deep sited or located near organ at risk tumors (Kraft, 2000; Brahme, 2009, 2010).

Even though the majority of the scientific community seems to generally agree on the potential superiority of light ion therapy as compared to conventional therapy with photons, it should be mentioned that the debate on the use of low LET and high LET radiation is still open and no clinically randomized trial has been reported. The need of accompanying the technical developments with clinical trials designed to compare protons, carbon ions and advanced photon techniques for selected tumors has been recently discussed by (Combs *et al.*, 2013). For example, at Heidelberg (Germany) major clinical trials have been recently designed and are open (or will soon open) for patient recruitment<sup>4</sup> aiming to compare clinical results of proton and heavier ion treatments under the same irradiation conditions (Schardt *et al.*, 2010).

Most of the clinical experience with light ions concerns protons and carbon ions. However, other particle species (such as, for instance, lithium or boron ions) may

---

<sup>4</sup> More details on the clinical trials identified as NCT01795300, NCT01165671, NCT01166308, NCT01795274, and NCT01528683 are available at <http://clinicaltrials.gov/>.

provide additional clinical advantages as preferable candidates for many treatments (Brahme, 2004, 2009, 2010, 2011). Furthermore, recently, it was suggested that the optimal treatment might be achieved not through the selection of only one single ion specie, but rather by a mixed beam of ions of different species. In fact, based on the past experience of mixed beams of neutrons and photons, it appears that mixed beams of charged particles will help to achieve the desired LET levels for different parts of the target volume. Different light ion dose distribution kernels might in fact be advantageous in different regions of the target volume (Brahme, 2011). In order to achieve a more uniform biological effect distribution in the tumor region, it has been suggested that it may be more advantageous to combine the different ion beams starting with a lower distal LET using, for example, lithium or helium ions and increase the Bragg peak LET towards the anterior part of the tumor using carbon ions, so that a more uniform dose and LET distribution with a smaller variation in the microscopic standard deviation in the energy deposition may be obtained (Brahme, 2011).

## 2.2 DOSE DELIVERY VERIFICATION BY MEANS OF PET

In view of the highlighted physical and biological properties of light ions, it is evident that the calculation of stopping point of both primary and generated secondary fragments in the patient, which corresponds to the maximum energy release and, for ions beyond proton, to an increased biological effectiveness, is one of the key issues. In fact, uncertainties in the beam range calculation could lead to severe deviations in the planned dose distribution with the risk of missing part of the tumor or administering undesired dose to the normal tissues. The mismatch in the calculation of the range of particles in the matter and, in more general terms, of the whole dose delivery distribution may be linked to several sources of error, such as: patient positioning errors, errors at level of the treatment planning algorithm, anatomical changes etc. (Brahme, 2003).

Even though nowadays several approaches and different alternative techniques are under study (Section 2.3), so far, PET is the only *clinically* implemented technique for an *in vivo* and *in situ* non-invasive verification of the treatment. PET or, preferably, PET-CT (Computed Tomography) imaging have the potential of monitoring the variations between the planned dose and the actual dose delivered to the patient.

Conventionally, positron emission tomography is used to image functional processes in the body by mapping the uptake of a radiopharmaceutical tracer in the tissues. According to the composition and associated properties of the tracer, it is in principle possible to image different functional processes in the tissues. For example,  $[^{18}\text{F}]$ FDG,  $[^{18}\text{F}]$ FLT,  $[^{18}\text{F}]$ FMISO are some of the possible radiopharmaceutical tracer, which could be used to study the glucose metabolism of the cell, cell proliferation, and hypoxia, respectively. PET tracers are constituted by a biologically active molecule labeled with a  $\beta^+$ -emitter isotope. In brief, following the nuclear decay, the positron emitted by the radiotracer undergoes annihilation with an electron after travelling a distance of few tens of a

mm to a few mm in the tissues and, from this process, a pair of approximately collinear back-to-back 511-keV photons are emitted. The nearly simultaneous tomographic detection of these photons by detectors operating in coincidence (within a certain time window) and the use of imaging reconstruction algorithms allow to determine the spatial distribution of the activity in the area of interest and give a visual representation and quantification of the underneath biological processes.

As mentioned above, PET imaging could also be applied in a non-conventional way for range verification and, potentially, imaging the dose delivery distribution during a radiation therapy treatment with external beams of light ions (Enghardt *et al.*, 1999; Enghardt, 2004; Enghardt *et al.*, 2004) or high energy photons (above 20 MV) (Janek *et al.*, 2006; Müller and Enghardt, 2006; Strååt *et al.*, 2013a; Strååt *et al.*, 2013b).

The rationale behind the use of PET imaging for light ion therapy is related to the impossibility of using electronic portal imaging methods as in case of conventional radiation therapy with photons, due to the fact that the primary radiation is fully stopped in the patient. Thus, it is necessary to detect the secondary radiation emerging from the patient, in this case, as *delayed*<sup>5</sup> radiation from the decay of positron emitter nuclei.

The experimental validation of the treatment delivery is essential since the treatment planning algorithms calculate the range of the particles in the matter based on an empirically determined conversion from the CT-Hounsfield Units (HU), and this calibration process might be a non-negligible source of uncertainties. CT-HUs reflect the attenuation of X-rays in the medium, which is strictly connected to the electron density of the medium, and to be used for the calculation of the corresponding particle range, they are mapped into water equivalent path lengths or relative range in water. The uncertainties arising from this procedure might be as high as 3-5% or even more for particular situations of major dosimetric concern (e.g. metal implants, strong density gradients such as in bone or lung, which have respectively very high or very low density as compared to the rest of the tissues) (Jäkel, 2011).

The efforts of the scientific community during the years have been directed towards two main research directions having as a common final aim the assessment of the dose delivery distribution from the inspection of the activity distribution via PET imaging. The former method is the so called *autoactivation* method (Tobias *et al.*, 1971), while the latter is related to the use of radioactive ion beams for treatment. An overview of both methods is given in the section 2.2.1 and 2.2.2, respectively. Both of the treatment verification strategies were initiated in the 70's at Lawrence Berkeley Laboratory (LBL), and further developed, after the shutdown of the LBL facility, in several other institutes.

---

<sup>5</sup> The term *delayed* is here used as opposed to the term *prompt* used in section 2.3 to classify and distinguish the possible different techniques for monitoring the delivery of the treatment (Schardt *et al.*, 2010).

### 2.2.1 The autoactivation method

*From the nuclear fragmentation to the activity curve*

The term *autoactivation* indicates the production of radioactive nuclei in a thick target by an incident beam of stable ions (Tobias *et al.*, 1971; Schardt *et al.*, 2010).

When light ions penetrate the tissues of the patient, they may undergo nuclear interaction processes with the nuclei of the target atoms, which can arise either as central collisions, peripheral<sup>6</sup> collisions or other Coulomb barrier induced processes (such as Rutherford scattering, Coulomb excitation, nucleon transfer by tunneling) according to the beam energies and impact parameter values. For impact parameters smaller or comparable with the sum of the radii of the target and projectile nuclei, central collision or peripheral collisions take place. In the central collisions, a large energy amount and transverse momentum are transferred and the projectile breaks in many fragments of lower velocity (Raju, 1980). In contrast, in peripheral collisions the incident particle interacts primarily with the surface of the target and as a result a few nucleons may be stripped from the nuclei of the interacting atoms (Raju, 1980). In the energy domain of radiation therapy (approximately from 80 to 430 MeV/u), the peripheral collisions are the most frequent nuclear interactions, while the central or near central collisions represent approximately the 10% of the nuclear fragmentation (Crespo, 2005). The fragmentation of the projectile is generally predominant (Raju, 1980).

Fragmentation reactions may result both in charge-changing and neutron-removal reactions. Fragments having mass heavier or equal to boron have positron emitter isotopes, which are likely to be created during the primary beam deceleration in the target. The amount of generated positron emitters and their type depend both on the stoichiometric composition of the tissue and on the interaction cross sections between the incoming nuclei and the target nuclei.

Projectile-produced fragments are characterized by a velocity that is approximately the same of the primary particles and they are mostly forward direct in a narrow cone. On the contrary, target-produced fragments have a velocity that is almost null and, as consequence, they approximately remain where they are generated (Greiner *et al.*, 1975; Morrissey, 1989; Schall *et al.*, 1996).

The kinematics characteristics of the reactions are reflected in the shape of the activity signal registered with the PET camera. Thus, in case of particles with charge  $Z \geq 5$ , the resulting activity signal registered by the PET camera is the superposition of a prominent maximum at a depth approximately corresponding to the range of projectile-like fragments with an activity background due to the target-like fragments produced all along the penetration depth of the primary particles (Enghardt *et al.*, 1999; Enghardt, 2004). The activity induced by positron emitter target-like fragments retains information about the transit of the beam in the medium and on its lateral spread. Since at the same velocity the fragment range scales approximately as the ratio between the masses of the fragment and

---

<sup>6</sup> Peripheral collisions are also sometimes called in the literature glancing collisions, see for example (Tobias *et al.*, 1977; Raju, 1980).

primary particle (Fiedler *et al.*, 2006), due to the similar mass, the range of, for example,  $^{11}\text{C}$  ions is slightly shorter than the one of the corresponding primary  $^{12}\text{C}$  ions.

In a  $^{12}\text{C}$  ion irradiation, the pronounced peak is mainly due to  $^{11}\text{C}$  and  $^{10}\text{C}$  projectile-like fragments. On contrary, due to the lack of projectile fragments, the pronounced peak at the end of the ion range is not seen in the proton activity curve. Therefore, the range verification for a proton beam irradiation has an intrinsic additional difficulty due to the nature of the process itself. Nevertheless, the activity curve distal fall-off almost coincides with the primary proton range. In case of proton irradiation the activity distribution is characterized by a rather flat region, which drops down 2-13 mm water equivalent before the particle range (Nishio *et al.*, 2005; Parodi and Bortfeld, 2006). The shift between the physical range and the activity distribution range is due to the reaction cross section threshold for production of positron emitter fragments.

The main advantage in the use of the autoactivation method is that it exploits the byproduct of the therapeutic irradiation performed with stable light ion beams and no extra dose needs to be administered to the patient.

The mean dose-related activity density for different beams irradiating a PMMA block is reported in Table 1. Experimental data for the stable ion beams ( $^1\text{H}$ ,  $^3\text{He}$ ,  $^7\text{Li}$ ,  $^{12}\text{C}$ ,  $^{16}\text{O}$ ) are taken from (Priegnitz *et al.*, 2008), while data for hard bremsstrahlung spectrum of photons generated by 50 MeV electrons result from Monte Carlo simulations with the GEANT4 code (Agostinelli *et al.*, 2003; Allison *et al.*, 2006) and are taken from (Müller and Enghardt, 2006). More details on the irradiation conditions are given in the mentioned publications.

Estimated dose-related activity density for positron emitter beam irradiations with  $^{10,11}\text{C}$  ions are also reported for comparison. The estimate is performed by scaling the dose-related activity density of the fragment of interest with the dose-related activity density of  $^{12}\text{C}$  particles. The difference in particle fluence for the same dose due to the different stopping power of the particles and the difference in the half-life of the fragments were included in the calculation. An uncertainty of about 30% was considered in the estimates based on the  $^{12}\text{C}$  ion uncertainty reported from the experiments.

Estimated data on  $^{10}\text{C}$  and  $^{11}\text{C}$  ions are in agreement with experimental investigation by the Japanese group at NIRS, reporting about  $30\,000 \text{ BqGy}^{-1}\text{cm}^{-3}$  for  $^{11}\text{C}$  ion irradiation and about  $450\,000 \text{ BqGy}^{-1}\text{cm}^{-3}$  for  $^{10}\text{C}$  ion irradiation (Yamaya *et al.*, 2012a; Yamaya, 2013).

For the stable beams, the highest activity is registered in case of an irradiation with protons (Table 1). The reason for the almost three fold increased activity density of protons as compared to carbon ions is related to the higher fluence required for the same delivered dose (Parodi and Enghardt, 2000; Parodi *et al.*, 2002). As seen in Table 1, the irradiation with positron emitter beams results in orders of magnitude increase with respect to an irradiation with stable carbon ions. The activity concentration for a conventional  $^{18}\text{F}$ -FDG PET imaging is on the order of  $10^3$ - $10^5 \text{ Bqcm}^{-3}$  (Fiedler *et al.*, 2011). For example<sup>7</sup>, the brain uptake is on

---

<sup>7</sup> The mentioned uptake levels are estimated at about one hour after the tracer administration for an administered activity of about 4 MBq/Kg (Staaf, 2013).

the range between  $1 \cdot 10^4$ - $4 \cdot 10^4$  Bqcm $^{-3}$ , whereas the gluteus maximus muscle tissue or lung tissue have activity concentration in the range between  $1 \cdot 10^3$ - $4 \cdot 10^3$  Bqcm $^{-3}$ . Tumors of the lung can lie in the span of  $10^4$ - $10^5$  Bqcm $^{-3}$ .

Dose-related activity density /Bq cm $^{-3}$ Gy $^{-1}$			
$^1\text{H}$	$^3\text{He}$	$^7\text{Li}$	$^{10}\text{C}$ (*)
$6600 \pm 2100$	$5300 \pm 1000$	$2500 \pm 1500$	$300\,000 \pm 100\,000$
$^{11}\text{C}$ (*)	$^{12}\text{C}$ (*)	$^{16}\text{O}$	Photons (from 50 MeV e $^-$ , hard)
$20\,000 \pm 6\,000$	$1\,600 \pm 510$	$1030 \pm 130$	$3000 \pm 450$

Table 1 Comparison of the dose-related activity density produced in a PMMA target by different primary beams. Experimental data for the stable ion beams ( $^1\text{H}$ ,  $^3\text{He}$ ,  $^7\text{Li}$ ,  $^{12}\text{C}$ ,  $^{16}\text{O}$ ) are taken from (Priegnitz *et al.*, 2008), while data photon beam irradiation result from Monte Carlo simulations with the GEANT4 code (Agostinelli *et al.*, 2003; Allison *et al.*, 2006) and are taken from (Müller and Enghardt, 2006). More details on the irradiation conditions are given in the mentioned publications. (\*) Data for  $^{10,11}\text{C}$  ions are estimated based on scaling of the activity with respect to the activity of the  $^{12}\text{C}$  ion irradiation.

The verification of the treatment delivery based on the  $\beta^+$ -activity generated through the autoactivation method is hampered due to both the low production of  $\beta^+$ -emitters, and issues related to the image acquisition and reconstruction. In fact, only a small percentage of the stable incoming primary beam is converted in target- or projectile-like positron emitter fragments depending on the tissue composition and on the value of partial nuclear reaction cross sections (Parodi, 2004). Moreover, the acquisition time of the PET images also largely affects the resulting quality of the images. In order to achieve a reasonable statistics, it might be needed to increase the imaging time after the end of the irradiation. Depending on the type of technology implemented (e.g. In-beam, Off-beam, In-room PET), the acquisition time varies considerably and it might be as long as 25-40 minutes for Off-beam PET (Fiedler *et al.*, 2011; Shakirin *et al.*, 2011). A long acquisition time unavoidably entail blurring of the images due to the washout of the activity. Furthermore, the geometry of the detector (and its efficiency) also affects the quality of the results, because of the possible loss of decay events due to the detection efficiency below the ideal 100% and also in reason of the related imaging artifacts.

It should be mentioned that issues connected with the image acquisition and reconstruction are common to any treatment delivery verification method with the use of PET imaging and they are not exclusive of the autoactivation method. The low  $\beta^+$ -activity signal issue, however, is intrinsically related to the autoactivation process itself and it may be solved by the use of positron emitter beams for treatment, as described in the following section (Section 2.2.2 and cf. Table 1). Moreover, the detector efficiency problem may also become an issue of second order importance if  $\beta^+$ -emitter ions are used as primary beams for the irradiation.

Yet, technical improvements in the sensitivity of the PET cameras and, particularly, the possibility of using Time of Flight PET with superior time resolution (from the typical time window of the order of several nanoseconds common to the vast majority of conventional PET scanners to the sub-nanosecond regime) could improve the PET image quality by notably increasing the signal-to-noise ratio in the images. In fact, a sub-nanosecond precision indirectly implies a higher PET sensitivity, since the positron annihilation location can be restricted to a confined area along the line-of-response of the detector. The Time of Flight imaging with fast scintillating crystals (e.g. LaBr<sub>3</sub>,  $\approx 10^{-11}$  s) coupled, for example with position sensitive photomultipliers or solid state Silicon Photon multipliers (SiPMs) would allow from one side speeding the reconstruction algorithms by reducing the number of iterations required to calculate the emission point and from another side it would also allow to discriminate the background activity by reducing the volume of interest (Dauvergne *et al.*, 2009). Several projects are ongoing within the ENLIGHT (European Network for Light Ion Hadron Therapy)<sup>8</sup> and ENVISION (European Novel Imaging Systems for Ion Therapy) collaborations, in order to overcome the challenges associated with the technical implementation of fast TOF detectors.

#### *Biological washout of the activity*

The clearance of the positron emitter activity due to biological processes, such as the blood flow, is an important issue in PET imaging. This process is one of the main sources of blurring in the reconstructed PET images and it contributes to degrading the spatial correlation between the activity and the delivered dose. The lack of knowledge of the chemical species that might be generated during the transport of positron emitter nuclei within the tissues prevents the use of compartment analysis commonly used in diagnostic PET, where the injected compound has, on the contrary, a specified chemical form (Tomitani *et al.*, 2003). Moreover, the difficulty in modelling the activity washout is also increased by the heterogeneity of the perfusion in the different tissues. For example, bone structures, fat tissues, or large hypoxic tumors are generally low perfused areas, while lung or liver are generally blood rich organs. However, since solid tumors very often contain a hypoxic core, the verification of the particle range through the detection of the Bragg peak region (which should coincide with the target) is expected to be less affected by the perfusion issues with respect to other areas. This has clearly a positive impact on the feasibility of the treatment delivery verification (Strååt *et al.*, 2013a). Recent investigations with In-beam PET measurements in carbon ion irradiation have confirmed that the biological half-life of the  $\beta^+$ -activity was higher for higher dose levels coinciding with the poorer perfusion patterns of the tumor region (Fiedler *et al.*, 2008).

Experimental investigation of the deposited activity as a function of the time after an irradiation with positron emitter <sup>11</sup>C and <sup>10</sup>C beams were conducted at NIRS (Japan) for the brain and tight muscle of the rear leg of both live and dead rabbits.

---

<sup>8</sup> <http://enlight.web.cern.ch/>

The images were acquired both with a full ring PET camera with 3D-acquisition capability 10 minutes after the irradiation and with a positron camera (consisting of two Anger cameras) located *in situ*, which allowed starting the acquisition immediately after the delivery of the dose (Tomitani *et al.*, 2003). The measurements indicated that a three component analysis might be used to model the biological clearance of the activity through the use of exponential functions with fast, medium and low decay constants (with half-lives for the thigh muscles 2s, 140s, and 3 175s and half-lives for the brain 10s, 195s, 10 191s) (Mizuno *et al.*, 2003; Tomitani *et al.*, 2003). Mizuno and co-authors ascribe the presence of three different components to different physical processes. They speculate that the initial fast component might be due to the fast blood flow, the medium component to the microcirculation via interstitial fluid and the slow component to a trapping of the radioactive ions by stable molecules of the tissues, which are slowly metabolized (Mizuno *et al.*, 2003). However, these hypotheses require further experimental verification to be confirmed. The modelling of the functional processes described by Mizuno and colleagues was also applied for the first time into the clinical framework by (Parodi *et al.*, 2007) in a comparison between measured patient data with Monte Carlo calculated PET imaging after proton irradiation. The verification of the proton range was possible within 1-2 mm of accuracy provided that the functional process were taken into account.

Further investigations on the washout of the activity with the new In-beam Open PET prototype (see following section) are ongoing at NIRS (Japan). The studies at the Japanese facility concern irradiations with  $^{10}\text{C}$  ions of brain and tight muscle of rats (Yamaya *et al.*, 2012b).

#### *Technologies and methods for PET verification of the treatment*

Concerning the practical implementation of the PET imaging verification of the treatment, three different scenarios are commonly envisaged: In-beam, In-room, and Off-beam PET (Fiedler *et al.*, 2011; Shakirin *et al.*, 2011). In the first case, the PET acquisition is performed online with a camera integrated in the irradiation site. The detection is performed simultaneously to the irradiation or more specifically, for a synchrotron based facility, during the pauses between the beam spills in order to discriminate from the noise generated by random coincidences (Parodi *et al.*, 2002). In the two other cases the acquisition is performed, respectively, after approximately 60 s with a PET scanner located very close to the irradiation site and 10-30 min after the end of the irradiation with a PET or PET-CT camera, which can conveniently be the one normally used for diagnostic purposes (Fiedler *et al.*, 2011; Shakirin *et al.*, 2011).

The determination of the optimal solution is still under debate. Several factors besides the image quality need to be taken into account, such as installation costs, influence of the detection modality in the workflow of the facility, as well as the accelerator typology (Shakirin *et al.*, 2011). A comprehensive investigation and comparison between In-Beam and Off-Line (i.e. both In-room and Off-beam) PET for proton and carbon ion irradiation taking into account also the different accelerator system scenarios (cyclotron or synchrotron based facilities) is given in

(Parodi *et al.*, 2008). This study showed the advantage of using In-beam PET with respect to Off-line PET and reported that the ratios between the number of decays available with In-beam and Off-line PET were at least in the range of 40-60% for cyclotron based facilities and in the range from 65-110% and 94-166% for synchrotron installations delivering protons and carbon ions, respectively (Parodi *et al.*, 2008), and even higher including the biological wash-out in the calculations.

Besides being highly costly (about 5 times higher than a conventional PET scanner (Shakirin *et al.*, 2011)), the In-beam irradiation technique is also technically challenging. The current clinically available In-beam PET installations had to come to a compromise and renounce to the presence of a full ring PET scanner, which would have interfered with the beam direction and patient setup. The new Open-PET geometry proposed by the Japanese group at NIRS has been designed to overcome these difficulties by using two PET ring detectors separated by a gap that allows the ion beam to enter and gives the possibility of a full 3D reconstruction of the images, not achievable by the limited geometry cameras (Yamaya and Inaniwa, 2010; Yamaya *et al.*, 2011). The proof-of-principle with a small Open PET prototype (110 mm of ring diameter and 41 mm of gap) of the feasibility of the technique has given positive inputs for further developments of new alternative geometrical arrangements. For example, a small prototype of a single-ring Open-PET consisting in two ellipse-shaped detector rings slanted by 45° and staggered to obtain an open space of 74.5 mm width was recently proposed (Tashima *et al.*, 2012).

Despite the difficult implementation, the unavoidable reconstruction artifacts due to the limited Field of View (FOV), and the consequent loss in sensitivity, the In-beam PET technology still offers the best image quality, since it is least affected by the biological wash-out problems (Fiedler *et al.*, 2011) and it allows the acquisition of signal from short-lived isotopes (such as  $^{15}\text{O}$  ions, which represents about the 60% of an average human body (ICRU, 1992; Straåt, 2012)). Moreover, the In-beam PET allows the verification of each single irradiation field at a time. This is advantageous, for instance, for the range verification of nearly opposing treatment fields, which is one of the most challenging cases.

The Off-line solution has the advantage of being a less costly technique and it offers the possibility of using combined PET-CT scanners, which would add invaluable morphologic information. However, the loss of the signal from short-lived positron emitters and the biological clearance highly affect this method.

In-room PET is a compromise between the two mentioned techniques. It benefits from a closed ring scanner and the counting statistics loss has been estimated to be around 50% of the In-beam case (Shakirin *et al.*, 2011).

So far, the only facility where the implementation of autoactivation method has been extensively investigated in the clinical routine with a dedicated In-beam double-head PET scanner is GSI (Germany). From December 1997 to July 2008, treatment delivery verification with PET imaging was performed on more than 440 patients (Enghardt *et al.*, 1999; Enghardt, 2004; Fiedler *et al.*, 2008; Schardt *et al.*, 2010). The new German facility, the Heidelberg Ion Beam Therapy Center has not followed the footsteps of the GSI institute and an Off-line solution was preferred. A commercial PET-CT scanner is installed in a room located in

proximity of the irradiation room, where the patient can be transported via a shuttle system.

Other facilities, which have investigated the autoactivation method On-line, are located in Japan and specifically, at NIRS in Chiba and at the National Cancer Center Hospital East in Kashiwa. At the Hyogo Ion Beam Medical Center an Off-line verification of the treatment with a full ring scanner was instead preferred. In Italy, the Centro di AdroTerapia e Applicazioni Nucleari Avanzate (CATANA) specifically devoted to the treatment of ocular pathologies with proton beams has developed an In-beam PET prototype of reduced dimensions (the so called DoPET, Dosimetry with a Positron Emission Tomograph (Attanasi *et al.*, 2010)). In USA, where only the proton treatment is available, the autoactivation method has been investigated at the University of Florida Proton Therapy Institute in Jacksonville and at the Massachusetts General Hospital in Boston. Both facilities use the Off-line technique. A review of the technology implemented at the various institutes mentioned above is given by (Fiedler *et al.*, 2011).

So far, no In-beam PET scanner has been used at cyclotron based facilities.

#### *Treatment delivery verification*

The fundamental problem associated with the treatment verification during light ion therapy is related to the fact that the  $\beta^+$ -activity generated during light ion irradiation and the correspondent dose are correlated, but they cannot be directly compared. The relationship between the two mentioned quantities is primarily complicated by the different nature of the underlying physical processes. The dose originates at the atomic level from electron-ion interactions, while the activity is the result of ion-nucleus interactions (Fiedler *et al.*, 2008).

A dedicated procedure based on the Monte Carlo method was developed at GSI and it was routinely used for the indirect verification of the treatment via PET imaging. The method relies on the comparison between the measured PET activity and the PET activity simulated by the Monte Carlo code POSGEN (Ponisch *et al.*, 2004) on the basis of the dose retrieved from the treatment planning system. By taking also into account the time course of the irradiation, this technique was used to monitor the maximum ion range, verify the lateral field position, and detect local changes in the patient anatomy or possible errors in the CT Hounsfield units conversion (Parodi, 2004; Schardt *et al.*, 2010).

The first step in the GSI iterative procedure consists in the visual comparison between the measured and Monte Carlo predicted image. The visual comparison of the images performed by trained clinicians and physicists is, however, rather time consuming and low in reproducibility. The development of automatic or semi-automatic solutions would be highly beneficial and the feasibility of the method is under study phase (Helmbrecht *et al.*, 2012). When deviations between the measured and predicted PET images are observed, hypothesis are formulated on the possible source of the inconsistencies and a new potentially correct CT is generated by a dedicate code. For example, CT modifications may consist of recalculation in the Hounsfield Units in case a change in the density is conjectured. Positioning errors may be corrected by rotating and shifting the CT

map with respect to the treatment planning isocenter. In the next step, the activity distribution is re-calculated on the basis of the new hypothesized CT. The process is iteratively perpetuated until a satisfactory agreement is achieved. The following step consists in the calculation of the dose distribution corresponding to modified CT and the particle fluence administered to the patient as reported by the treatment plan. Finally, the initial and recalculated doses are subtracted in order to determine the discrepancies, which have to be accounted for in the following treatment fractions (Enghardt *et al.*, 2004).

The prediction of the activity distribution by the Monte Carlo code is done by modelling both the particle yields and the photon detection process. A database of measured activity distribution in a PMMA target is available for each of the energies available at the synchrotron. This information corroborated by the data on the fluence and energy of the injected beam extracted from the treatment planning, and the density and stoichiometric information of the tissue extracted from the CT, serve as a base to reconstruct the activity for each specific patient case (Enghardt *et al.*, 1999). More information on the actual implementation of the code is given by (Ponisch *et al.*, 2004).

A retrospective clinical evaluation of the results obtained from the GSI pilot project was conducted in order to assess the accuracy of the treatment delivery verification by Monte Carlo methods. Detection of the errors in the range calculation showed high values of sensitivity and specificity (sensitivity about 91-92% and specificity about 96%) for a 95% confidence interval (Fiedler *et al.*, 2011).

Despite the good results obtained with the Monte Carlo iterative method, the ideal approach for the quantification of the dose on the bases of the activity distribution would be analytical.

The possibility of analytically calculate the PET-activity from the treatment planning dose (*direct approach*) would allow to compare it with the measured  $\beta^+$ -activity distribution, so as to verify that the treatment has been correctly delivered. This method could be used as an alternative (or complement) to the Monte Carlo method, which is not free from uncertainties in the modeling of the interaction and transport of particles in the matter or in reproducing the treatment planning engine (Parodi and Bortfeld, 2006). The relationship between the dose ( $D_{\text{TPS}}$ , dose extracted from the Treatment Planning System) and activity,  $P_{\text{calculated}}$ , might be mathematically described by the use of a filtering approach, whose derivation was given by (Parodi and Bortfeld, 2006):  $P_{\text{calculated}}(z) = D_{\text{TPS}}(z) * f(z)$ . Thus,  $P_{\text{calculated}}$  could be compared with  $P_{\text{measured}}$  or  $P_{\text{MC}}$  from Monte Carlo. The same relation holds also if the dose is derived from measured data  $D_{\text{measured}}$ ,  $P_{\text{calculated}}(z) = D_{\text{measured}}(z) * f(z)$ , as demonstrated for both monoenergetic beams and SOBP proton irradiation of PMMA blocks by (Attanasi *et al.*, 2008).

The filter function  $f$  is conveniently defined as the convolution of a Gaussian and a power law functions (a special class of functions named the  $Q_v(z)$ -functions). The filter is unique for a given activation channel, independent of beam energy and specific target. Comparisons of calculated PET activity distribution with Monte Carlo prediction have shown a very good agreement below 1 mm of

accuracy for both phantom and head and neck tumor patients (Attanasi *et al.*, 2011).

The *inverse approach*, namely the derivation of the dose from the PET activity, requires the solution of an inverse ill-posed problem (Hadamard, 1902):  $D_{\text{calculated}}(z) = P_{\text{measured}}(z) * f^{-1}(z)$ . In proton therapy, promising results were recently shown (Remmelle *et al.*, 2011), however, this issue has not been fully solved yet. The main problem has been identified in being related to the poor quality of the measured PET images having a low signal-to-noise-ratio, even if deblurring algorithms and regularization techniques are used in order to obtain a stable solution. The developed method has given good results for inhomogeneous phantom irradiation using the Monte Carlo simulated PET activity (Remmelle *et al.*, 2011). However, when measured data are considered (independently of being phantom data or real patient data) the low quality of the images make the dose reconstruction being very degraded and affected by many artifacts (Remmelle *et al.*, 2011). In fact, the regularization techniques applied to the measured images allows finding a stable solution of the deconvolution problem, but they cannot compensate for artifacts (Remmelle *et al.*, 2011).

In the case of protons, the method has been so far only limited to one single beam irradiation. It has not been possible yet to separate the components in the PET signal related to the contribution coming from different beams (Remmelle *et al.*, 2011). Furthermore, the biological washout of the positron emitters in the tissue through the vasculature system is an important issue for the method because of the severe dislocation of the original activity (Oelfke *et al.*, 1996; Litzenberg *et al.*, 1999).

### 2.2.2 On the use of positron emitter beams for treatment

In the medical radiation physics field, the use of radioactive beams has been primarily proposed as an alternative to overcome the difficulties arising from the low activity PET signal observed with the autoactivation method (cf. Table 1). The main advantage in the use of positron emitter beams is that the resulting activity distribution is no longer primarily dependent on the stoichiometry of the tissue and related cross sections for production of positron emitters, since the main contribution to the activity comes from the primary beam itself.

Experimental investigations of a primary stable beam of carbon ions in water reported by the GSI group (Germany) have shown that at 400 MeV/u about the 30% of the primary particle reaches the Bragg peak depth, whereas at 200 MeV/u the number of primaries reaching the Bragg Peak is about the 70% (Haettner, 2006). Similar figures also apply to a primary  $^{11}\text{C}$  ion beam irradiation. In a  $^{12}\text{C}$  beam the projectile fragmentation peak due to  $^{11}\text{C}$  production is below the 1% (Kempe, 2008; Sommerer *et al.*, 2009). Therefore, the use of a primary beam of  $^{11}\text{C}$  ions results in a notably higher  $\beta^+$ -activity with respect to an irradiation with stable  $^{12}\text{C}$  ion beam (Kitagawa *et al.*, 2001; Tomitani *et al.*, 2003; Shirai *et al.*, 2009).

At the present time, the main contribution in the study of radioactive beams comes from the NIRS facility (Japan), where intensive experimentation on plastic targets and head phantoms, as well as on animals has been reported (Kitagawa *et al.*, 2001; Tomitani *et al.*, 2003; Shirai *et al.*, 2009; Yamaya *et al.*, 2011; Yamaya *et al.*, 2012a; Yamaya *et al.*, 2012b). However, it should be underlined that results on the irradiation of patients with positron emitter beams have not yet been reported by the Japanese group.

Experimental studies designed to primarily focus on the investigation of the biological washout of the  $^{11}\text{C}$  activity on rabbit tight muscle irradiation with both  $^{12}\text{C}$  and  $^{11}\text{C}$  ions showed that the autoactivity was roughly 1/30 of the one resulting from an irradiation with a primary  $^{11}\text{C}$  ion beam, for the same dose. Expectations from Monte Carlo simulations of the  $^{11}\text{C}$  yields in simple geometries were on the order of 1/50 (Tomitani *et al.*, 2003). However, it should be mentioned that since the fragmentation reactions take place not only in the target, but also in the intervening materials upstream the target, the ratio of the autoactivity to the  $^{11}\text{C}$  implanted activity is dependent on the configuration of irradiation setup of  $^{12}\text{C}$  beams and the 1/30 figure should be considered as a rough estimate (Tomitani, 2013). Therefore, the mentioned Monte Carlo and experimental results are not directly comparable, but they both substantially confirm increased activity levels.

Furthermore, results on an irradiation of head phantom followed by an acquisition with PET-CT imaging for both  $^{12}\text{C}$  and  $^{11}\text{C}$  ion irradiation for 1Gy of delivered dose have shown that the higher signal-to-noise ratio is also accompanied by a higher absolute activity maximum (Shirai *et al.*, 2009).

Figure 2 shows Monte Carlo calculations with the SHIELD-HIT10 code (Chapter 4) of the positron emitter yields generated by a monoenergetic and monodirectional primary  $^{12}\text{C}$  ions ( $E_{\text{mean}}=350.7$  MeV/u) (a) and  $^{11}\text{C}$  ions ( $E_{\text{mean}}=370$  MeV/u) (b) in a water target ( $R_w \sim 22.3$  cm). The total yield of positron emitters (solid line) and the total yield excluding short-lived oxygen fragments (dashed line) are also reported. Convolution of the total positron emitter yield with Gaussian functions having Full Width at Half Maximum (FWHM) 2, 4, and 8 mm are also presented in the figure to account for the finite resolution of the PET images. The background level is estimated to be about  $N_{\text{back}}/N(0) \approx 0.0018$  for both the  $^{12}\text{C}$  and  $^{11}\text{C}$  ion irradiation (horizontal dotted line in the figure). The specificity to image the Bragg Peak for the  $^{11}\text{C}$  ion beam irradiation with respect to the  $^{12}\text{C}$  ion beam irradiation is 11.5, 8.8 and 6.2 fold for 2, 4, and 8 mm of FWHM the Gaussian function, respectively. If no Gaussian filtering is applied the value increases to 16.4 fold.

The use of radioactive beams for range verification prior treatment was also tested at GSI for an irradiation with  $^{19}\text{Ne}$  ions of 406 MeV/u of initial energy on a PMMA phantom. Results showed that the particle range calculated by Gaussian fit of the centroid of the reconstructed distribution could be calculated with rather high precision for less than a thousand of detected events (e.g.  $\bar{R}^{^{19}\text{Ne}} = 141.06 \pm 0.46$  mm for 500 events,  $\bar{R}^{^{19}\text{Ne}} = 141.51 \pm 0.29$  mm for 1000 events). However these values may be significantly reduced in a real patient.

Besides the increase in the registered activity, the use of radioactive isotopes of lower mass is generally advantageous with respect to the corresponding stable

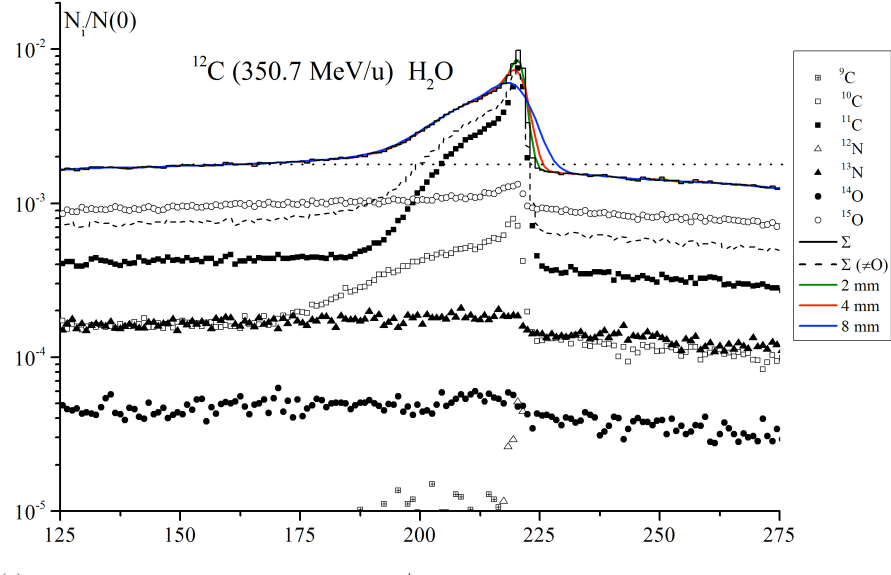
ions due to their reduced fragmentation tail and lower LET in the entrance channel region (Kempe, 2007, 2008).

Considering the importance of treatment verification, some of the ions are potentially more interesting than others. Ions from lithium to carbon are most interesting because they have the least detrimental biological effect on normal tissues for a given biological effect in the target volume (Brahme, 2010), since they combine a sufficiently high LET in the tumor and a low LET in the entrance and fragmentation tail region. Nitrogen and oxygen are less desirable from these points of view. Nonetheless, from the treatment accuracy and verification point of view, ions from boron to oxygen are of special interest, since they have positron emitting isotopes:  $^8\text{B}$ ,  $^{9,10,11}\text{C}$ ,  $^{12,13}\text{N}$  and  $^{15}\text{O}$ . For these reasons, boron and carbon ions seem to be the optimal candidates for radiation therapy. However, further research is required to draw any strong conclusion.

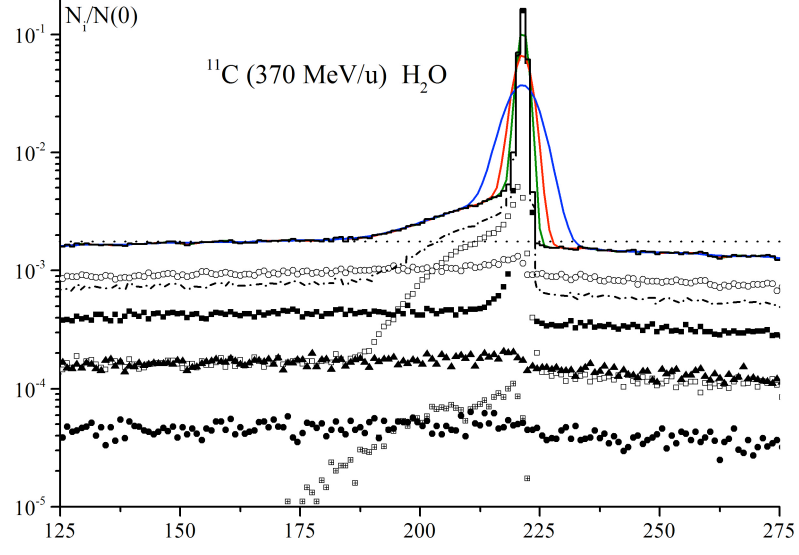
Another advantageous characteristic of  $^8\text{B}$  and  $^{9,10}\text{C}$  ions is clearly related to their faster decay time equal to 770 ms, 19.29 s, and 127 ms, respectively, which consequently implies a higher efficiency in consideration of the activity washout when performing an On-line verification of the treatment.

Furthermore, the expected increase in the effectiveness of  $^8\text{B}$  and  $^9\text{C}$  ions for treatment, which should be linked to their delayed emission of low energy proton and alpha particles ( $^8\text{B} \rightarrow ^8\text{Be} + \beta^+ \rightarrow 2\alpha$ ;  $^9\text{C} \rightarrow ^9\text{B} + \beta^+ \rightarrow ^9\text{Be} + p \rightarrow 2\alpha + p$  (55.6%),  $^9\text{C} \rightarrow ^5\text{Li} + \alpha \rightarrow 2\alpha + p$  (44.4%)), was rather recently questioned (Li *et al.*, 2003; Li *et al.*, 2006; Kempe, 2007; Mancusi *et al.*, 2009). In fact, microdosimetric Monte Carlo calculation have evidenced that the decay of  $^9\text{C}$  contributes little to the energy deposition distributions and also the biological effect of the decay seemed to be negligible, which is in contradiction with previous interpretation of the measured data (Mancusi *et al.*, 2009).

Radioactive beams can have several applications in the medical field. They can be both used as probing beams of low intensity and delivering a low dose for range verification prior treatment with stable ions (Chatterjee *et al.*, 1981; Iseki *et al.*, 2004) or for a complete radiation treatment in case of tumor close to organ at risk and critical dose localization (such as the pituitary or small intraocular tumors or tumors abutting the spinal cord). Further applications of the radioactive beams have been proposed through the years. As mentioned in the previous section, the short-lived radioactive beams can be used to study the metabolic or flow rate in the tissue by injecting a “bolus” of positron emitters in a particular region of the body. This technique was tested at LBL with beams of fast decaying  $^{19}\text{Ne}$  ions (half-life  $\approx 17.26$  s) (Tobias *et al.*, 1977; Llacer *et al.*, 1979). The implantation of the radioactivity by  $^{19}\text{Ne}$  ion beams in the carotid artery of a live dog to map the blood flow was tested by (Llacer *et al.*, 1984a) and further studies were also performed by the NIRS group. As previously described,  $^{11}\text{C}$  (half-life  $\approx 20.33$  min) and particularly  $^{10}\text{C}$  ions (half-life  $\approx 19.29$  s) were used to envisage and develop an empirically based model for activity washout (Mizuno *et al.*, 2003; Tomitani *et al.*, 2003). In addition, they might find application in the chemistry field for tracing hot atoms reactions or fast synthesis of radiopharmaceuticals (Tobias *et al.*, 1977).



(a)



(b)

Figure 2 Comparison of positron emitter yields produced by an irradiation of a water target with a monoenergetic and monodirectional  $^{12}\text{C}$  ion beam ( $E_{\text{mean}} \approx 350.7 \text{ MeV/u}$ ) (a) and a  $^{11}\text{C}$  ion beam ( $E_{\text{mean}} \approx 370 \text{ MeV/u}$ ). Sum of all the positron emitter yields (solid line) and sum of the positron emitter yields excluding short-lived oxygen fragments (dashed line) are also reported. Convolution of the total positron emitter yield with Gaussian functions having FWHM 2, 4, and 8 mm are also presented in the figure to account for the finite resolution of the PET images. The background level is estimated to be about  $N_{\text{back}}/N(0) \approx 0.0018$  both for the  $^{12}\text{C}$  and  $^{11}\text{C}$  ion irradiation (horizontal dotted line in the figure). Calculations were performed with the Monte Carlo code SHIELD-HIT10 (Chapter 4).

Range verification accuracy of 1 mm is desirable in order to reduce the safety margins of the treatment planning (Pawelke *et al.*, 1996; Iseki *et al.*, 2004). Accuracies of less than 1 mm in the verification of the range can be reached provided that a sufficient number of registered photon coincidences are detected by the PET camera (Pawelke *et al.*, 1996). The minimum dose required for an

accuracy in the range verification of about 1 mm was estimated to be about 250 mGy in case of  $^{12}\text{C}$  ion carbon beam irradiation, 20 mGy for a primary beam of  $^{11}\text{C}$  particles and about 5 mGy for  $^{10}\text{C}$  ions, which corresponded to about 500 detected coincidences of a dual head positron camera made of position sensitive BGO crystals (Pawelke *et al.*, 1996). More recent studies from the Japanese group at NIRS showed that for an uncertainty of 0.3 mm in the range verification the peak dose required with  $^{10}\text{C}$  ion beams was found to be 96 mGyE (Iseki *et al.*, 2004). As compared to the conventional PET imaging where the reconstruction of complex activity maps are needed, for the range verification of the injected beam only the centroid of the activity peak at the end of the ion range is needed (Pawelke *et al.*, 1996). A PET camera should not only have a high resolution that would permit a better discrimination of the activity peak approximately located at the depth of the ion range on a high background activity, but also a high detection efficiency is desirable. In the case of the autoactivation method a high detection efficiency of the PET camera is crucial, this issue is relatively less important when the treatment is directly delivered by positron emitter beams and “normal” doses are administered. The prospective is again reversed if the radioactive beams are instead used as probing beams of low intensity, as mentioned above.

The main drawbacks in the use of radioactive beams are linked to the difficulties in achieving an intense enough production efficiency and beam purity. These topics will be addressed in the Chapter 3.

### 2.3 ALTERNATIVES TO PET IMAGING FOR TREATMENT DELIVERY VERIFICATION

During the irradiation with stable beams of light ions, beyond the relatively delayed emission of  $\beta^+$ -radiation from positron emitter fragments, *prompt* ( $t < 1$  ns) secondary radiation also exits the patient. This secondary radiation consists of both low mass charged particles ( $\alpha$  particles and, mainly, protons) and  $\gamma$ -rays. The main advantage resulting from the fast detection of the electromagnetic or charged particle radiation is in their potential for *real time* imaging. In principle, not only the detection of the possible misdelivery of the treatment can be performed, for example, after the irradiation of each slice of the tumor volume, but also the spatial information on the treatment delivery is not affected and corrupted by the biological washout.

Single prompt gamma rays are mainly the result of the nuclear de-excitation of the fragments generated during the primary ion beam slowing down path in the target (Testa *et al.*, 2010; Testa, 2011). The majority of gamma rays is emitted in-flight and therefore it conserves information about the location of the nuclear fragmentation reaction (Dauvergne *et al.*, 2009).

In a treatment verification performed via PET imaging, the emission of single prompt photons is one of the major sources of noise, which causes false coincidences to be detected. As consequence, the acquisition statistics is unavoidably reduced (up to 40%) and the exploitation of the PET signal during the beam extraction is prevented (Parodi *et al.*, 2005).

However, the single photon emission can be advantageously exploited for the verification of the range of the primary beam in the target if, for instance, collimated prompt gamma cameras or Compton cameras are used (Min *et al.*, 2006; Dauvergne *et al.*, 2009; Testa *et al.*, 2009). The profile of prompt gamma rays detected in orthogonal direction with respect to the beam path shows a peaked shape with a fall-off that can be correlated to the location of the Bragg Peak (Schardt *et al.*, 2010; Bom *et al.*, 2012). Gamma rays are emitted along almost the whole primary ion stopping path up to a few mm (2-3 mm) before the Bragg Peak. The shift is due to the fragment cross section threshold reached when the energy of the center of mass of the ion-target nucleus system becomes lower than the Coulomb barrier. Furthermore, the contribution from the  $\gamma$ -rays correlated with the ion track should be also distinguished from elastically or inelastically scattered neutrons or Compton scattered photons (Testa *et al.*, 2009). Experiments have also been performed to investigate the possible correlation of the neutron profile at 90° detection angle with the treatment delivery, but no evident correlation was found (Testa *et al.*, 2010). The correlation of the range of particles and the photon emission has been recently studied both for protons (Min *et al.*, 2006; Bom *et al.*, 2012) and carbon ion (Testa *et al.*, 2010) irradiations.

Testa and co-workers made use of a collimated gamma camera consisting of stacked thin detectors aligned to each collimator slit to provide a longitudinal snapshot of the photon emission profile. The information on the transverse position was instead obtained by the use of a position sensitive hodoscope (Testa, 2011). The hodoscope also gave information about the particle Time of Flight (TOF), so to also help discriminating the useful photon radiation from the background radiation (Dauvergne *et al.*, 2009). One of the main issues with this method is the rather poor counting statistics, particularly when physical collimating devices are in use. Experiments conducted at the facilities in GANIL (France) and GSI (Germany) on the irradiation of a PMMA and water block with 95 and 305 MeV/u carbon ion beams showed a net count rate along the ion beam path of  $1 \cdot 10^{-7}$  photons/(ion msr mm) with a background count rate of about  $1 \cdot 2 \cdot 10^{-7}$  photons/(ion msr mm). Expectations from Monte Carlo simulations of a 300 MeV/u carbon ion beam performed with GEANT4 (Agostinelli *et al.*, 2003; Allison *et al.*, 2006) reported that about 0.3 prompt photons per incident ion may be detected.

As an alternative to collimated cameras, Compton cameras have also been proposed (Roellinghoff *et al.*, 2011; Richard *et al.*, 2012) in order to increase the counting statistic by eliminating absorbing collimating devices. The Compton camera is an electronically collimate detection system, which generally consists of a stack of scattering detectors followed by an absorbing detector (Roellinghoff *et al.*, 2011). The trajectory of the emitted photon is reconstructed by the intersection of the cones containing the particle direction. The beam hodoscope can also be used in this case to tag the photons both in space and time. Monte Carlo simulations have recently been performed to support a future development of the camera (Roellinghoff *et al.*, 2011).

From the count rate point of view, the use of interaction vertex imaging techniques with charged particle is an advantage. The achievable statistics is 2-3

orders of magnitude higher with respect to the photon technique:  $6 \cdot 10^{-5}$  protons  $\text{ion}^{-1} \text{msr}^{-1}$  and  $5 \cdot 10^{-4}$  protons  $\text{ion}^{-1} \text{msr}^{-1}$  were detected at a 10 degree angle with respect to the primary beam direction for  $^{12}\text{C}$  ions at 95 MeV/u and 200 MeV/u, respectively, whereas about  $5 \cdot 10^{-7}$  prompt  $\gamma$ -rays  $\text{ion}^{-1} \text{msr}^{-1}$  were detected orthogonally to the beam direction (Testa, 2011). The shape of the charged particle detection profile is similar to the one mentioned in the gamma-ray case (i.e. a rather flat profile followed by a fall out in close proximity of the particle range). Both single-track vertexing (for a fragmentation multiplicity equal to 1) and multi-track vertexing (for a fragmentation multiplicity  $\geq 2$ ) are possible to reconstruct the fragmentation point coinciding with the point of emission of the charged particle. The vertex can be reconstructed by calculating the intersection of the primary beam direction, provided by a hodoscope, with one (single-track vertexing) or two or more (multi-track vertexing) fragment directions, provided by a position sensitive detectors located downstream (Henriquet *et al.*, 2012).

The spatial resolution of the method is, however, intrinsically limited by the multiple scattering of the particles. Larger counting rate is expected in the forward direction, which is also the direction most affected by geometrical uncertainties. However, at small angles with respect to the ion beam path the detection of the particle range become more difficult. Accuracies of the order of 1 mm are achievable (Dauvergne *et al.*, 2009). Feasibility studies and further research are ongoing in the framework of the ENVISION project (Henriquet *et al.*, 2012).

Finally, it is worth mentioning another nuclear imaging technique under development phase, which has the potential of achieving sub-millimeter spatial resolution, the so called  $\gamma$ -PET (Lang *et al.*, 2013). This technique combines a Compton camera with a PET. A 3-dimensional reconstruction of the activity is achievable due to the intersection of the Compton-cone surface with the Line of Response (LOR) extracted from PET acquisition (Lang *et al.*, 2013). The method could not only be applied to conventional nuclear imaging with the use of radioisotopes emitting both a positron and a gamma ray quasi-simultaneously (such as  $^{22}\text{Na}$ ,  $^{94}\text{Tc}$ ,  $^{89}\text{Zr}$ ,  $^{44}\text{Sc}$ ,  $^{68}\text{Ga}$ ,  $^{124}\text{I}$ ,  $^{152}\text{Tb}$ ,  $^{86}\text{Y}$ ,  $^{76}\text{Br}$ ,  $^{82}\text{Rb}$ ), but also to an irradiation with light ions to detect positron-gamma emitter fragments, such as  $^{10}\text{C}$ ,  $^{14}\text{O}$  particles.

## 2.4 BIOLOGICAL TREATMENT VERIFICATION AND OPTIMIZATION USING PET-CT DOSE RESPONSIVENESS IMAGING

The *in vivo* monitoring and quality control during ion beam therapy of malignant tumors has several advantages. On one hand, the actual irradiated volume could be determined and adaptive treatment approaches in subsequent treatment sessions based on PET-CT imaging could be applied (Brahme, 2003, 2009). The combination of PET with CT in the same imaging system allows for a better distinction between physiological uptake and pathological uptake, a shorter scan time due to the possibility of using the CT data for the attenuation correction, and improved lesion localization due to anatomical and functional co-registration. On the other hand, the information acquired by the imaging system could be placed

inside a much broader framework going far beyond the limits of the quality control and treatment replanning. In fact, the potentially available information on the dose delivery distribution could be combined with the information on the tumor responsiveness to the treatment so as to create a fully optimized and individualized radiation treatment method, according to the BIOART (Biologically Optimized in vivo predictive Assay based Radiation Therapy) approach as shown in Figure 3 (Brahme, 2003).

The central goal in radiation therapy is to determine the dose delivery distribution that maximizes the complication free tumor control probability and minimize the normal tissue morbidity.

The expected probability for tumor eradication may be expressed as shown by (Brahme, 2003):

$$P_B = \exp(-\bar{N}) = \exp\left(-\iiint_V n(r) d^3 r\right) = \exp\left(-\iiint_V n_0(r) e^{-D(r)/D_e(r)} d^3 r\right), \quad (1)$$

where  $\bar{N}$  is the mean number of surviving clonogens in the total volume  $V$ ;  $n_0(r)$  and  $n(r)$  are, respectively, the initial density of clonogens per unit volume, and the corresponding surviving number of clonogens at the spatial coordinate  $r$ .  $D(r)$  and  $D_e(r)$  are, respectively, the delivered dose and the effective radiation resistance at the point  $r$ . The effective radiation resistance is defined as the dose that causes a decrease in the cell survival of  $1/e$  ( $\approx 37\%$ ).

One of the central statements of the BIOART theory is that the tumor eradication probability shown in equation (1) can be calculated based on the information retrieved by PET images acquired with radiopharmaceuticals able to detect the spatial distribution of clonogenic cells, for example, fluorodeoxyglucose (FDG).

A necessary condition for the applicability of the algorithm is that two PET images are acquired: one before the start of the treatment and the other one after a few fractions of radiation dose (such as after the first week of therapy). The time lapse between the first and second image should be so that the fraction of clonogenic cells is still detectable and that inflammatory reactions, typically arising after the early treatments, are not affecting to a large extent the activity signal detected by the PET camera.

The latter issue could, to some extent, be solved if radiopharmaceuticals more specialized for detecting tumor cells are used. In fact, the accuracy in the determination of the clonogens density is linked to the property of the radiopharmaceutical under usage. Despite FDG is by far the most commonly used PET tracer, which exploits the increased glucose uptake and metabolism in malignant cells, it might not be the optimal tracer in this sense.

The BIOART algorithm lays his foundation on the following approximate relation of proportionality

$$PET_n(r) \propto \rho(r) \cdot f_n(t, D, r), \quad (2)$$

which is valid provided the vasculature is normal in all tissues and the tracer reaches the tumor cells.  $PET_n(r)$  is the PET activity signal registered after the  $n^{\text{th}}$  fraction and  $\rho(r)$  is the density of the imaging substance, which is assumed to be known.  $\rho(r)$  could be approximated by the convolution of the vascular fluence

density and a diffusion kernel (Brahme, 2003). For instance, the vasculature density could be imaged by using ammonia ( $^{11}\text{CH}_3$ ) or water ( $\text{H}_2^{15}\text{O}$ ).  $f_n(t, D, r)$  is the number of functional clonogenic cells<sup>9</sup>.

Thus the role of the PET imaging is dual. On one hand, it can, in principle, be used to calculate the mean dose distribution during the first n treatment fractions and, on the other hand, it can be used to extract information about the effective radiation resistance of the tumor and the number of functional clonogens.

Taken together, the BIOART approach not only provide the theoretical framework for the exploitation of a physically optimized treatment plan, where one could assess the level of tumor eradication probability based on the dose delivery distribution, but also, and more importantly, could be applicable to optimize the treatment in terms of radiobiological responses. This can be achieved by combining the calculation of the tumor eradication probability to the normal tissue complication probability, so as to finally maximize the complication-free cure (P+) or the probability to minimize the injury at nearly maximum complication free cure (P++) (Brahme, 2003).

The BIOART principle is very general and *a priori* valid for any radiation type. So far, its proof-of-principle principle has been given for radiation therapy of lung tumors with photons (Brahme, 2009, 2010). Generally, the application of the BIOART approach to light ion therapy might be more difficult if extreme hypofractionation regimes are performed, since at least two treatment fractions about a week apart are required. It is therefore not useful for single fraction of light ion therapy of lung tumors (cf. (Tsujii *et al.*, 2008)). Further clinical research on this topic is required. More insights might be given in the framework of the European ARTFORCE<sup>10</sup> (Adaptive and innovative Radiation Treatment FOR improving Cancer patients' treatment outcome) collaboration, which involves several major institutes in Europe. The Karolinska Institutet and the RaySearch Laboratories (Sweden) are currently investigating on the biological adaptive treatment planning possibility for photon IMRT.

---

<sup>9</sup> Brahme introduces a distinction between *temporarily functional* and *finally surviving* tumor cells. The temporarily functional tumor cells are defined as the cells that are imaged by PET, even though they might be lethally damaged and disappear within a certain time period.

<sup>10</sup> <http://www.cancerartforce.eu/>

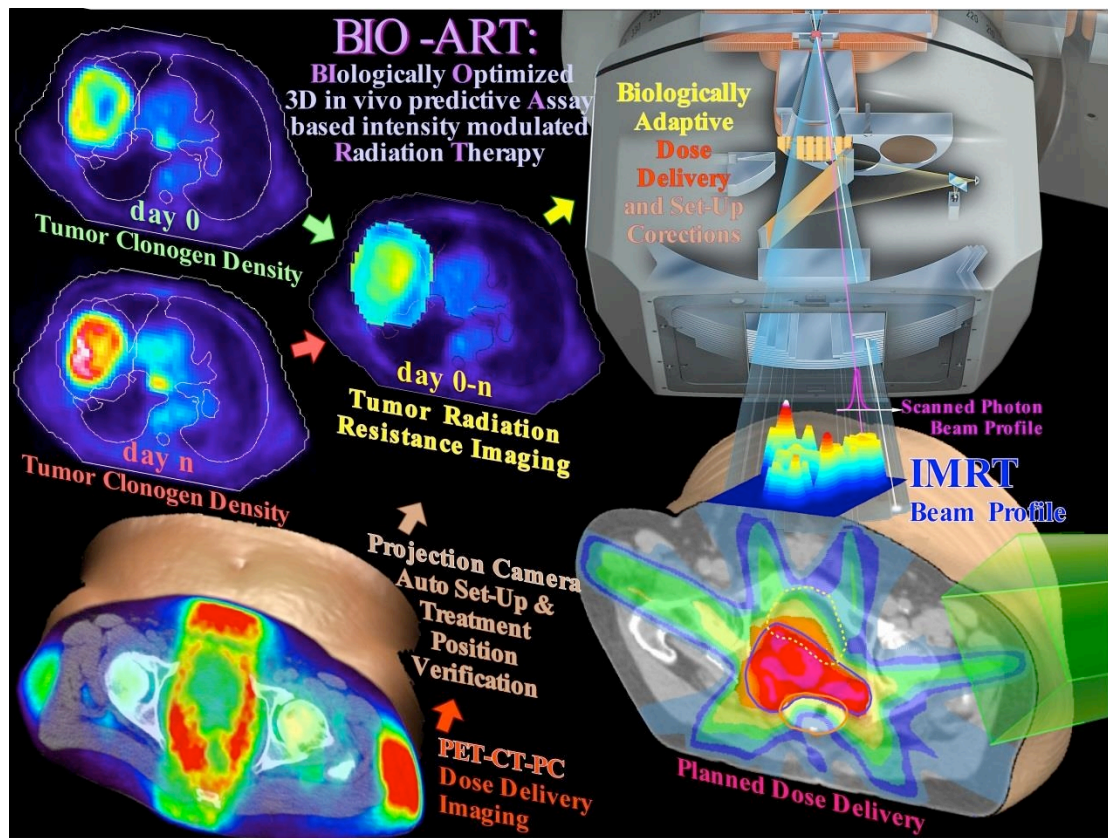


Figure 3 Illustration of the BIOART approach applied to IMRT showing how dose responsiveness imaging may be combined with dose delivery imaging to achieve a biologically optimized adaptive radiation therapy. PET technology may, in principle, be used both for monitoring the dose delivered with external beams (lower left panel) and for assessing the tissue responsiveness to radiation therapy (upper left panels) with the final aim of achieving an adaptive radiation treatment according to the actual absorbed dose delivered and the individual response of each patient (right half of figure) (Brahme, 2009).

### **3 PRODUCTION OF CLINICALLY USEFUL POSITRON EMITTER BEAMS**

#### **3.1 HIGH QUALITY $^{11}\text{C}$ POSITRON EMITTER BEAMS**

The aim of the thesis is to maximize the production yield of high quality $^{11}\text{C}$  positron emitter beams through the in-flight fragmentation method by analyzing all the main steps from the production of the beam and the transport in the beam optical system to the purification of the beam from other potentially contaminating fragments.

The solution proposed in this work could, in principle, be applied both to synchrotron, high intensity linac and cyclotron based facilities. However, it naturally stems from a cyclotron based facility, such as that planned for the Karolinska Hospital (Brahme, 2010) equipped with an excentric gantry (Figure 4). The general aim of project arises as the summa of specific sub-aims, which coincide with the steps of the progress time line of the project itself:

- The selection of the optimal material to increase the yield of  $^{11}\text{C}$  projectile-like fragments, minimize the  $^{11}\text{C}$  ion beam emittance (i.e. angular and radial spread), and thus maximize the brilliance (proportional to the ratio of the beam intensity and beam emittance);
- The reduction and almost elimination of the energy spread of the secondary  $^{11}\text{C}$  ion beam by the use of a variable wedge-shaped degrader;
- The purification of the  $^{11}\text{C}$  ion beam from other contaminating fragments through magnetic rigidity, energy loss and TOF-velocity filtering.

This project also aimed to contribute to the testing of the Monte Carlo code SHIELD-HIT nuclear models through the comparison of total inelastic, total and partial charge changing cross sections, and fragment yields with experimental data for carbon ion beams (Chapter 4).

The analysis of the produced secondary  $^{11}\text{C}$  ion beam requires taking into account several steps, which are addressed in the following sections. A short discussion on the methods used to produce radioactive beams and on the current facilities, with particular attention to the medical field, is given in Section 3.2. The selection of the production target from the maximization of the particle yield point of view is described in section 3.3, the characterization of the beam from an angular and radial spread point of view is disclosed in section 3.4, the reduction of the energy spread of the beam is the subject of section 3.5, and finally the main

---

<sup>11</sup> In this work, with “High quality” it is intended to indicate beams having energy, angular and radial spread suitable for accurate radiation treatment.

characteristics of the proposed beam line design and the purification of the beam from contaminating fragments are given in section 3.6.

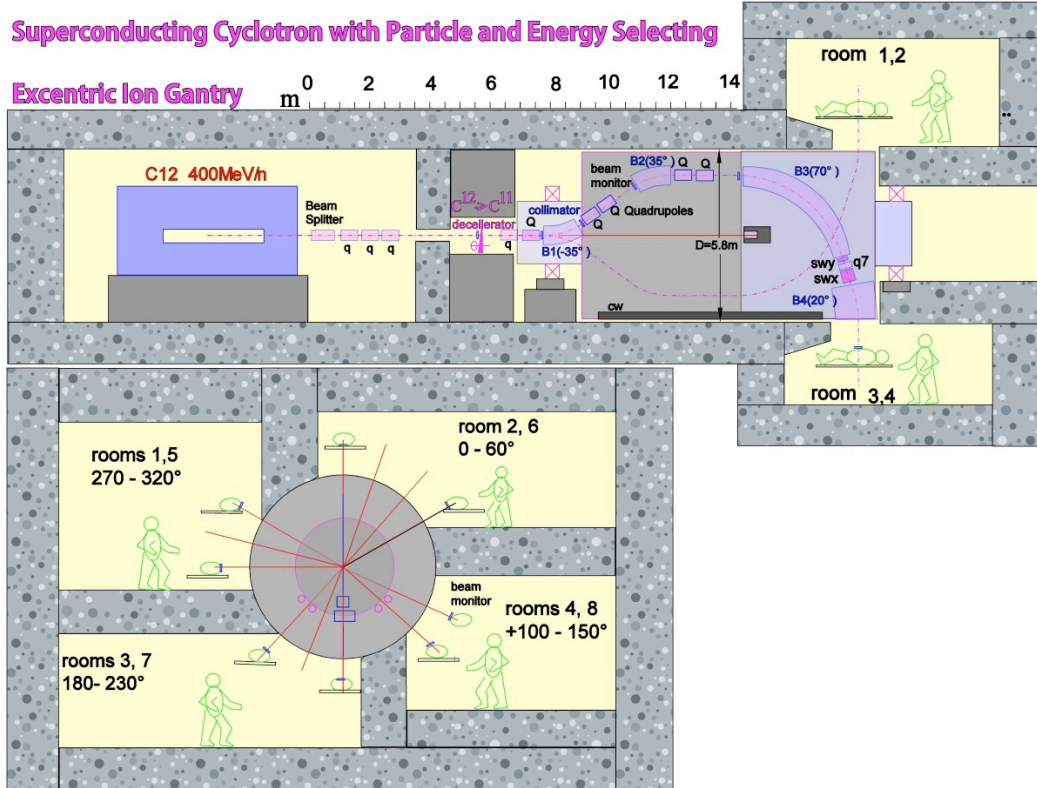


Figure 4 Cross section through the superconducting cyclotron with the light ion excentric gantry capable of treating patients in 4 surrounding rooms as shown in the lower left panel (Brahme, 2010). The beam line shown in the figure presents an early study of the design given by (Brahme, 2010), which is planned to be update with the new design resulting from the findings of this project (cf. Figure 12). The  $^{11}\text{C}$  ion beam is intended to be produced in the decelerator located upstream in the beam line. The use of a positron emitter beam for treatment allows more accurate *in vivo* Bragg peak imaging and it is intended to be used both for treatment delivery verification prior treatment and for treating tumors located in proximity of organs at risk.

### 3.2 RADIOACTIVE ION BEAM PRODUCTION METHODS

Several methods can be envisaged in order to produce radioactive beams. They can be classified in two main categories, even though this distinction is becoming less and less sharp for recent facility designs: the in-flight fragmentation method and the so called Isotope Separation On Line (ISOL) method (Blumenfeld *et al.*, 2013).

In the in-flight fragmentation method, the radioactive ions of interest are selected among the various reaction products following the interaction of a primary beam with a target, usually a thin<sup>12</sup> target. The separation stage is generally based on the

<sup>12</sup> The definition of thin/thick target is not free from ambiguities. However, in this context, it might be useful to consider as thin a target where the generated projectile-like fragments leave the target

use of several dipole magnets possibly complemented by a degrader stage to achieve a final mass  $A$  and charge  $Z$  selection through an  $A/Z$ -selection performed by the dipoles followed by a  $Z$ -selection performed with the degrader stage. Some of the in-flight fragmentation facilities make use of storage rings (e.g. the ESR storage ring at GSI, the Test Storage Ring at MPI in Heidelberg etc.), where the beam is injected and decelerated via stochastic or electron cooling techniques (Blumenfeld *et al.*, 2013).

Classically, the ISOL method is based on the injection of an intense primary beam into a target. The reaction products are then thermalized and stopped into a catcher, which, in case of a thin target experiment is an additional gas or solid element, whereas, for thick target experiments, it coincides with the target itself. Then through diffusion and effusion processes the fragments of interest are transferred to an ion source. After mass selection in an isobar separator, the radioactive isotopes are finally post-accelerated (Lindroos, 2004; Blumenfeld, 2008; Blumenfeld *et al.*, 2013). The production of radioactive nuclei at rest and their re-acceleration is usually chosen for producing low-energy radioactive beams (Bimbot, 1995).

The main focus of the majority of the current radioactive beam facilities worldwide is on fundamental interaction experiments to produce rare isotope beams and condensed matter atomic physics with final ion acceleration energies not suitable for treatment. However, the increasing interest in the radiation therapy with radioactive ion beams is promoting the production of radioisotopes intended for medical applications (Blumenfeld *et al.*, 2013).

Four main fragmentation facilities make use of the in-flight fragmentation method: GANIL (France), GSI (Germany), NSCL/MSU (USA) and RIKEN (Japan). Among them, only the SchwerIonenSynchrotron (SIS) at GSI is able to accelerate ion up to energies of 2 GeV/u, while the other facilities have lower acceleration energies. The main facilities which make use of the ISOL method are instead: CERN-ISOLDE (Switzerland), GANIL-SPIRAL (France), Oak Ridge-HRIBF and TRIUMF (North America). More details and a review of past and new planned facilities is given by (Blumenfeld *et al.*, 2013).

As mentioned in Chapter 2, the first investigations on the use of radioactive beams for radiation therapy started in the late 70's at the LBL (USA), where the world's first relativistic heavy ion accelerator, the Bevelac, was located (Alonso and Castro, 2002). The radioactive beam research at Berkeley was mainly focused on  $^{19}\text{Ne}$  and  $^{11}\text{C}$  ion beams produced by the in-flight fragmentation of the stable isotopes on a beryllium target (Alonso *et al.*, 1979; Llacer *et al.*, 1979; Chatterjee *et al.*, 1981; Chatterjee *et al.*, 1982; Llacer *et al.*, 1984b; Tobias, 1985).

Years later, two main European facilities followed the footsteps of the LBL research with radioactive beams. At GSI (Germany) the investigations concerned  $^{15}\text{O}$ ,  $^{17}\text{F}$  and  $^{19}\text{Ne}$  ions in the energy range produced by projectile fragmentation in a beryllium target (about 4 gcm $^{-2}$ ) (Enghardt *et al.*, 1991)) from 300 to 500 MeV/u (Pawelke *et al.*, 1996). The intensity of the radioactive neon ions given in the GSI-report (year 1991) was about  $10^5$  particles/spill for a primary ion  $^{20}\text{Ne}$  beam of  $10^8\text{-}10^9$  particles/spill (Enghardt *et al.*, 1991). However, the GSI research

---

with approximately the same velocity as at the moment of production. Thus, the electronic energy losses in the target due to the slowing down process should be negligible.

continued with the autoactivation method, rather than the exploitation of the radioactive beams for treatment.

The production of radioactive ion beams from the fragmentation of 400 MeV/u ions ranging from  $^{12}\text{C}$  to  $^{20}\text{Ne}$  was one of the main focuses of the extensive analysis and review conducted during the European Light Ion Medical Accelerator (EULIMA) collaboration (Bimbot, 1988; EULIMA, 1988). The general aim of the EULIMA collaboration was to investigate the potential benefits of the use of light ions for cancer treatment and describe the requirements for a future clinical installation of an ion therapy dedicated accelerator. However, the project never saw a practical continuation.

Other investigations on radioactive ion beams produced by in-flight fragmentation of 44 MeV/u  $^{40}\text{Ar}$  and 65 MeV/u  $^{16}\text{O}$  in a beryllium target were performed at GANIL (France) during the 80's (Bimbot *et al.*, 1985; Bimbot *et al.*, 1986).

Beyond the experience coming from the above mentioned European facilities, the institute where most part of the radioactive ion beam investigation has been conducted in recent years is the National Institute of Radiological Science (NIRS), in Chiba (Japan). The Japanese facility adopted in the course of the years two different modalities in order to produce the radioactive beams. Initially the in-flight projectile fragmentation method was preferred and a secondary beam course dedicated to the production of positron emitter carbon ions was built in 1997 (Iseki *et al.*, 2004). Radioactive beams of carbon isotopes were originally produced through the projectile fragmentation method with a carbon ion beam impinging on a beryllium target ( $^7\text{Be}$ ). Kanazawa and co-workers report the achieved outcome intensity of the  $^{11}\text{C}$  ion beam as a function of the target thickness, the achromatic aluminium degrader thickness and the momentum acceptance of the beam line (Kanazawa *et al.*, 2002; Kanazawa *et al.*, 2004a; Kanazawa *et al.*, 2004b). With an incoming beam of carbon ions having an energy equal to 430 MeV/u (which is the maximum energy allowed by the Heavy Ion Medical Accelerator in Chiba (HIMAC)), a maximum production rate of about 0.97% of the incoming primary beam intensity is achieved, with a purity of about 93%, in absence of the aluminium degrader and with a beryllium target 51 mm long. The mean energy of the secondary  $^{11}\text{C}$  ion beam was about 355 MeV/u. If a 10.6 mm of degrader thickness is used, the purity of the beam is increased to the 99% and the intensity of the  $^{11}\text{C}$  ion beam consequently decreased to 0.76%. The mean energy of the secondary  $^{11}\text{C}$  ion beam is in this case about 330 MeV/u. The main impurities were due to the primary  $^{12}\text{C}$  ions and  $^7\text{Be}$  fragments (Kanazawa *et al.*, 2002). The momentum acceptance was about  $\pm 2.5\%$  and the angular acceptance 13 mrad (Suda *et al.*, 2000; Kanazawa *et al.*, 2002).

With the intensity achieved through the projectile fragmentation method at NIRS, approximately 3-4 minutes of irradiation were required in order to deliver the physical dose of 1 Gy in a target volume of  $3.5 \times 3.5 \times 5 \text{ cm}^3$  (Kitagawa *et al.*, 2001).

At NIRS, an alternative technique was recently preferred to the projectile fragmentation method. The technique is based on the method commonly used to produce radiopharmaceuticals for PET (Shirai *et al.*, 2009). The  $^{11}\text{C}$  ions are generated through the nuclear reaction  $^{14}\text{N}(\text{p},\alpha)^{11}\text{C}$  in a target chamber filled with  $\text{N}_2$  gas and 5% of  $\text{H}_2$  to produce  $^{11}\text{CH}_4$  molecules (Donets *et al.*, 2010). The

proton beam ( $E_p \approx 18$  MeV) is produced in a separated cyclotron before being injected in the target. After separation from the  $N_2$  gas using a cryogenic system, the methane is then loaded into an ion source. About  $4 \cdot 10^{12}$  methane molecules can be produced each 20 minutes. To improve the efficiency of the ion source an electron string ion source is under development phase in collaboration with the Joint Institute for Nuclear Research (JINR), Russia (Hojo *et al.*, 2008; Noda *et al.*, 2011; Kitagawa *et al.*, 2012). The proton irradiation generates a sufficient number of particles, however, the number of  $^{11}C$  ions which are eventually injected into the HIMAC synchrotron is limited by the rather low efficiency of the compression/ionization process (Shirai *et al.*, 2009),  $10^7$ - $10^8$  particles per injection versus the  $10^{10}$  usually necessary for treatment (Shirai *et al.*, 2009). Therefore, a cooling-stacking technique (Tanabe *et al.*, 1991) has been proposed at HIMAC to intensify the  $^{11}C$  ion beam to  $10^9$  particles per injection (Shirai *et al.*, 2009). In fact, at HIMAC two identical synchrotrons are available, the lower one can serve as a storage ring and electron cooler where multiturn-injected beams can be stacked (Noda *et al.*, 2000). In the heavy vacuum storage ring, the ion beam interacts with an electron beam and it adjusts to the velocity of the electrons (Müzenberg, 1992; Geissel *et al.*, 2002), so that the momentum spread can be reduced to values as low as  $10^{-6}$  FWHM (Müzenberg, 1992; Geissel *et al.*, 2002). However, issues related to the reduction of the cooling time and coherent beam instability have been recently reported (Shirai *et al.*, 2009). The solution adopted at the Japanese facility might also be extended to the production of other short-lived positron emitter beams, such as  $^{15}O$  and  $^{10}C$  ions (Hojo *et al.*, 2008). Nevertheless, this technique is certainly more costly, not least for the required presence of an additional cyclotron and an electron cooler storage ring. Thus, the different techniques for the production of radioactive beams can be classified on a time scale base, as shown in Table 2.

	Ultra-fast	Medium	Slow
Time scale	ns	ms	min-hr
Method	In-flight	Re-acceleration Storage ring Electron cooling	Cyclotron production Separation at the ion source
Ion separation	Magnetic rigidity TOF Velocity filtering	Not needed	Not needed
Properties	Possibility of producing short-lived ions (e.g. $^{9}C$ , $^{8}B$ , $^{14}O$ )	Possibility of producing short-lived ions (e.g. $^{9}C$ , $^{8}B$ , $^{14}O$ )	Mainly ions with longer half-life

Table 2 Classification of the different techniques for production of radioactive beams depending on their time scale.

### 3.3 THE SELECTION OF THE TARGET MATERIAL FROM THE PRODUCTION EFFICIENCY POINT OF VIEW

The maximization of the yield of the  $^{11}\text{C}$  fragments produced during the slowing down of a primary  $^{12}\text{C}$  ion beam is the first step in the selection of the optimal target material.

In general, the intensity of the secondary beams depends on the choice of the target material, its thickness and the specific properties of the production reaction (Alonso *et al.*, 1979). Specifically, projectile-like fragments are of interest in our case, since the secondary  $^{11}\text{C}$  ion beam should have the highest possible energy at the exit of the target and as well as the lowest possible emittance.  $^{11}\text{C}$  target-like fragments have to be discarded, since they have very low velocity and they are isotropically emitted (Greiner *et al.*, 1975; Morrissey, 1989). As an example, in Figure 5, the fluence differential in energy of the  $^{11}\text{C}$  fragments for a 400 MeV/u  $^{12}\text{C}$  ion primary beam is shown for liquid hydrogen and graphite at depths corresponding to a mean energy of the  $^{11}\text{C}$  ion beam of about 200 MeV/u. A clear separation in the fragment energy is seen in the figure, which is likely to coincide with the projectile-like and target-like regions.

By selecting the material of the production target, the yield of the projectile-like  $^{11}\text{C}$  ion beam can be substantially increased. Experiments conducted at LBL (USA) indicated that materials having low atomic number ( $Z$ ) are preferred as nuclear production target, since the fragment production is higher, the primary beams are attenuated more rapidly (as a function of the depth in units of  $\text{g}/\text{cm}^2$ ) and there is less multiple scattering (Alonso *et al.*, 1979).

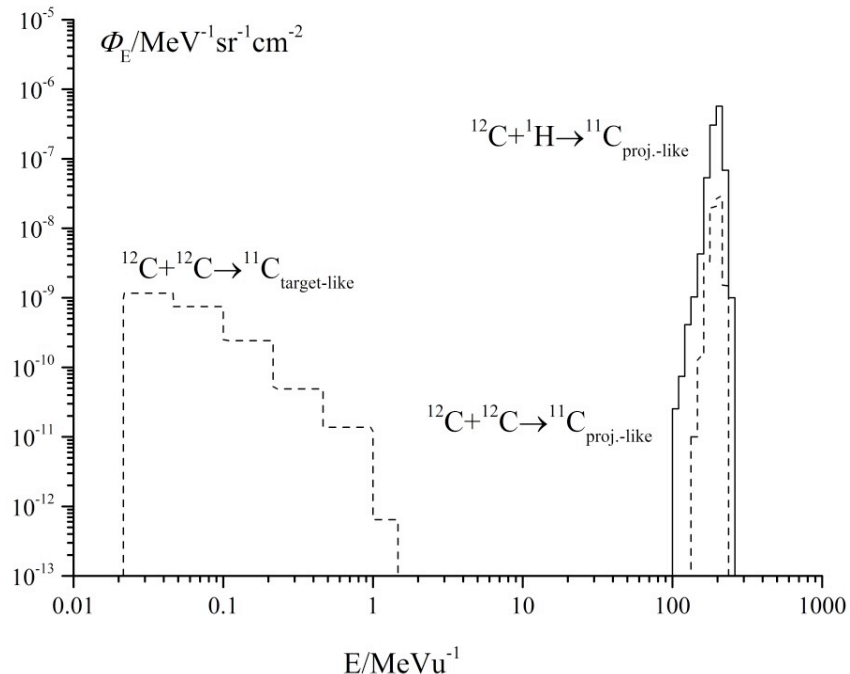


Figure 5 Fluence differential in energy of the  $^{11}\text{C}$  fragments on 400 MeV/u  $^{12}\text{C}$  ion beams for a liquid hydrogen (solid lines) and a graphite target (dashed lines) at a depth approximately corresponding to 200 MeV/u of  $^{11}\text{C}$  mean energy in both targets. A net distinction in the fragment energy region is seen, which is likely to coincide with the projectile- and target-like fragment regions.

In Figure 6(a), the attenuation of the primary  $^{12}\text{C}$  ion beam with initial energy 400 MeV/u is shown as a function of the depth (in units of g/cm<sup>2</sup>) for some of the target materials studied in paper I.

The attenuation of the primary beam is described by  $\Phi_p(z) = \Phi_p(0)\exp(-\mu_p z)$ . The mass absorption coefficient, in the first approximation of energy independence in the high energy region (Kempe and Brahme, 2010a), may be written as:

$$\mu_p/\rho = n\sigma_{r,0} = N_A/A_T \sigma_{r,0} \cong N_A/A_T \cdot \pi R_0^2 (A_T^{1/3} + A_p^{1/3} - b)^2, \quad (3)$$

where  $R_0$  is the nuclear radius proportionality constant,  $A_T$  and  $A_p$  are respectively the molar mass of the target and projectile.  $\sigma_{r,0}$  is the total energy-independent reaction cross section (equation 3, paper I). For energies higher than 110 MeV/u, the reaction cross section can be considered as energy independent and mainly related to the geometric characteristic of the projectile and target (Sihver *et al.*, 1993; Sihver and Mancusi, 2009).  $b$  is the mean overlap parameter between the projectile and the target, which is meant to represent the partial transparency of the nuclear surfaces (equations (3-5) in paper I, (Goldhaber and Heckman, 1978; Sihver *et al.*, 1993; Sihver *et al.*, 2008)). The parameter  $b$  may be expressed as a second order polynomial in  $A_T^{1/3}$  and  $A_p^{1/3}$ , as given in equations (4) and (5) of paper I. If the primary ion is fixed, as in our specific case of  $^{12}\text{C}$  incident beams, the dependency of the mass attenuation coefficient with the molar mass of the material  $A_T$  composing the target roughly varies as  $A_T^{-1/3}$ , indicating that the lighter the target the more the beam is attenuated due to nuclear reactions with the atoms of the medium (cf. Figure 6(a)). Figure 6(b) shows the variation of the primary  $^{12}\text{C}$  ion fluence as a function of its mean energy in different targets.

Results of the fragmentation of a primary  $^{12}\text{C}$  ion beam presented in Figures 3(a) and 3(b) of paper I (cf. also Figure 7 of this report) have shown that the highest production yield of  $^{11}\text{C}$  fragments is achieved for a pure liquid hydrogen target. As compared to beryllium or carbon, which are the most commonly used in-flight fragmentation target materials (Geissel *et al.*, 1989; Kanazawa *et al.*, 2002), the production yield maximum is almost doubled and reaches about 8% of the primary beam intensity, when the whole energy and angular spectra of the particles are considered.

The relative yield of a certain fragment type,  $i$ , is governed by the partial reaction cross sections resulting in the production of the fragments,  $\sigma_i$ , the number of atoms in the considered target thickness ( $nz$ ), as well as on the attenuation of the incoming primaries and the corresponding fragments in thick targets (equation (4)). Clearly, the fragment production yield is higher for thicker targets. However, at the same time the beam emittance becomes larger, as further described in Section 3.4.

In first approximation, the fluence of the fragment of type  $i$ ,  $\Phi_i(z)$  can be expressed as  $\Phi_i(z) \approx \Phi_p(0)z\sigma_i n$ , where  $\Phi_p(z)$  is the primary particle fluence after the target thickness  $z$ . For example, despite the lower cross section for production of projectile-like  $^{11}\text{C}$  fragments in liquid hydrogen with respect to graphite in a  $^{12}\text{C}$  primary ion beam ( $\sigma_{^{12}\text{C}+^{1}\text{H} \rightarrow ^{11}\text{C}}/\sigma_{^{12}\text{C}+^{12}\text{C} \rightarrow ^{11}\text{C}} \cong 1/2$ , cf. paper I, figures 1 and 2), a thicker target is required for the same energy loss (due to the lower linear

stopping power). Therefore,  $\Phi_{^{12}\text{C}+^1\text{H} \rightarrow ^{11}\text{C}} / \Phi_{^{12}\text{C}+^{12}\text{C} \rightarrow ^{11}\text{C}} \approx n_{^1\text{H}} \sigma_{^{11}\text{C}} l_{\Delta E, ^1\text{H}} / n_{^{12}\text{C}} \sigma_{^{11}\text{C}} l_{\Delta E, ^{12}\text{C}} \gg 1$ , where  $n$  is the number of atoms per unit volume ( $n = N_A \rho / A_T$ ) and  $l$  is the length of the target corresponding to a fixed energy loss  $\overline{\Delta E}$ .

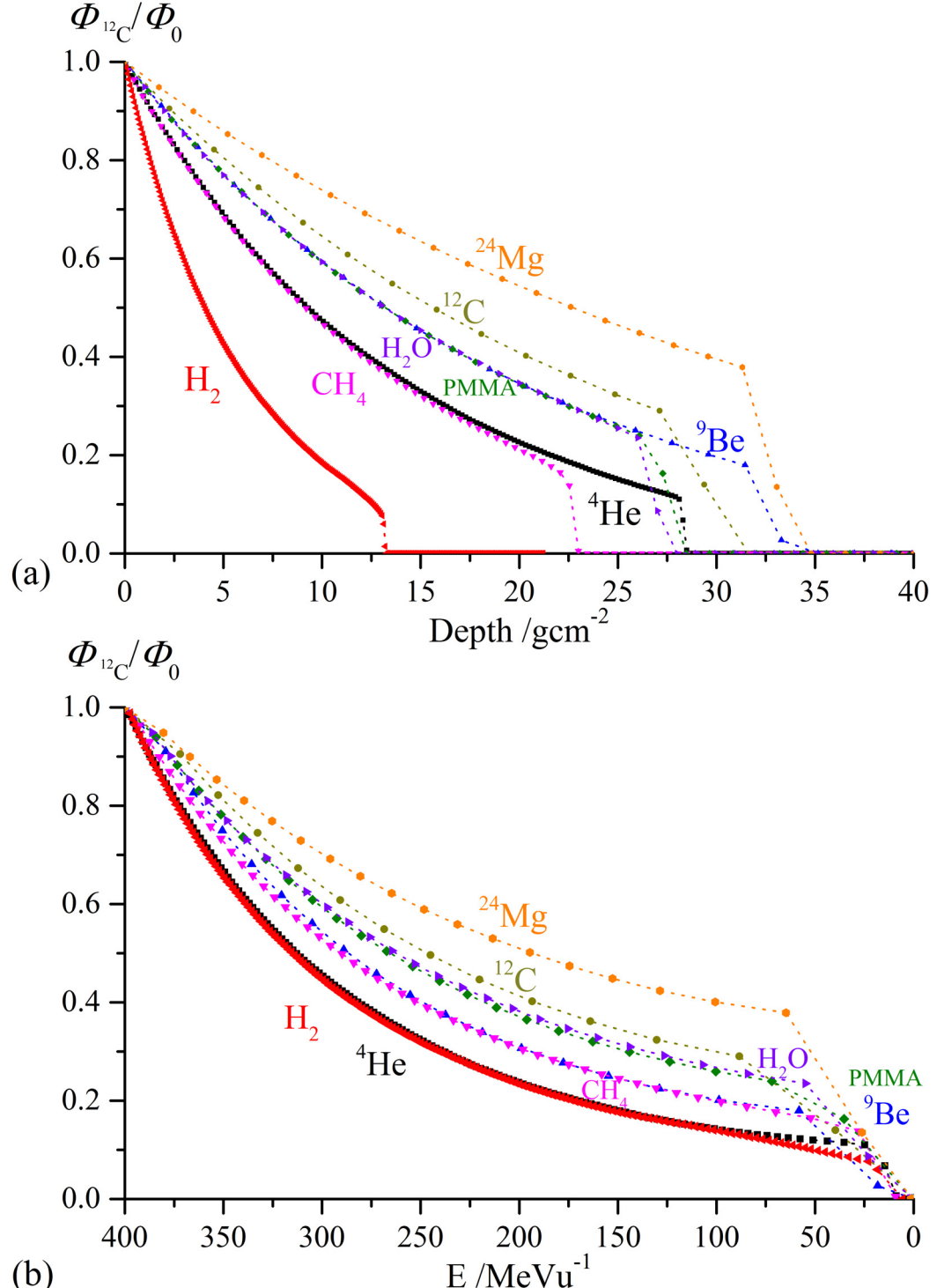


Figure 6 Attenuation of  $^{12}\text{C}$  primary particle fluence (normalized to the initial fluence) as a function of the depth (a) and variation of the  $^{12}\text{C}$  ion beam fluence as a function of its mean energy (b) in several target materials.

More accurately, the fluence build-up of secondary fragments may be written as:

$$\frac{\Phi_i(z)}{\Phi_{p,0}} = \int_0^z \sigma_i \cdot n \cdot e^{-\mu_p s} e^{-\mu_i(z-s)} ds \approx \frac{r_{i,T} N_A}{A_T} \rho_T \sigma_{r,0} \left( \frac{e^{-\mu_i z} - e^{-\mu_p z}}{\mu_p - \mu_i} \right) \quad z \leq R_p, \quad (4)$$

where  $r_{i,T}$  is the ratio between the cross section of production of the specific fragment  $i$ ,  $\sigma_i$ , and the total reaction cross section  $\sigma_{r,0}$ ,  $N_A$  is the Avogadro's number and  $A_T$  is the molar mass of the material (cf. paper I and (Kempe and Brahme, 2010a)).  $\mu_p$  and  $\mu_i$  are the attenuation coefficients of the primary and fragments, respectively. The  $^{11}\text{C}$  fragments are generated up to a depth which roughly corresponds to the primary particle practical range  $R_p$  (Kempe and Brahme, 2010a) provided that their energy is above the reaction energy threshold for the considered material.

The  $^{11}\text{C}$  fluence build-up maxima derived from Monte Carlo simulations have shown an exponential decrease as a function of the molar mass of the material in case of elemental targets (Figure 2, paper I). For compounds, a relationship was found between the fraction by weight of hydrogen atoms and the fluence build-up maximum of  $^{11}\text{C}$  ions, as seen in Table 3 and Figures 2 and 3 in paper I. In this respect, a new definition of the effective molar mass ( $A_{\text{eff}}$ ) was introduced, which takes into account the differences in  $^{11}\text{C}$  production according to the hydrogen content of the material. For elements, the effective molar mass coincides with the molar mass.

$$A_{\text{eff}} = \frac{\sum_i A_i N_i (\Phi_{f,\max}(A_i)/\Phi_{p,0}(A_i)) / (\Phi_{f,\max}(H)/\Phi_{p,0}(H))}{\sum_i N_i}, \quad (5)$$

where  $N_i$  is the number of atoms of a given element  $i$  in the compounds,  $A_i$  is the molar mass of each element  $i$ ,  $\Phi_{f,\max}(A_i)/\Phi_{p,0}(A_i)$  is the normalized value of the fluence build-up maximum evaluated for a target corresponding to the element  $i$ , and  $\Phi_{f,\max}(H)/\Phi_{p,0}(H)$  is the value of the normalized fluence build-up maximum evaluated for an hydrogen target.

The expression of the fluence build-up maximum of projectile-like fragments can also be analytically derived from equation (4) (Kempe and Brahme, 2010b).

The fluence build-up maximum is given by:

$$\Phi_{f,\max}/\Phi_{p,0} = r_{i,T} (\mu_p/\mu_f)^{1/(1-\mu_p/\mu_f)} = r_{i,T} (\sigma_p/\sigma_f)^{1/(1-\sigma_p/\sigma_f)}, \quad (6)$$

where  $\sigma_p$  and  $\sigma_f$  are the total reaction cross sections for the primary particles and fragments, respectively. In agreement with (Alonso and Krebs, 1984), the peak production yield is expected to be related to the ratio of the cross section for the desired ion to the total reaction cross section. In paper I, the factor  $(\sigma_p/\sigma_f)^{1/(1-\sigma_p/\sigma_f)}$  is calculated by the use of the semi-empirical cross section parameterization by (Sihver *et al.*, 1993; Sihver *et al.*, 2008) and, in case of  $^{12}\text{C}$  and  $^{11}\text{C}$  ions, its value, in the high energy approximation, is almost constant for the materials analysed in this study.  $r_{i,T}$  for projectile-like fragments shows an

exponential decrease as a function of the effective molar mass (Figure 2, paper I), being the highest in case of a liquid hydrogen target. The values of  $\tau_{\text{LT}}$  for projectile-like fragments were calculated with the Multi Stage Dynamical Model (MSDM) generator included in the Monte Carlo code SHIELD-HIT (Botvina *et al.*, 1990; Botvina *et al.*, 1997) (Chapter 4).

In Figure 7, the fluence build-up of positron emitter beams of interest,  $^{14,15}\text{O}$ ,  $^{9,10,11}\text{C}$ ,  $^8\text{B}$  ions, from stable  $^{16}\text{O}$  ( $\bar{E}=430$  MeV/u),  $^{12}\text{C}$  ( $\bar{E}=400$  MeV/u) and  $^{10}\text{B}$  ( $\bar{E}=325$  MeV/u) primary beams, respectively, is shown as a function of the depth for different target materials (water, beryllium, liquid deuterium and liquid hydrogen). The advantage of using the liquid hydrogen target is clearly seen. The liquid hydrogen target might be also used for the production of other  $\beta^+$ -emitter beams. However, for positron emitter ions which require the removal of more than one neutron from the incident primary beam, the production cross sections are considerably lower and the generated yield maxima are notably decreased. As a rule of thumb, the production cross sections decrease with one order of magnitude for each neutron removal. Nevertheless, for the short-lived  $^{10}\text{C}$  and  $^{14}\text{O}$  fragments the production yield might be still sufficient for range verification of the treatment with low intensity probing beams prior treatment with the stable isotopes (Section 2.2.2), even though larger energy distribution of these secondary beams has also to be accounted for and unavoidably reduces the outcoming useful yield.

Material	Density [g/cm <sup>3</sup> ]	$z_{\text{max}}$ [g/cm <sup>2</sup> ]	$\Phi_{^{11}\text{C}}(z_{\text{max}}) / \Phi_{^{12}\text{C}}(0)$ [%]	$f_{\text{H}}$	$A_{\text{eff}}$ [u]
$\text{H}_2^{**}$	0.071*	6.3	7.7	1	1
Methane ( $\text{CH}_4$ ) <sup>**</sup>	0.42*	14.3	6.1	0.251	2.13
Ammonia ( $\text{NH}_3$ ) <sup>**</sup>	0.68*	16.4	5.7	0.180	2.36
Polyethylene ( $\text{C}_2\text{H}_4$ )	0.94	16.5	5.6	0.140	2.88
Water ( $\text{H}_2\text{O}$ )	1	20.0	5.4	0.112	3.05
PMMA ( $\text{C}_5\text{H}_8\text{O}_2$ )	1.86	33.5	5.0	0.080	3.70
Polystyrene ( $\text{C}_8\text{H}_8$ )	1.05	18.3	4.96	0.077	3.82
$^4\text{He}$	0.19	15.2	4.9	/	4
$^9\text{Be}$	1.85	22.2	4.3	/	9
$^{12}\text{C}$	2.26	24.9	4.1	/	12
$^{24}\text{Mg}$	1.74	27.8	3.2	/	24

(\*) 1.013 bar at boiling point, (\*\*\*) liquid phase.

Table 3 List of the materials considered in the analysis with their relevant properties: density, depth of the fluence build-up maximum  $z_{\text{max}}$ , value in percent of the fluence of  $^{11}\text{C}$  particles normalized to the incoming fluence of  $^{12}\text{C}$  particles at the depth of the maximum  $\Phi_{^{11}\text{C}}(z_{\text{max}}) / \Phi_{^{12}\text{C}}(0)$ , fraction by weight of hydrogen atoms  $f_{\text{H}}$ , and effective atomic mass  $A_{\text{eff}}$ . For compounds, the  $^{11}\text{C}$  build-up maximum is high in materials having high fraction by weight of hydrogen atom, being the highest in a pure liquid hydrogen target (cf. Figures 2 and 3, paper I). Materials are sort out in order of increasing  $A_{\text{eff}}$ .

For  $^{10}\text{C}$  ion the build-up maximum is reduced to about the 1.5% of the primary  $^{12}\text{C}$  ion fluence, while for  $^9\text{C}$  ions the production is below 0.07% for the liquid hydrogen target. The build-up maximum for  $^{15}\text{O}$  is about 6.5%, while for  $^{14}\text{O}$  is about 1% for the liquid hydrogen target. In all the other materials production maxima are lower. Calculations for  $^{10}\text{B}$  ions in liquid hydrogen and deuterium are comparable have produced a yield of about 0.03%.

As a result of the conducted investigations, the most natural choice would be to consider a production target of pure liquid hydrogen for  $^{11}\text{C}$  ion beam production. However, due to the sophisticate cryogenic system which would be needed for such thick liquid hydrogen target (about 170 cm) (Figure 3, paper I) and, more importantly, because of the large emittance of the  $^{11}\text{C}$  beam (see Section 3.4), a more practical and cost effective solution was envisaged: a two component production target constituted of a first liquid hydrogen section followed by a polyethylene section of variable length. Another plastic material with high hydrogen content might be an equally good choice.

In Figure 8, the build-up of the  $^{11}\text{C}$  fragments is shown for a variable section of liquid hydrogen followed by polyethylene as a function of the depth in the target. As seen, the  $^{11}\text{C}$  fragment build-up has a further increase in the polyethylene section (cf. also Figure 9, paper III). The increase in the production yield maximum of the  $^{11}\text{C}$  fragments as a function of the increasing length of the liquid hydrogen section is also clearly seen.

The purpose of using the liquid hydrogen section is therefore to boost the  $^{11}\text{C}$  ion production. The polyethylene section may consist of plane parallel slabs used to reduce the mean energy of the outgoing  $^{11}\text{C}$  ion beam to the desired mean energy level in order to reach the desired tumor depth. Binary increasing thickness of polyethylene (1 mm, 2 mm, 4 mm, ..., 128 mm) may be combined for reaching any desired thickness from 1 mm to 255 mm with only 8 layers. If the  $^{11}\text{C}$  ion production method is applied to synchrotron based facilities, the polyethylene part might not be necessary since the energy of the beam is directly changed at the accelerator level. It would then be sufficient to use a fixed 20 cm liquid hydrogen section and vary the extracted energy.

In Table 4 the fluence build-up of the  $^{11}\text{C}$  fragments and the  $^{11}\text{C}$  mean energy at the exit of the liquid hydrogen portion, as well as the  $^{11}\text{C}$  fluence build-up maximum are given for a variable length of the liquid hydrogen section ranging from 20 to 70 cm. The limit cases of pure liquid hydrogen and pure polyethylene target (0 cm of  $\text{H}_2$ ) are also reported in the table for completeness. The mean energy of the  $^{11}\text{C}$  ion beam at the exit of the liquid hydrogen section ranges, as a function of the liquid hydrogen section length, from about 370 MeV/u to 300 MeV/u for a primary  $^{12}\text{C}$  ion beam mean energy of 400 MeV/u corresponding to a range in water ranging from about 22 to 15 cm. Therefore, the use of a thinner section of liquid hydrogen would allow exploiting a larger energy range for treatment and should be preferred.

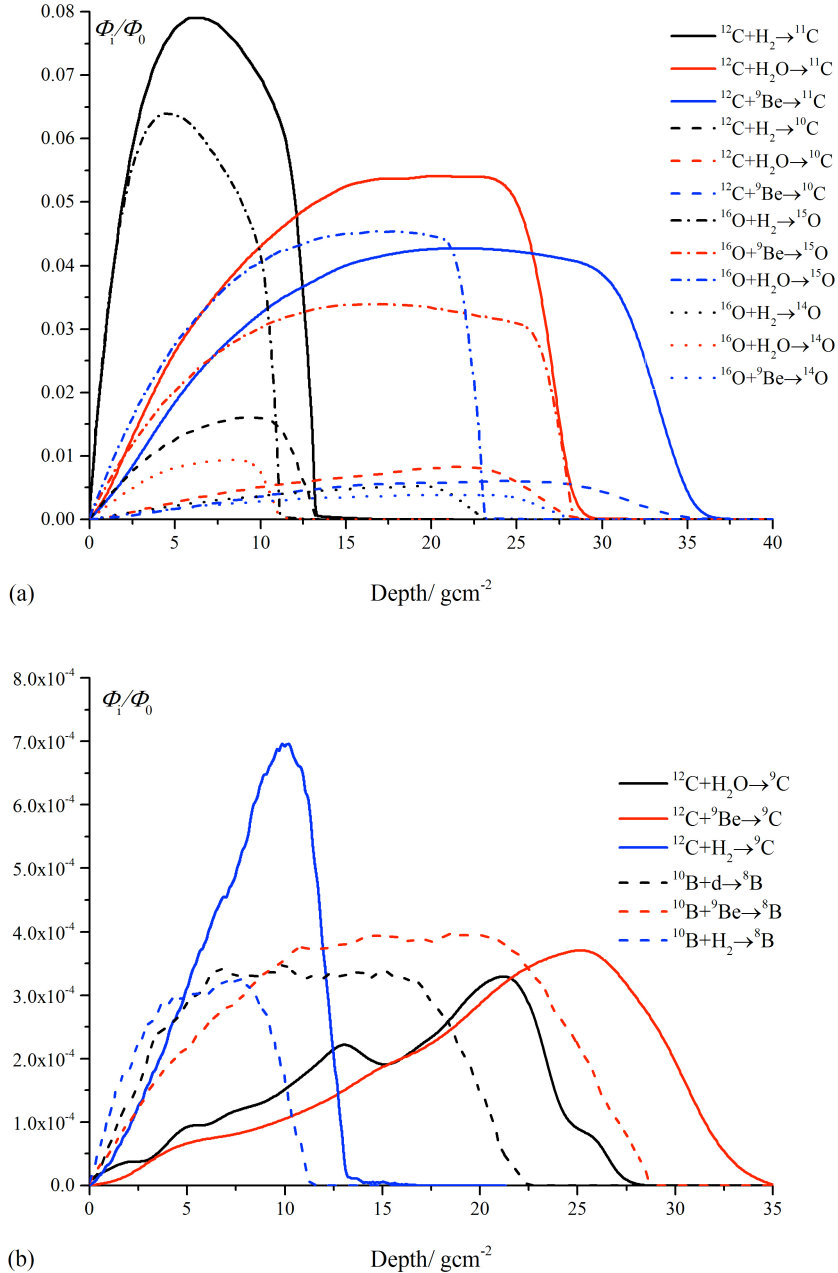


Figure 7 The fluence build-up of  $^{10,11}\text{C}$  and  $^{14,15}\text{O}$  positron emitter beams produced by  $^{12}\text{C}$  ( $\bar{E} = 400 \text{ MeV/u}$ ) and  $^{16}\text{O}$  ( $\bar{E} = 430 \text{ MeV/u}$ ) irradiation (a), and  $^9\text{C}$  and  $^8\text{B}$  ions produced by primary  $^{12}\text{C}$  and  $^{10}\text{B}$  ( $\bar{E} = 325 \text{ MeV/u}$ ) primaries (b) as a function of the depth in liquid hydrogen ( $\rho \approx 0.071 \text{ g/cm}^3$ ), liquid deuterium ( $\rho \approx 0.162 \text{ g/cm}^3$ ), beryllium ( $\rho \approx 1.85 \text{ g/cm}^3$ ) and water ( $\rho \approx 1.00 \text{ g/cm}^3$ ) targets.

H <sub>2</sub> section cm	$\bar{E}_{\text{H}_2\text{exit}}^{11\text{C}}$ MeV/u	$\Phi_{\text{H}_2\text{exit}}^{11\text{C}} / \Phi_0^{12\text{C}}$	$\Phi_{\text{max}}^{11\text{C}} / \Phi_0^{12\text{C}}$
0 ( $\equiv \text{C}_2\text{H}_4$ )	/	/	0.056
20	370	0.038	0.061
25	365	0.046	0.062
30	360	0.052	0.064
35	350	0.057	0.065
50	330	0.069	0.070
70	297	0.077	0.077

Table 4 The mean energy of the  $^{11}\text{C}$  ion beam and the  $^{11}\text{C}$  fluence normalized to the incoming fluence of the primaries at the exit of the liquid hydrogen section and the  $^{11}\text{C}$  fluence build-up maximum are given as a function of the thickness of the liquid hydrogen section. Values were extracted from Monte Carlo calculation (cf. Figure 8 of this report and Figure 9 of paper III). Error on the values reported in the table is about 5%.

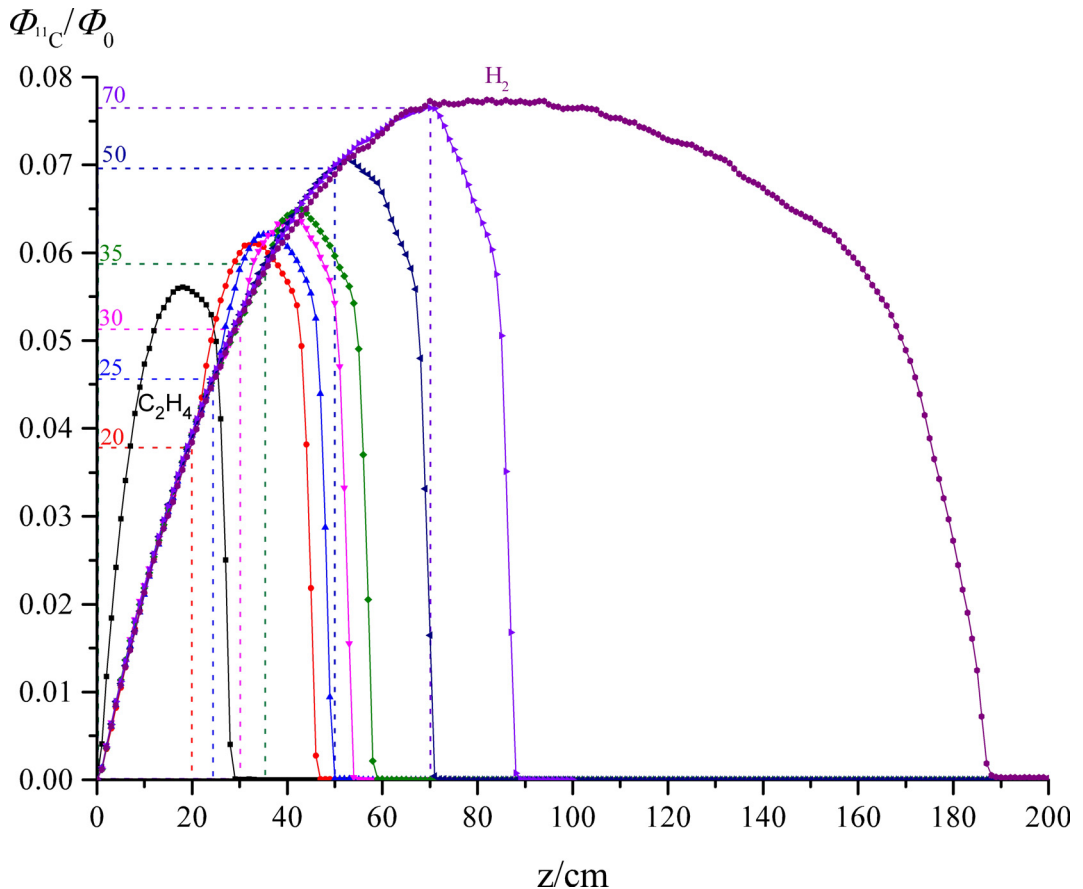


Figure 8 The  $^{11}\text{C}$  fluence build-up normalized to the incoming fluence of primary  $^{12}\text{C}$  particles is presented for a composite decelerator made of a first liquid hydrogen section of variable thickness (0-70 cm) followed by polyethylene, as well as for a pure liquid hydrogen target and a pure polyethylene target.

### 3.4 RADIAL AND ANGULAR SPREAD OF THE $^{11}\text{C}$ ION BEAM AS A FUNCTION OF THE TARGET MATERIAL

It is well known that the fragments have a larger energy spectrum and emittance as compared to primary particles (Kempe and Brahme, 2010b). The larger the spread of the beam, the lower the resulting fragment yield available for treatment at the exit of a beam line with limited angular, radial and energy acceptances (cf. Figure 5, paper III).

In paper III, the energy, angular and radial distributions of the  $^{11}\text{C}$  ion beam are studied as the material composing the target varies. The selection of the target material requires a compromise in the optimization of the characteristics of the beam, which are based on the interplay of several physical parameters.

The analytical investigation conducted in this work was based on the solution of the Boltzmann equation for primary light ions and generated fragments derived by (Kempe and Brahme, 2010b). Aim of the analytical investigation is to support the Monte Carlo simulations in guiding the analysis and understanding the results.

The primary particle transport is based on a two component Gaussian solution, which separates the particle transport in its longitudinal and lateral components, i.e. the attenuation of the primary particle with the depth in the target and their lateral spread, respectively (Kempe and Brahme, 2010) (equation (1) in paper III). For a general understanding of the variation of the angular and radial spread for the heavier fragments (such as the  $^{11}\text{C}$  ions) as a function of the material composing the target, it might be sufficient, in a first approximation, to consider the depth dependent distributions for the primary particle case. A more accurate and complex description of the solution of the Boltzmann equation for the transport of secondary fragments in the medium is given by (Kempe and Brahme, 2010b).

The mean square angular spread of primary ions at the depth  $z$  in the target can be described by:

$$\overline{\theta_p^2(z)} = \overline{\theta_p^2(0)} + \int_0^z T_p(E_p(u)) du, \quad (7)$$

where  $\overline{\theta_p^2(0)}$  is the mean square angular spread at the surface. The mass scattering power  $T_p$  describes the increase of the mean square angle of divergence per unit distance travelled and it is calculated for the energy  $E_p$  that corresponds to the depth  $u$  along the  $z$  axis (Kempe and Brahme, 2008). (Kempe and Brahme 2010) define a the mass scattering power in case of light ions based on a modified version of the mass scattering power for electrons (ICRU, 1984):

$$\frac{T}{\rho} = \frac{1}{\rho} \frac{d\overline{\theta^2}}{dl} = \frac{4\pi N_A}{M_A} \left[ \frac{m_e r_e Z_{p,\text{eff}} Z_A}{(1+\tau) \beta^2 M_p} \right]^2 \left[ \ln \left( \frac{\theta_m^2}{\theta_\mu^2} + 1 \right) + \left( \frac{\theta_m^2}{\theta_\mu^2} + 1 \right)^{-1} - 1 \right], \quad (8)$$

where  $l$  is the path length of the particle,  $N_A$  is the Avogadro's number,  $r_e$  is the classical electron radius,  $m_e$  is the electron mass,  $M_p$  is the molar mass of the primary ion,  $\tau$  is the ratio between the kinetic and the energy at rest of the projectile ion,  $\beta = v/c$  is the velocity of the incoming ion normalized to the speed of light,  $\theta_\mu$  is the screening angle due to the screening of the nucleus by orbital

electrons and  $\theta_m$  is the cut-off angle due to the finite size of the nucleus. For a given projectile and velocity, media having lower  $Z_A^2 / M_A$  deflect the particle trajectory less significantly than others. Thus, in case of an incoming  $^{12}\text{C}$  ion beam of a fixed energy per nucleon, among the materials considered in this study, the mass scattering power is the lowest in the hydrogen case. As a consequence, it is also expected that the angular variance is the lowest in the case of hydrogen compared to other light materials, if the same depth in the material is considered. The mean square radius at depth  $z$  is described by:

$$\overline{r_p^2}(z) = \overline{r_p^2}(0) + 2\overline{r\theta_p}(0)z + \overline{\theta_p^2}(0)z^2 + \int_0^z (z-u)^2 T_p(E_p(u)) du, \quad (9)$$

where  $\overline{r_p^2}(0)$ ,  $\overline{\theta_p^2}(0)$ ,  $\overline{r\theta_p}(0)$  are respectively the mean square radial spread, the mean square angular spread and covariance at the surface of the primary incident beam.

The mean covariance of the radial and angular spread describes the increase in the most probable inclination of the particles of the beam at increasing off-axis positions. The mean covariance at depth  $z$  in the case of primary particles is given by the following equation (Kempe and Brahme, 2010b):

$$\overline{r\theta_p(z)} = \overline{r\theta_p(0)} + \overline{\theta_p^2(0)}z + \int_0^z (z-u) T_p(E_p(z-u)) du. \quad (10)$$

The lateral and angular distribution of the beam can be described in terms of effective extended source. The effective extended source is defined as the source which in vacuum produces the same fluence differential in energy and angle as the real beam and it is located at a point  $s_{\text{eff}} \equiv \overline{r\theta(z)}/\overline{\theta^2(z)}$  (ICRU, 1984). The size of the effective particle source is defined by (ICRU, 1984):

$$\overline{r_{\text{eff}}^2} \equiv \overline{r^2(z)} - \overline{r\theta(z)}^2 / \overline{\theta^2(z)}. \quad (11)$$

In papers III and IV, the comparisons of the characteristics of the secondary  $^{11}\text{C}$  ion beam generated from an incoming 400 MeV/u  $^{12}\text{C}$  ion beam in the different target materials are shown for the same  $^{11}\text{C}$  ion mean energy ( $\overline{E}_{^{11}\text{C}} \approx 200\text{MeV/u}$ ). Thus, different depths are considered in the different target materials, as reported in Table I of paper III. The lower the mean energy of the secondary beam, the more the beam is degraded in terms of angular, radial and energy distribution spreads. Therefore, the  $^{11}\text{C}$  ion mean energy of about 200 MeV/u has been considered as a fair level for comparisons between the different target materials, even though it is a rather low energy for treatment with carbon ions (about 8 cm of range in water).

Results in paper III show that a pure liquid hydrogen target, although it has the lowest multiple scattering (cf. equations (7) and (8)) and the lowest angular spread, it has at the same time the highest radial spread (Figure 6, paper III). On one hand, the angular deflection is kept low along the target depth, due to the low density and the low number of atoms per unit volume, which consequently entails also a reduced number of collisions with the atoms in the medium and a lower multiple scattering. On the other hand, the  $^{11}\text{C}$  ion beam is transported with minimal attenuation at a long distance with consequent expansion of the radial distribution (cf. equation (9)). Therefore, even small initial deflections are

magnified by the deep penetration of the ions causing an increase of the effective source size (cf. equation (11)).

Results on the angular spread have shown values below  $1^\circ$  for all the considered materials: about  $0.95^\circ$  for the heaviest magnesium and about  $0.65^\circ$  for liquid hydrogen for depths in the different targets corresponding to the  $^{11}\text{C}$  ion mean energy of about 200 MeV/u (Figures 3 and 4 in paper III).

The acceptance criteria for a clinically useful beam considered in this work are: an energy spread less than 1%, an angular spread less than  $1^\circ$  and a radial spread less than 0.5 cm in radius.

Results on the variation of the radial spread as a function of the thickness of the liquid hydrogen section followed by polyethylene are presented in Figures 6(b), 7 and 8 of Paper III for a depth in the targets corresponding to ( $\bar{E}^{11}\text{C} \approx 200\text{MeV/u}$ ). For a 20 cm liquid hydrogen the radial spread can be confined below 1 cm of diameter with an almost negligible loss in the fragment yield.

Figure 9 shows a further comparison of the variation of the  $^{11}\text{C}$  ion beam production as a function of the depth for a target made of pure liquid hydrogen (solid lines) and a target made of 20 cm of liquid hydrogen followed by polyethylene (dashed lines) for a radial acceptance of the beam equal to 1, 1.5, 10 cm in diameter. As seen in Figure 9, for the composite decelerator made of liquid hydrogen and polyethylene a negligible difference is seen in the production yield as a function of the limited radial acceptance at any depth in the target.

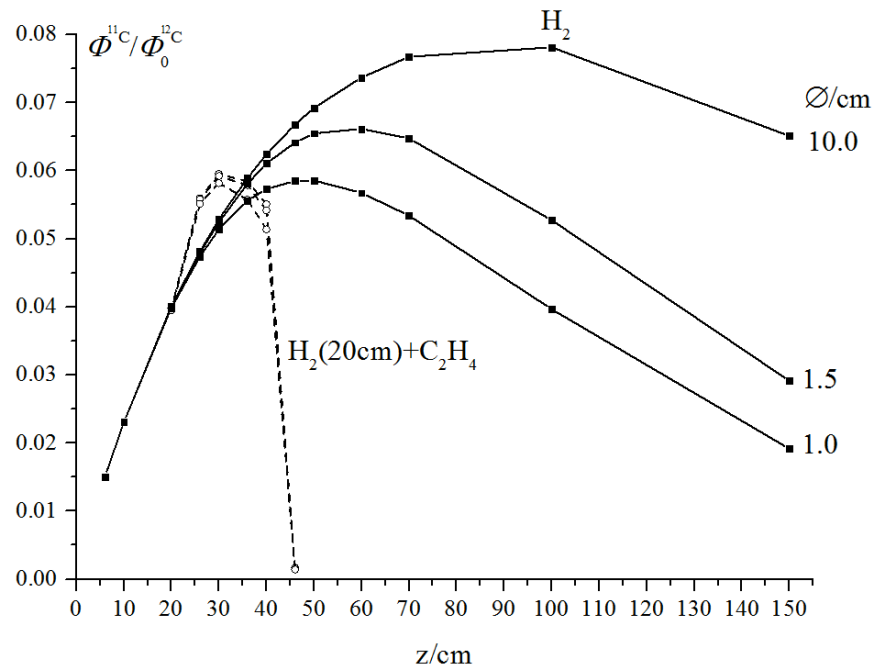


Figure 9 Comparison of the variation of the  $^{11}\text{C}$  ion beam production as a function of the depth for a target made of pure liquid hydrogen (solid lines) and a target made of 20 cm of liquid hydrogen followed by polyethylene (dashed lines) for a radial acceptance of the beam equal to 1, 1.5, 10 cm in diameter. With the composite decelerator the radial spread of the  $^{11}\text{C}$  ion beam is roughly confined below 1 cm in diameter for any depth.

## 3.5 REDUCTION OF THE ENERGY SPREAD

### 3.5.1 Energy distribution of fragments

The width of the energy distribution of the fragments produced by the slowing down of the  $^{12}\text{C}$  ion beam can be separated in three components due to three different physical effects: the energy loss straggling, the nuclear reaction process, and the different stopping power of primaries and generated fragments (cf. (Bimbot, 1988)).

#### *Energy straggling*

The energy loss of an incoming particle penetrating a medium is a stochastic process. The amount of energy loss in each individual interaction is a local value characterized by a probability distribution around a mean energy loss value (Rossi, 1952). A particle of energy  $E_0$  that penetrates a path length  $z$  has a certain probability of losing an energy  $\Delta$ , which can be approximated with a Gaussian distribution (Rossi, 1952; ICRU, 1993):

$$F(\Delta, z) = \frac{1}{\sqrt{2\pi\sigma_E^2}} \exp\left(-\frac{(\Delta - \Delta_{av})^2}{2\sigma_E^2}\right), \quad (12)$$

where  $\Delta_{av}$  is the mean energy loss value and  $\sigma_E$  is the standard deviation of the Gaussian distribution function. The corresponding variance  $\sigma_E^2$  is given by:

$$\sigma_E^2 = \frac{4\pi r_E^2 (m_e c^2) N_A Z_A Z_p^2}{(1 - \beta^2) M_A} \left[ 1 + 2 \left( \frac{m_e}{M_0} \right) (1 - \beta^2)^{-\frac{1}{2}} + \left( \frac{m_e}{M_0} \right)^2 \right]^{-1} z, \quad (13)$$

as described in (Rossi, 1952; ICRU, 1993).

For a certain projectile, velocity and depth, materials having lower  $Z_A/M_A$  ratio are expected to produce a lower energy straggling. Thus, the energy straggling in hydrogen ( $Z_A/M_A$  numerically very close to 1) is the highest compared to other light materials. Therefore, from an energy spread point of view, a high atomic number decelerator produces less energy spread and, thus, it is more advantageous.

In case of fragments, the energy straggling contribution to be considered is dual and it results both from the energy straggling of the fragments themselves and also from the energy straggling of the primary particles, whose contribution varies according to the depth of production of the fragments.

#### *Nuclear reaction kinematics*

Several approaches have been used to model the nuclear component, mainly focused in the description of the longitudinal component of the momentum, which is the largest fraction of the linear momentum in a projectile fragmentation reaction (Meierbachtol *et al.*, 2012). In the early statistical model developed by (Goldhaber, 1974; Goldhaber and Heckman, 1978), the standard deviation of the

Gaussian shaped momentum distribution of the fragments ( $\propto \exp(-p^2/2\sigma_{||i}^2)$ ) along the penetration depth of the beam is related to the momentum of the nucleons inside the projectile at the time of the reaction. One of the main assumptions of the model is that the velocity of the projectile and fragment are the same. The momentum distribution of the produced projectile-like fragments is determined by the Fermi motion of the abraded nucleons (Müzenberg, 1992) and it can be described as a function of the mass number of the projectile  $A_p$  and fragment atoms  $A_i$ :  $\sigma_{||i} = \sigma_0 \sqrt{A_i(A_p - A_i)/(A_p - 1)}$ , where  $\sigma_0 \approx p_f/\sqrt{5} \approx 90 \text{ MeV}/c$  is the so called reduced momentum width and  $p_f$  is the Fermi momentum. Assuming that the projectile nucleons have a mean square momentum in the projectile frame equal to  $\sigma_0 \approx \sqrt{3/5} p_f$ , the expected momentum dispersion is  $\sigma_0 \approx \sqrt{1/5} p_f$  (Ma, 2002). For example, for  $^{11}\text{C}$  fragments generated by  $^{12}\text{C}$  primary particles, the expected momentum dispersion along the penetration depth is reduced to  $\sigma_{||i} \equiv \sigma_0$ . In Goldhaber's model the Fermi motion is considered to be the major contribution to the fragment momentum distribution (Bacquias *et al.*, 2012). (Morrissey, 1989) derives a similar scaling formula from experimental data and valid in the approximation of small mass losses:  $\sigma_{||i} = \sigma_0 \sqrt{A_p - A_i}$ , where  $\sigma_0$  is a constant which should be fitted from experimental data, values of the constant are reported, for example, by (Meierbachtol *et al.*, 2012).

Alternative semi-empirical or fully theoretical models are also described in the literature in order to determine the dispersion of the longitudinal momentum distribution (Tarasov, 2004; Bacquias *et al.*, 2012). Tarasov and co-workers introduce a “universal parameterization” model where a semi-empirical formula is used to calculate the momentum distribution of the fragments. The model considers the convolution of a Gaussian function with an exponential tail in the low energy side and it is capable to describe the velocity ratio between the projectile and the fragments (Tarasov, 2004). Bacquias and co-workers describe a model fully based on theoretical considerations, which takes into account the different fragmentation reaction processes. They define a mass limit for multifragmentation and derive different equations according to the fragment mass with respect to mass limit value (Bacquias *et al.*, 2012). When fragments having a mass close to the projectile are produced the multifragmentation do not occur and the total momentum dispersion is the sum in quadrature of the Fermi motion contribution and the recoil induced by evaporation (Bacquias *et al.*, 2012).

### *Differences in stopping power of projectiles and fragments*

An additional contribution to the increase of the energy spread is due to different depth of production of projectile-like fragments in the target. Depending on the target depth at which the fragments are produced, they have different energy and they are transported in the medium traversing a different length with a stopping power that differs from the projectiles to the fragments. In other words, secondary fragments produced near the first layers of the target travel through the rest of the

target as different species experiencing a different stopping power than the primary ions beam which fragmentates near the last layers of the target. This process results in an additional contribution to the widening of the energy spread (Bimbot, 1988). The contribution of this term to the resulting energy spread increases as the target thickness increases and it might become the predominant term (Bimbot, 1988).

From results shown in paper III, the energy spread of the  $^{11}\text{C}$  ion beam calculated for the different target materials at the depths corresponding to a mean energy of the  $^{11}\text{C}$  ion beam of 200 MeV/u is almost the same (cf. Figures 1 and 2(b) in paper III) and it is equal to about 12 MeV/u of FWHM. The standard deviation of the energy distributions only minimally decreases as a function of  $A_{\text{eff}}$  (Figure 2(b) of paper III).

In paper III, a characterization of the shape of the energy distribution was also performed by calculating higher order momenta above the mean energy and variance, such as the skewness (momentum of order III) and kurtosis (momentum of order IV):

$$M_i = \frac{\int_0^{\infty} (E - \bar{E})^i \Phi_E dE}{\sigma^i \int_0^{\infty} \Phi_E dE}, \quad (14)$$

where  $\bar{E}$  is the mean energy value (first moment) and  $M_{i=II,III,IV}$  is the  $i^{\text{th}}$ -moment of the distribution. A larger scattering of the data as a function of the effective molar mass is observed for the higher order momenta (skewness and kurtosis). For the composite decelerator made of 20 cm of liquid hydrogen followed by polyethylene, the energy spread ( $\Delta E / \bar{E}$ ) ranges from 5% for  $\bar{E}_{^{11}\text{C}} \approx 370\text{MeV/u}$  at the exit of the liquid hydrogen section to about the 20% for  $\bar{E}_{^{11}\text{C}} \approx 150\text{MeV/u}$  (Figure 10 (a)).

### 3.5.2 The variable wedge-shaped degrader

To reduce the large energy spread of the  $^{11}\text{C}$  positron emitter beam, a wedge-shaped degrader of variable thickness is intended to be used at the first dispersive focal point of the beam line, as shown in Figure 12. Even though with a wedge-shaped degrader the accuracy in the momentum compression of, for example, the electron cooling technique (cf. Section 3.2) is not achievable and it entails second order effects which have to be corrected for, (such as a loss of the beam intensity with consequent production of contaminating particles and increase of the ion beam emittance), it does not require the presence of storage rings and electron cooling (Müzenberg, 1992; Geissel *et al.*, 2002), thus being a more cost effective solution.

The wedge-shaped degrader is used in a monochromatic configuration (Geissel *et al.*, 1992) and its thickness  $t_{^{11}\text{C}}$  is calculated with the following equation derived from the energy-range relation described by (Kempe and Brahme, 2008):

$$t_{^{11}\text{C}}(E) = R_0(E) \left[ 1 - \left( \frac{E_{\min}}{E} \right)^k \right], \quad (15)$$

where  $E \in \Delta E = [E_{^{11}\text{C},\min}, E_{^{11}\text{C},\max}]$  is the energy range covered by the  $^{11}\text{C}$  ion energy distribution at the depth  $z$  in the production target (cf. Figure 10 (a)), and  $R_0(E)$  is the range correspondent to the energy  $E_0$  in degrader material (extracted from the SRIM<sup>13</sup> tables).  $k$  is a dimensionless transport parameter given by  $k = E_0/S_0 R_0$ , where  $S_0$  is the stopping power at the surface in the continuous slowing down approximation of the  $^{11}\text{C}$  ions (Kempe, 2008). The thickness of the wedge-shaped degrader is calculated so that the energy differences,  $E - E_{\min}$  with  $E \in [E_{^{11}\text{C},\min}, E_{^{11}\text{C},\max}]$  are compensated by the different path lengths of the ions in the degrader material (Geissel *et al.*, 1989). The resulting  $^{11}\text{C}$  ion energy distribution is therefore centred on the minimum value ( $E_{^{11}\text{C},\min}$ ) of the  $^{11}\text{C}$  ion incoming energy distribution range (cf. Figure 11).

The calculated wedge-shaped profile depends on the energy distribution of  $^{11}\text{C}$  ions at the exit of the production target (Figure 10 (b)), as well as on the degrader material (Schwender, 2011). For lower  $^{11}\text{C}$  ion mean energy the curvature of the wedge-shaped profile becomes more accentuated, due to the stopping power departure from linearity at lower energies. In order to select the degrader material, a compromise is unavoidable. In fact, the energy loss straggling (equation (13)) and the multiple Coulomb scattering (equations (7) and (8)) are minimized by high and low atomic number materials, respectively. Beryllium was chosen as a good compromise between the two competing effects (Anferov, 2003). However, carbon may also be an alternative (Van Goethem *et al.*, 2009).

In order to analytically calculate the  $^{11}\text{C}$  ion energy distribution at the exit of the wedge-shaped degrader, both energy straggling and the attenuation of the  $^{11}\text{C}$  ion beam through the degrader are taken into account. The outgoing  $^{11}\text{C}$  ion energy distribution is described as the build-up of the sum of Gaussian-like kernels having intensity equal to the attenuated intensity and spread given by the energy straggling component (cf. equations (5), (8), (9) and Figure 5, paper IV). Further details on the analytical method adopted to finalize the calculation are given in Section 2.4 of paper IV.

---

<sup>13</sup> <http://www.srim.org/>

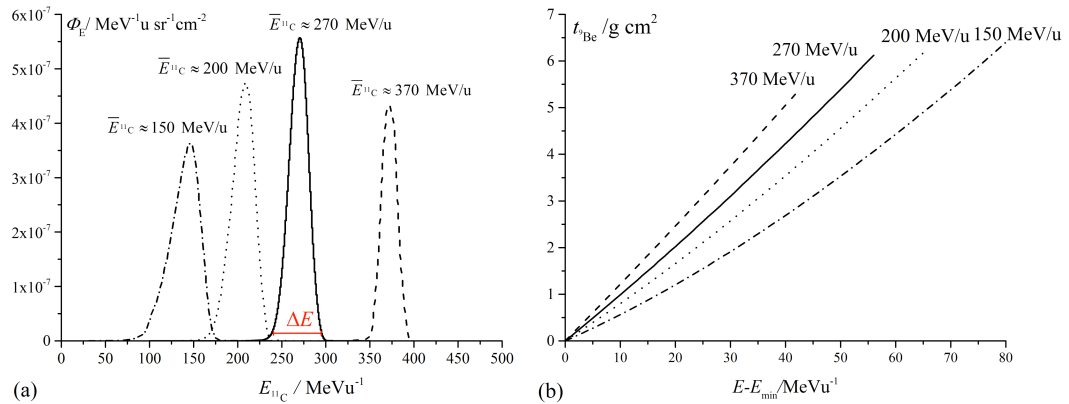


Figure 10  $^{11}\text{C}$  ion energy distributions (a) and corresponding beryllium wedge-shaped profiles (b) for a target made of 20 cm liquid hydrogen followed by polyethylene. The profile of the variable wedge-shaped degrader is calculated so that the energy differences  $E - E_{\min}$  are compensated by the different path lengths of the ions in the material composing the degrader (Geissel *et al.*, 1989).

In Figure 11, the incoming energy spread extracted from Monte Carlo data and the analytically calculated energy distributions are shown for an incident mean energy of  $^{11}\text{C}$  ion beam of 270 MeV/u for a composite decelerator made of 20 cm liquid hydrogen followed by polyethylene at a depth corresponding to 11 g/cm<sup>2</sup>. The calculated energy spread of the  $^{11}\text{C}$  ion beam at the exit of the degrader is about the 1% of the  $^{11}\text{C}$  ion mean energy. The loss in the  $^{11}\text{C}$  yield due to the attenuation in the wedge is about the 14% for the configuration shown in Figure 11. For the energy distributions shown in Figure 10 (a) corresponding to a  $\bar{E}_{^{11}\text{C}} \approx 150-370 \text{ MeV/u}$  the loss of  $^{11}\text{C}$  particles due to the attenuation in the beryllium degrader is in the range from about 15% to 10%, respectively.

As a result of the presence of the wedge-shaped degrader, the range of exploitable  $^{11}\text{C}$  ion mean energy for treatment is reduced from about 370 MeV/u to about 350 MeV/u. Therefore, an increase of the primary  $^{12}\text{C}$  ion initial energy above 400 MeV/u may be needed if depths more than 20 cm-water equivalent have to be treated. However, not many tumors are located at such depths (Noda *et al.*, 2007) and, for skin and normal tissue sparing in the entrance channel of the beam, usually cross fields from other directions that might not need such a long penetration depth may be sufficient. A direct solution in order to increase the mean energy of the  $^{11}\text{C}$  ion beam would be to reduce the liquid hydrogen section of the decelerator, however, this would unavoidably entail a loss in the intensity of  $^{11}\text{C}$  ion beam.

Nevertheless, synchrotrons delivering, for example, 430 MeV/u carbon ions are already available (e.g. at the Heidelberg Ion beam Therapy center in Germany<sup>14</sup> (HIT)) and superconductive cyclotrons are in the research phase of development and might become available in the near future (Kang *et al.*, 2012). Finally, if mixed beam are used, it might not be optimal to treat the distal part of deep seated tumors with particles as heavy as carbon ions, but rather lower LET particles, such as lithium or boron ions, might be preferable (Section 2.1, (Brahme, 2011, 2012))

<sup>14</sup> <http://www.klinikum.uni-heidelberg.de>

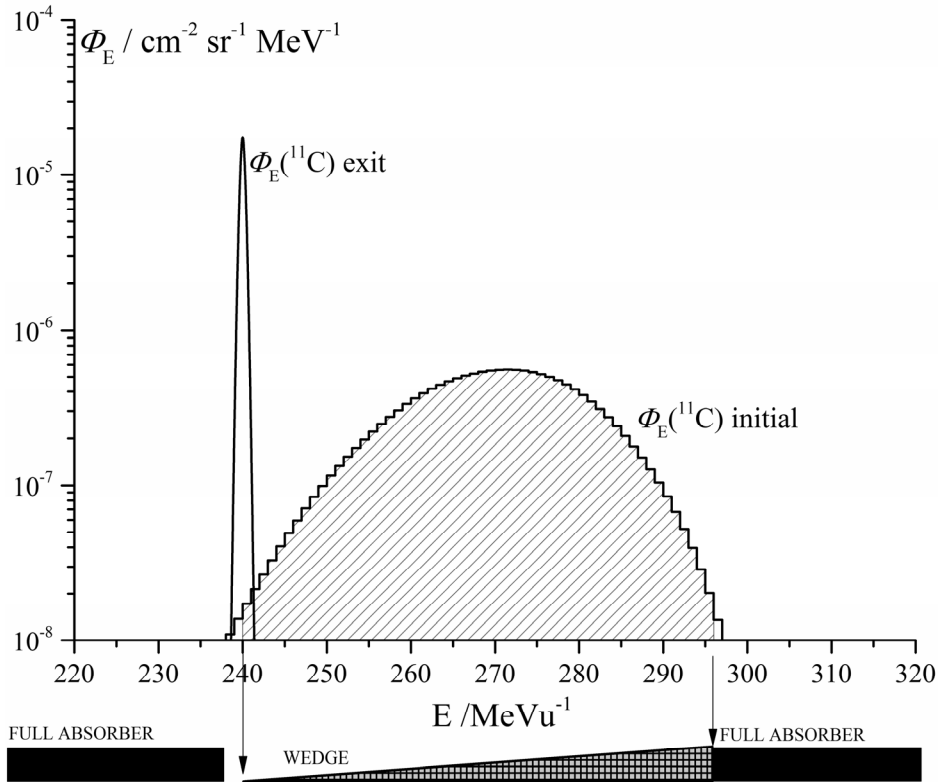


Figure 11 Energy distribution of the  $^{11}\text{C}$  fragments at the entrance and at the exit of the wedge-shaped degrader. The incoming energy distribution is simulated by the Monte Carlo code SHIELD-HIT, while the outgoing distribution is analytically calculated by considering the energy straggling effect of the beam (equation (13)) and its attenuation in the wedge-shaped degrader. The thickness of the degrader is calculated with equation (15). The contribution to the  $^{11}\text{C}$  beam intensity decrease in the beryllium degrader is extracted by fit of the  $^{11}\text{C}$  particle fluence attenuation in beryllium calculated with the Monte Carlo code SHIELD-HIT10.

### 3.6 BEAM LINE DESIGN AND PURIFICATION OF THE $^{11}\text{C}$ ION BEAM FROM OTHER CONTAMINATING FRAGMENTS

The beam line design for the production of  $^{11}\text{C}$  positron emitter beams is illustrated in Figure 12. A combination of magnetic rigidity, energy loss and TOF-velocity analysis is used in order to purify the produced  $^{11}\text{C}$  ion beam from its contaminants.

The production target consists of a fixed liquid hydrogen  $^{11}\text{C}$  ion producer (about 20 cm thick) followed by a digital decelerator and energy selector made of polyethylene slabs of variable thicknesses, as already described in Section 3.3. The optical system composing the fragment separator consists of several elements described below.

The beam size collimator slits in the initial, middle and final part of the beam line have different roles: the first pair of slits serves as a beam collimator for reducing the radial spread of the beam to values below 1 cm in diameter, whereas the last two pairs of slits, each of them located after the bending magnets, are mainly used to stop the contaminating fragments having magnetic rigidity values (and,

therefore, trajectories) different from the  $^{11}\text{C}$  particles, which are supposed to travel along the beam line axis. Two dipoles magnets with a  $45^\circ$  bending are used to purify the beam from contaminating fragments according to the magnetic rigidity of the particles (see Section 3.6.1). The variable wedge-shaped degrader (previously described in Section 3.5) is located at the first dispersive focal point of the fragment separator and it is used to both reduce the energy spread of  $^{11}\text{C}$  particles and to further separate the fragments according to their different energy loss properties. Finally, to further purify the  $^{11}\text{C}$  ion beam from contaminating fragments, a Radio Frequency-driven Time Of Flight velocity is also included in the beam line (see Section 3.6.2). Further description of the beam line components is given in paper IV, section 2.1.

The upper panel of Figure 12 schematically illustrates in more detail the transport of the particles in the beam optic system. At the exit of the production target (and decelerator), fragments are bent along trajectories having different radii according to their magnetic rigidity (cf. equations (16) and (17)). Given a certain particle type, the higher the energy of the particle the less the particle trajectory is affected by the action of the magnets. Thus, by fine tuning the position of the wedge-shaped degrader on the dispersive axis of the ion-optical system, the energy spread of the ion beam, for which the degrader is designed, is notably reduced to values almost equal to the minimum value of the energy spread, as seen in the previous Section 3.5.2. At exit of the wedge-shaped filter, particles are then focused on a pair of energy/magnetic rigidity selection slits before reaching the final bending magnet which further separates the remaining contaminants (see also Section 3.6.1).

In order to provide shielding against the high neutron fluence,  $\sim 2\text{m}$  thick concrete walls (cf. Figure 4) are included in the design of the facility. The majority of neutrons is expected to be generated in the decelerating system located upstream in the beam line (cf. Figure 2, paper IV), but also in the wedge, collimation slits etc. Since the neutron trajectories are not affected by the electromagnetic fields of the beam line, they are expected to be stopped both in the geometric labyrinth of the charged particle beam line and by radiation shielding in the excentric rotary gantry (Figure 4 and Figure 12). Further studies on the neutron contamination are therefore desirable.

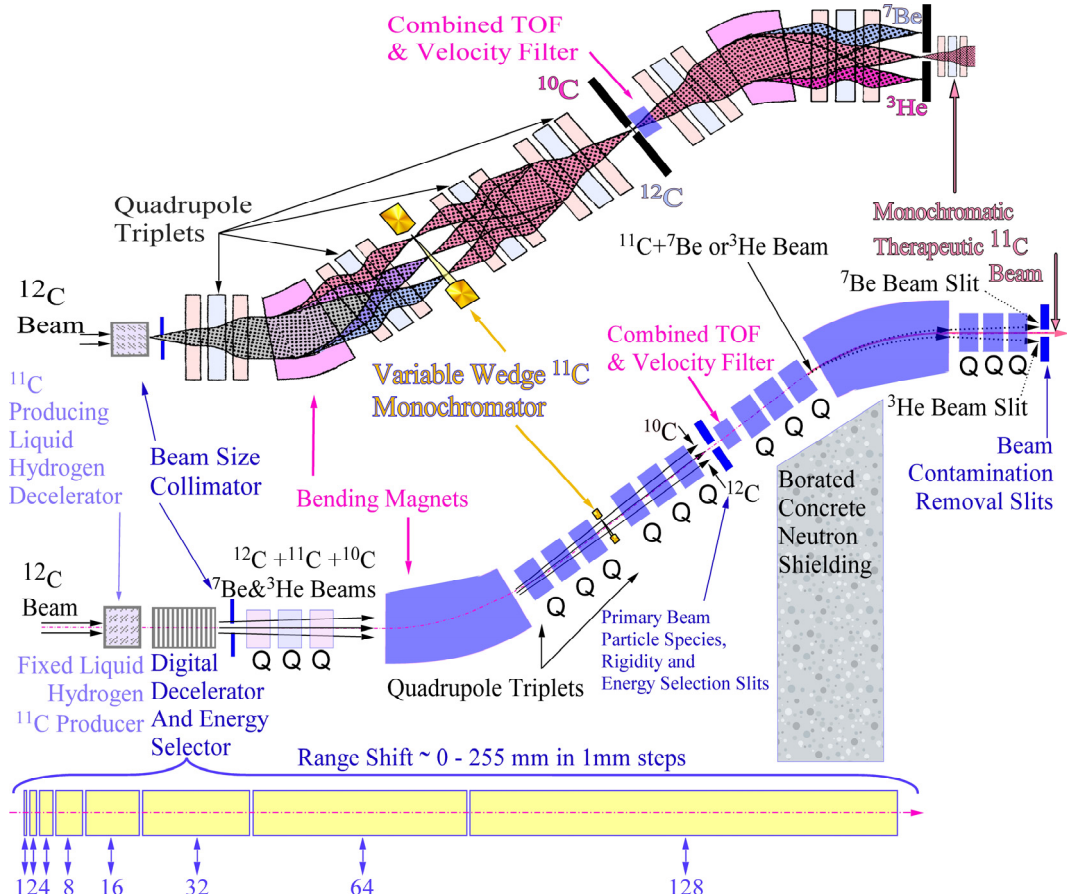


Figure 12 Illustration of the beam optical system at the entrance to the excentric gantry (Figure 4) used to produce therapeutic scanned  $^{12}\text{C}$  and  $^{11}\text{C}$  beams with less than 1% energy spread. The initial liquid hydrogen and digital polyethylene decelerator are optimal for making  $^{11}\text{C}$  positron emitter beams of high brilliance. The following bending magnets, the quadrupole triplets, the TOF and velocity filter are used to both compress the ion beam phase space density and to maintain a high intensity and brilliance with minimum contamination. The upper panel of the figure illustrates in more detail the variation of the particle trajectories according to their magnetic rigidity under the action of the wedge-shaped degrader, the magnetic dipoles and the focusing/defocusing quadrupoles. The magnetic rigidity range is here separated, for simplicity, in the low (red) and high (blue) components. The upper panel figure is modified after (Geissel *et al.*, 1989).

### 3.6.1 Magnetic rigidity filtering

The magnetic rigidity  $B\rho$  describes the resistance of a particle to a change of its direction of motion under the influence of a macroscopic magnetic field of strength  $B$ . When a particle of momentum  $\vec{p} = m_p \vec{v}$  and charge  $Z_p$  travels a path  $ds$  in the time  $dt$  in a plane perpendicular to the magnetic field  $\vec{B}$ , its motion is governed by the Lorentz's force:

$$Z_p \vec{v} \times \vec{B} = \frac{d\vec{p}}{dt} = \frac{|\vec{p}|}{\rho} \frac{ds}{dt} \rightarrow |\vec{B}| \rho = \frac{|\vec{p}|}{Z_p}, \quad (16)$$

where  $\rho$  is the radius of the particle trajectory.

where  $\rho$  is the radius of the particle trajectory.

In the relativistic limit where  $p/c = \sqrt{E^2 + 2m_p c^2 E}$ , the magnetic rigidity can be expressed as a function of the kinetic energy  $E$  (here in units of MeV/u) by the following equation:

$$\begin{aligned} B\rho(E) &= 3.3357 \cdot 10^{-3} \cdot \frac{1}{Z_p} \sqrt{2m_p c^2 EA_p + (EA_p)^2} = \\ &= 3.3357 \cdot 10^{-3} \cdot \frac{1}{Z_p} \sqrt{2mc^2 A \left[ \bar{E}_0 \left( 1 - \frac{z}{R_0} \right)^{\frac{1}{k}} \right] + \left[ A\bar{E}_0 \left( 1 - \frac{z}{R_0} \right)^{\frac{1}{k}} \right]^2} \quad (17) \end{aligned}$$

where the energy-range equation (1) in paper IV (Dufour et al. 1986, Kempe and Brahme 2008) was used.

One of the main differences between the beam line design proposed in this work from the design common to most of the in-flight fragmentation facilities is the presence of thick production target of variable thickness. Thus, a detailed analysis of the characteristics of the produced  $^{11}\text{C}$  ion beam and other contaminating fragments in terms of beam mean energy, mean magnetic rigidity and mean velocity variation as a function of the thickness of the target is required (paper IV, Figure 2 (a-d)).

In fact, the  $B\rho$ - $\Delta E$ - $B\rho$  stages are rather commonly used in the beam lines of various in-flight fragmentation facilities. The use of these three stages allows to purify the beam to a large extend. When a thin target is used, the first stage discriminates the particle according to their mass-to-charge ratio since the reaction mechanism approximately conserves the fragment velocity (cf. equations (16) and (17)) (Dufour *et al.*, 1986), while the degrader in the second stage further discriminates the particles in the previous subset of nuclei and it is roughly sensitive to  $A^{2.5}/Z^{1.5}$  as calculated by Dufour and co-workers. However, these considerations cannot be applied to our case due to the considerable thickness of the production target, which consequently entails a large variation of the velocity of the fragments at the exit of the target with respect to the production point due to their slowing down process in the material.

Figure 13 shows the mean magnetic rigidity of the particles produced in the composite decelerator (20 cm of liquid hydrogen and the remaining length made of polyethylene) as a function of the depth. As seen in Figure 13, the mean magnetic rigidity of the  $^{11}\text{C}$  fragments results in being very close to that of  $^7\text{Be}$  and  $^3\text{He}$  ions at the depths of about  $11 \text{ g/cm}^2$  and  $16 \text{ g/cm}^2$ , respectively. Therefore, for the polyethylene slab combination corresponding to those mentioned thicknesses, the  $^7\text{Be}$  and the  $^3\text{He}$  fragments are bended by the first dipole magnet along the same trajectory in the optical system as the  $^{11}\text{C}$  fragments, being therefore the most contaminating fragments.

However, even though the crossing points of the mean magnetic rigidity curves between the  $^{11}\text{C}$ - $^7\text{Be}$  ions and  $^{11}\text{C}$ - $^3\text{He}$  ions occur at the specific depths mentioned above, when the magnetic rigidity distribution of the particles (cf. Figure 3, paper IV) is taken into consideration, the crossing in the magnetic rigidity spectra is

seen almost along the whole depth in the target indicating that additional filtering techniques are surely needed (Section 3.6.2).

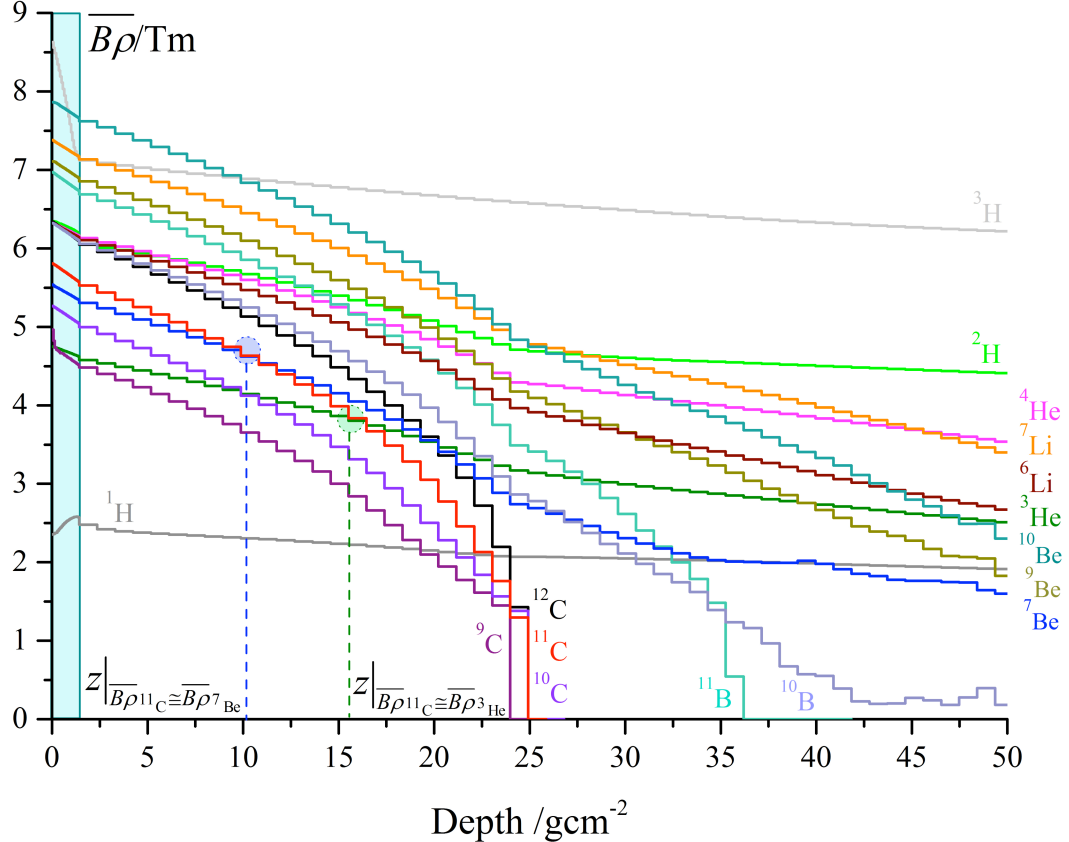


Figure 13 Variation of the mean magnetic rigidity of the particles produced in a composite target material made of 20 cm of liquid hydrogen (shaded area) followed by polyethylene as a function of the depth. At the depth of about 11 g/cm<sup>2</sup> and 16 g/cm<sup>2</sup> the mean magnetic rigidity of <sup>11</sup>C particles is approximately equal to that of <sup>7</sup>Be and <sup>3</sup>He fragments, respectively, which are then the most contaminating fragments.

Figure 14 shows the magnetic rigidity spectra for a wide range of fragments generated in the target material at the depths which correspond to the crossing points mentioned above. As seen in the Figure, a few other fragment spectra (the <sup>4</sup>He ions and, only marginally, <sup>6</sup>Li ions) additionally overlap the <sup>11</sup>C ion magnetic rigidity spectrum.

Due to the fact that a considerably larger energy spread is seen for the <sup>3,4</sup>He fragments and, furthermore, the helium isotopes are more easily separable with a velocity filtering as compared to <sup>7</sup>Be fragments (cf. Figures 16 and 17), the main concern is the contamination coming from the higher energy <sup>7</sup>Be fragments, despite the higher <sup>3</sup>He particle fluence (see Figure 2(a) in paper IV).

Figure 15 shows the magnetic rigidity distribution of the <sup>11</sup>C and <sup>7</sup>Be ions both at the entrance and at the exit of the beryllium wedge-shaped degrader. The magnetic rigidity spectra at the entrance of the decelerator are derived from the Monte Carlo calculation of the energy spectra (cf. equation (17)), whereas the outgoing spectra are derived from the analytically calculated energy spectra

taking into account both the attenuation of the particles in the wedge and the increase of the energy distribution due to the energy straggling (equation (13)), as mentioned in Section 3.5.2 for the  $^{11}\text{C}$  ion case.

For fragments other than  $^{11}\text{C}$  ions, the outgoing energy/magnetic rigidity spectra are calculated by firstly considering the portion of the spectrum in the magnetic rigidity domain which overlaps the  $^{11}\text{C}$  magnetic rigidity range (i.e. the portion of fragments which pass through the wedge and it is not stopped in the full absorbers located on both sides of the wedge). Secondly, the compression of the fragment spectrum in the energy domain is calculated by considering the decrease in the fragment energy due to the given  $^{11}\text{C}$ -degrader thickness (equation (15)).

In the lower part of Figure 15 the degrader configuration is schematically illustrated. The beryllium wedge-shaped degrader is located in between two full absorbers which are used to confine the magnetic rigidity range and prevent the contaminating fragments from decreasing the  $^{11}\text{C}$  ion beam purity.

In order to avoid the  $^{11}\text{C}$  fragments in the low rigidity side of the distribution being stopped in the absorbers at the exit of the wedge-shaped degrader, an aperture of width approximately equal to the  $^{11}\text{C}$  rigidity distribution standard deviation is also included in the design of the system  $\Delta B\rho_{\text{aperture}} = (\overline{B\rho}_{^{11}\text{C},\text{out}}, \overline{B\rho}_{^{11}\text{C},\text{out}} - \sigma_{^{11}\text{C},\text{out}}) \approx (4.333, 4.344)\text{Tm}$ .

As a consequence, the fragments (both  $^{11}\text{C}$  ions and contaminants), whose distribution in rigidity coincide with the aperture range, are free to pass unperturbed through it. Therefore, the yield of useful  $^{11}\text{C}$  fragments is increased and the beam purity is decreased.

The total yield of the  $^{11}\text{C}$  fragments at the exit of the wedge-shaped degrader is thus the sum of the integral yield of the initial distribution of the  $^{11}\text{C}$  fragments passing unperturbed through the aperture and the  $^{11}\text{C}$  distribution at the exit of the wedge-shaped degrader integrated from the lowest magnetic rigidity value allowed by the aperture ( $\approx 4.333 \text{ Tm}$ ) to the maximum magnetic rigidity value of the distribution. In the case of the  $^7\text{Be}$  fragments, the total yield is calculated by integrating the whole  $^7\text{Be}$  fragment rigidity distribution at the exit of the wedge-shaped degrader and the portion of the initial  $^7\text{Be}$  spectrum in correspondence with the aperture. The ratio of the total  $^7\text{Be}$  fragments and  $^{11}\text{C}$  ions is about 56%. However, the presence of the last slit located downstream in the beam line optics (Figure 12 and Figure 15) after the last bending magnet allows to further reducing the contamination in the  $^{11}\text{C}$  ion beam from other fragments. The extreme of the slit should be located at  $\overline{B\rho}_{^{11}\text{C},\text{out}} + \sigma_{^{11}\text{C},\text{out}}$ , as shown in Figure 15.

By taking into account the presence of the slit, the contamination of the  $^7\text{Be}$  fragments in the  $^{11}\text{C}$  ion beam is reduced to about 4%. A TOF-velocity filtering is planned to be inserted in the beam line optics to further increase the beam purity (Section 3.6.2).

Finally, by considering a limited radial acceptance of 0.5 cm and by integrating the  $^{11}\text{C}$  rigidity distribution at the exit of the wedge-shaped degrader in the acceptance limit imposed by the presence of the final slit (cf. Figure 15), the  $^{11}\text{C}$  fluence is about the 5% of the incoming  $^{12}\text{C}$  fluence for a target a target thickness corresponding to about  $11\text{g/cm}^2$  (20 cm of liquid hydrogen followed by 10 cm of polyethylene).

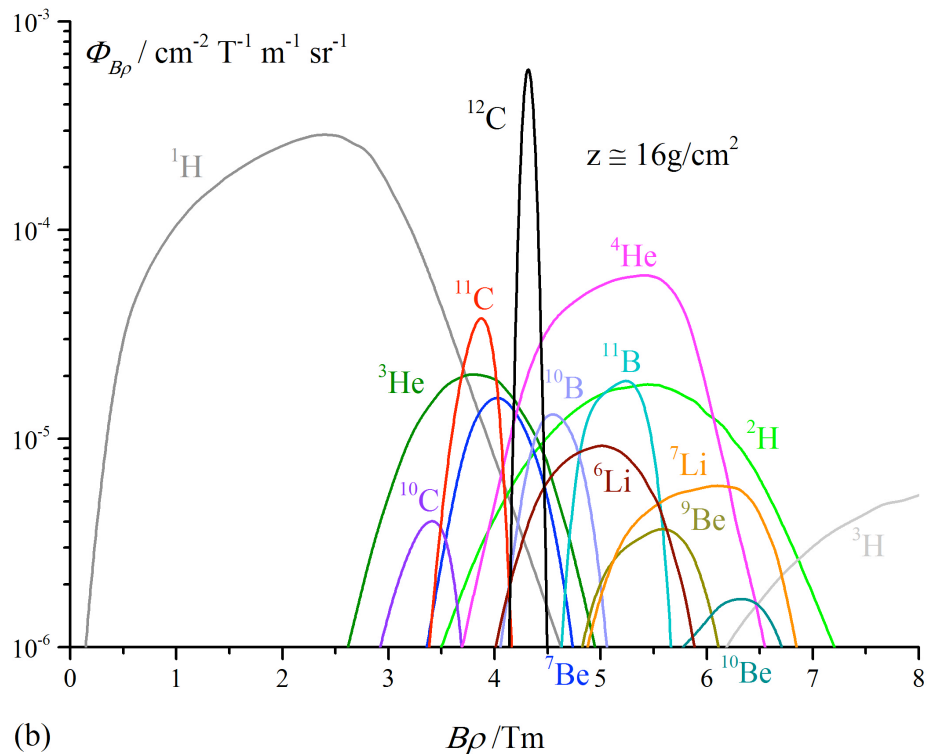
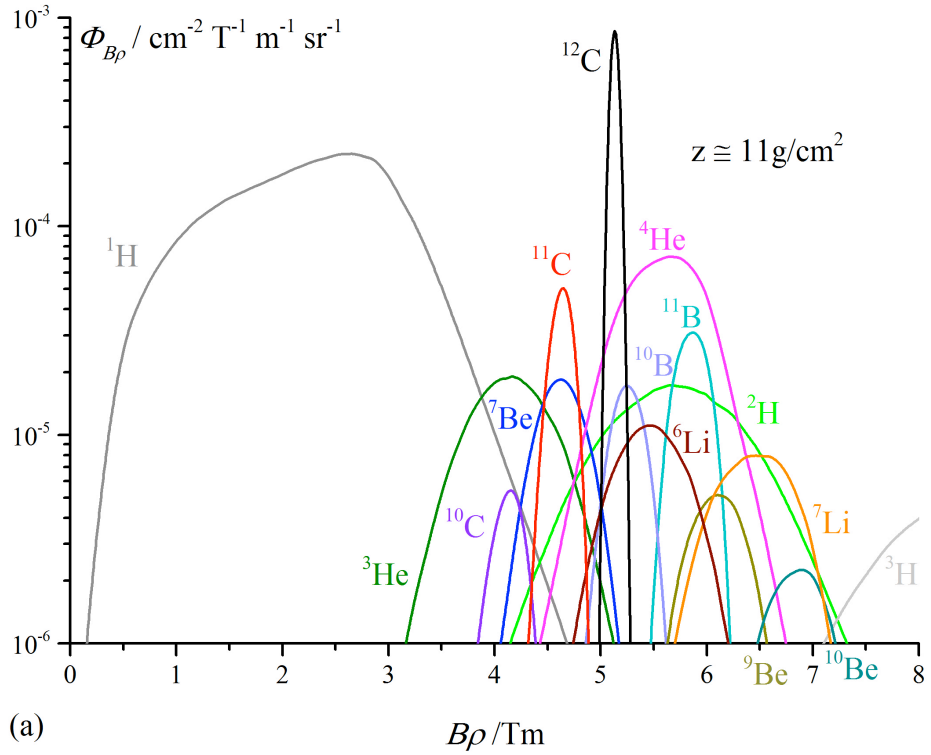


Figure 14 Magnetic rigidity spectra of fragments generated in the decelerator at  $11 \text{ g/cm}^2$  and  $16 \text{ g/cm}^2$  of depth in the target. At those depths, the contamination from, respectively,  $^7\text{Be}$  and  $^3\text{He}$  fragments is the highest. However, the spectra of other particles (such as the  $^4\text{He}$  ions and, only marginally, the  $^6\text{Li}$  ions) contribute to decrease the purity of the beam, thus making the use of additional filtering techniques unavoidable.

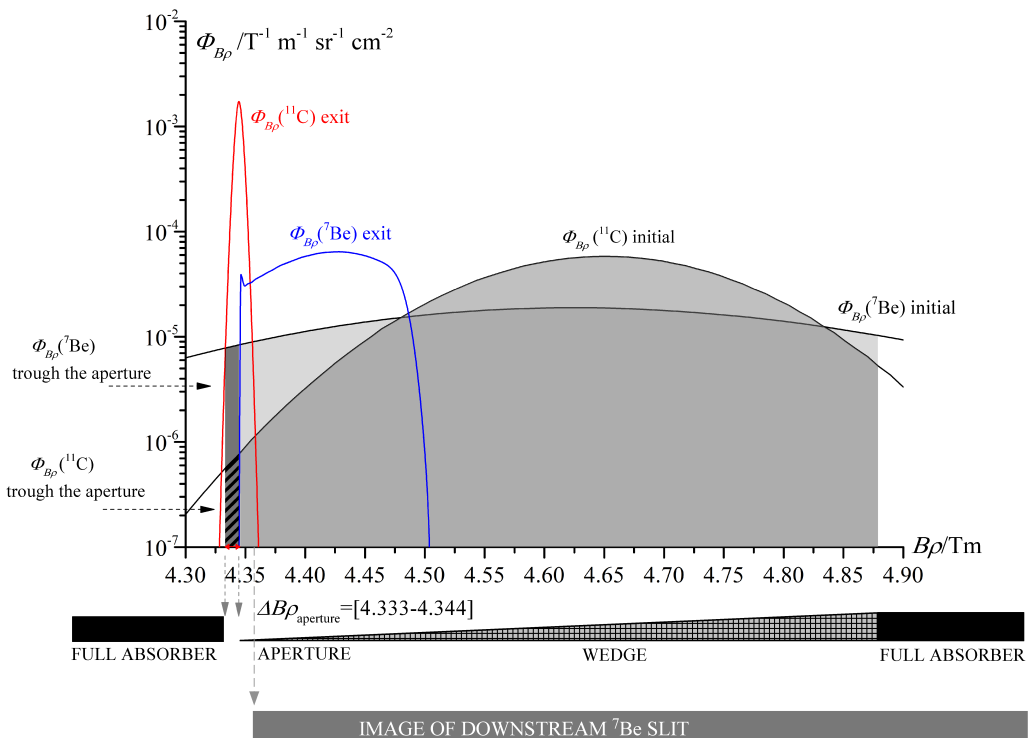


Figure 15 The magnetic rigidity distributions of the  $^{11}\text{C}$  and  $^7\text{Be}$  fragments at the exit of the wedge-shaped degrader are plotted together with the initial magnetic rigidity distributions. The wedge-shaped degrader, the full absorbers and the final downstream slit are also schematically illustrated in the lower panel of the figure. An aperture having the width approximately equal to the standard deviation of the  $^{11}\text{C}$  energy distribution is located in the low magnetic rigidity side of the wedge-shaped degrader, in order to prevent  $^{11}\text{C}$  fragments from being stopped in the full absorbers.

### 3.6.2 The Radio Frequency-driven TOF and velocity filter

In order to achieve a higher  $^{11}\text{C}$  ion beam purity than the one obtained by the sole use of the system based on the dipole magnets and the energy degrader, a novel system based on the modification of a classical Wien filter may be used for discriminate the fragments according to their velocity.

A classical Wien filter (Anne and Mueller, 1992; Wien, 1999; Nummela *et al.*, 2002) makes use of mutually perpendicular electric and magnetic fields. The electrostatic and magnetic components of the Lorentz's force  $\vec{F} = \vec{F}_E + \vec{F}_B = q(\vec{E} + \vec{v} \times \vec{B})$  have opposite directions and compensate only in case of a particle velocity equal to  $v = E/B$ . Thus, ions having the right velocity can pass undeflected through the filter and, as a consequence, a particle selection based on the velocity is achievable. The magnitudes of the electric and magnetic fields are chosen in such a way that for the  $^{11}\text{C}$  ion beam the Lorentz's force is null and the  $^{11}\text{C}$  ion beam follows a trajectory coinciding with the central axis of the beam line.

Figure 16 shows the variation of the mean velocities  $\bar{v}/c$  of the fragments generated in the combined target as a function of the depth. The most contaminating  $^7\text{Be}$  and  $^3\text{He}$  fragments have higher mean velocities with respect to the  $^{11}\text{C}$  particles for all the target thicknesses combinations, thus the separation in the velocity domain might be used to help filtering the  $^{11}\text{C}$  ion beam.

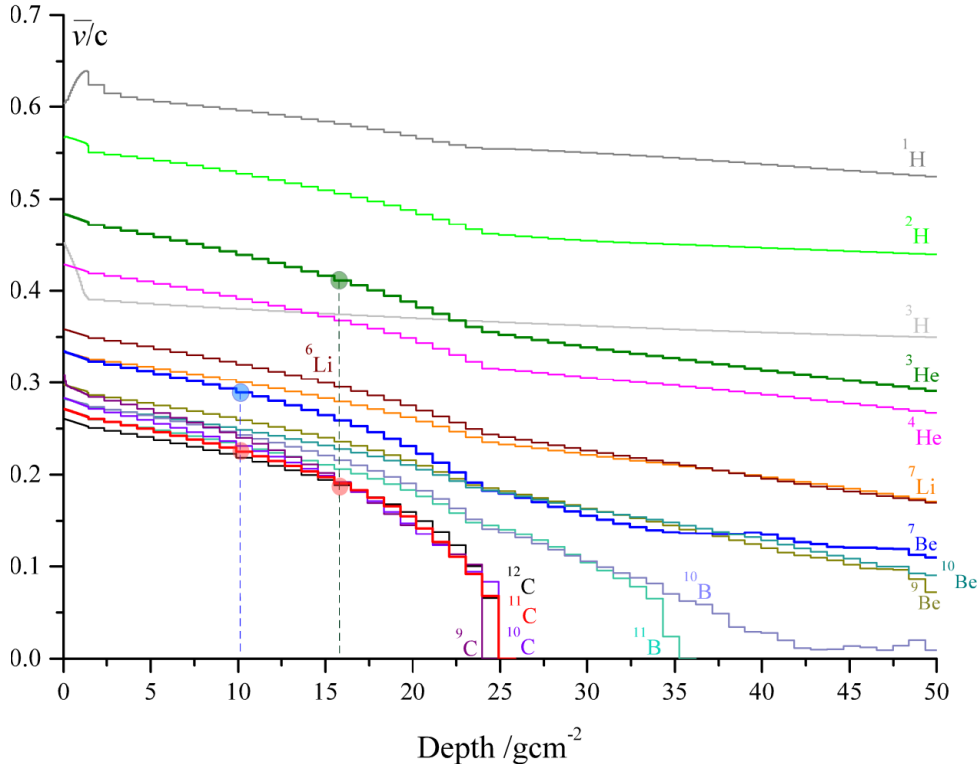


Figure 16 Variation of the particle velocity ( $\bar{v}/c$ ) as a function of the depth in a target made of 20 cm of liquid hydrogen followed by polyethylene. No intersection is seen among the  $^{11}\text{C}$ ,  $^3\text{He}$  and  $^7\text{Be}$  mean ion velocities at any depth in the target making TOF velocity filtering suitable. Small circles indicate the mean velocity values for the  $^{11}\text{C}$ ,  $^7\text{Be}$  and  $^3\text{He}$  fragments at the depths of the intersections in magnetic rigidity (Figure 13).

Figure 17 (a) and (b) show the fluence differential in velocity of the fragments at  $11 \text{ g/cm}^2$  and  $16 \text{ g/cm}^2$  of depth, respectively. Even considering the particle velocity spectra, no intersection is seen between the  $^{11}\text{C}$ - $^3\text{He}$  and  $^{11}\text{C}$ - $^7\text{Be}$  curves. Therefore, particles whose magnetic rigidity spectra intersect the  $^{11}\text{C}$  ion spectrum do not intersect in the velocity domain.

The TOF-velocity filter proposed in this work makes use of particle TOF properties in a two ways. The TOF-velocity filter is intended to be driven by the Radio Frequency (RF) of the cyclotron. Being fragments produced by direct in-flight reaction, they conserve, to a large extent, the micro pulse structure from the cyclotron. Thus, the optimal location of the filter can be calculated so that the  $^{11}\text{C}$  ions will move through the filter essentially unperturbed, whereas the contaminants (e.g.  $^7\text{Be}$  ions) will reach the filter at the opposite phase of the RF at

a time when the electric field has changed its direction. Thus, both the magnetic and electric components of the Lorentz's force will be oriented in the same direction and the sum of their contributions will enhance the contaminants' ejection strength.

Being the velocity filter tuned on the velocity of  $^{11}\text{C}$  particles, the following relation between the electric and magnetic field holds:  $B = E/\overline{v_{^{11}\text{C}}}$ , where  $\overline{v_{^{11}\text{C}}}$  is the mean velocity of  $^{11}\text{C}$  fragments at the entrance of the filter. Thus, in the conventional case of no variation of the electrostatic field with the cyclotron RF, the  $^7\text{Be}$  fragments are subject to the electromagnetic force:

$$|\overline{F_{^7\text{Be}}}| = q_{^7\text{Be}} \left( E - \overline{v_{^7\text{Be}}} B \right) = q_{^7\text{Be}} E \left( \frac{\overline{v_{^{11}\text{C}}} - \overline{v_{^7\text{Be}}}}{\overline{v_{^{11}\text{C}}}} \right). \quad (18)$$

Assuming a velocity filter of length  $L$  and electrostatic field magnitude  $E=U/d$ , where  $U$  is the electrostatic potential and  $d$  is the interplate distance, the deflection angle of the  $^7\text{Be}$  fragments at the exit of the velocity filter,  $\theta_{^7\text{Be}}$ , results in the following:

$$\theta_{^7\text{Be}} = \frac{dy}{L} = \left( \frac{F_{^7\text{Be}}}{M_{^7\text{Be}}} \right) \frac{t^2}{2L} = \left( \frac{F_{^7\text{Be}}}{M_{^7\text{Be}}} \right) \left( \frac{L}{2v_{^7\text{Be}}^{-2}} \right) = q_{^7\text{Be}} E \left( \frac{\overline{v_{^{11}\text{C}}} - \overline{v_{^7\text{Be}}}}{\overline{v_{^{11}\text{C}}}} \right) \left( \frac{L}{2v_{^7\text{Be}}^{-2} M_{^7\text{Be}}} \right). \quad (19)$$

In the case of RF-driven electrostatic field, the electrostatic and magnetic fields have the same direction and an additive contribution should be considered in equations (18) and (19).

Figure 18 (a) shows the deviation of the  $^7\text{Be}$  ion mean velocity with respect to the  $^{11}\text{C}$  ion mean velocity  $[(\overline{v_{^{11}\text{C}}} - \overline{v_{^7\text{Be}}})/\overline{v_{^{11}\text{C}}}]$  as a function of the depth in the decelerator.

As seen, the difference between the mean energy of the  $^{11}\text{C}$  and  $^7\text{Be}$  ions remains almost constant for the whole target length up to about 20 g/cm<sup>2</sup>. In the same figure, results of the angular deflection of  $^7\text{Be}$  fragments and correspondent spatial deflection are shown as a function of the depth for an electrostatic potential of 250 kV, a length of 5 m and a interplate distance of 1 m, which are the values characteristic of the Wien filter at the GANIL spectrometer (Anne and Mueller, 1992).

To increase the separation efficiency of the velocity filter and reduce its size, it might be possible, for example, to increase the interplate electrostatic potential and increase the strength of the magnetic field, which would help to prevent sparking. Another possibility would be modify the beam line design presented in Figure 12 and move the velocity filtering section in separate area.

Figure 18 (b) shows the velocity spectra of the  $^{11}\text{C}$  and  $^7\text{Be}$  ions at the exit of the wedge-shaped degrader for a target thickness combination corresponding to 11 g/cm<sup>2</sup>.

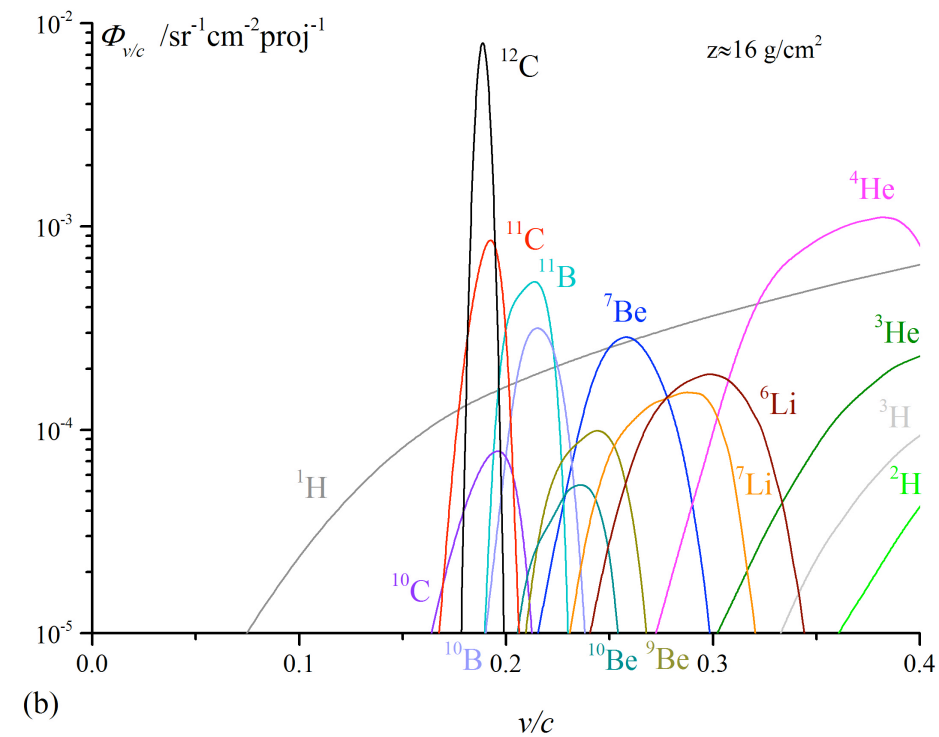
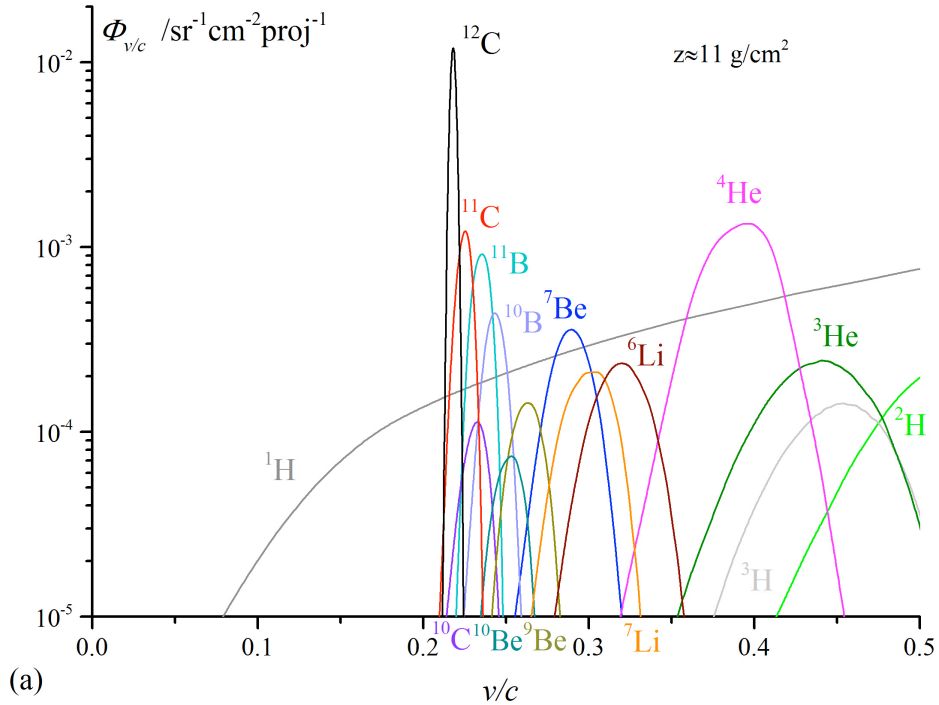


Figure 17 Velocity spectra of the fragments at  $11 \text{ g/cm}^2$  (a) and  $16 \text{ g/cm}^2$  (b) in a composite decelerator consisting of 20 cm of liquid hydrogen followed by polyethylene.

As expected, the velocity spectrum of the  $^{11}\text{C}$  ion beam at the exit of the wedge has a spread less than 1% (Figure 18 (b)) and therefore the loss of  $^{11}\text{C}$  ion intensity due to the deflection of the beam trajectory by the velocity filter, which is tuned on the  $^{11}\text{C}$  ion mean energy at the exit of the wedge-shaped profile, is consequently minimal. However, it is desirable to locate the wedge-shaped filter as close as possible in the beam line to the exit of the decelerator in order to improve the efficiency of the TOF velocity filter.

It may be mentioned that calculation of the deviation of the particle trajectories under the influence of the velocity filter were performed for the mean energy of the distributions. However, due to the location of the velocity filter in the beam line (after the wedge-shaped monochromatizing filter), the mean values of the distribution at the exit of the wedge are located around the minimum of the initial distributions.

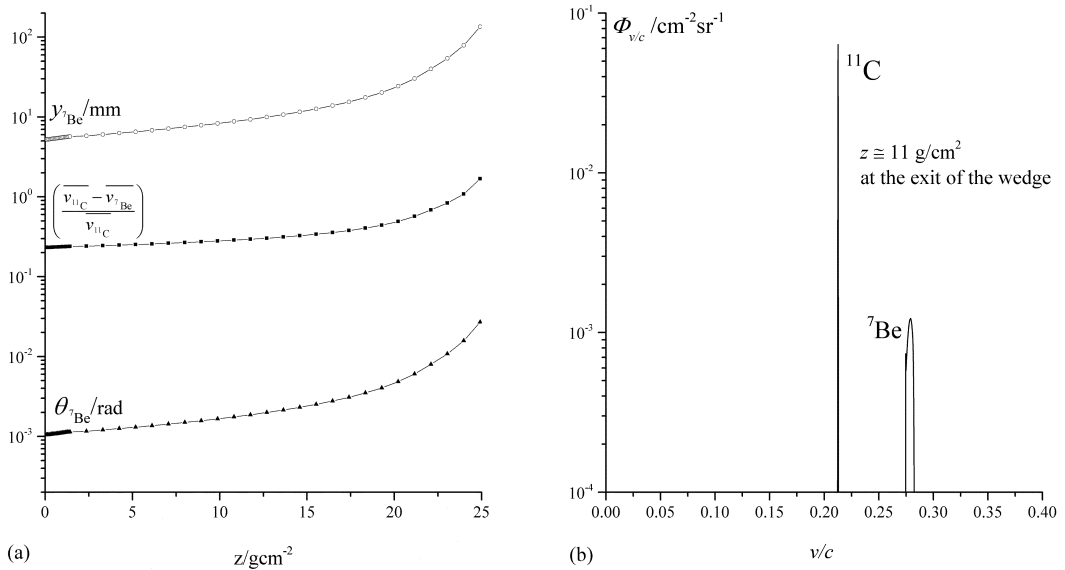


Figure 18 (a) Tranversal shift  $y_{7\text{Be}}$  with respect to the beam line optics axis of the  $^7\text{Be}$  ions due to the velocity filter action (in mm), deviation of the  $^7\text{Be}$  ion mean velocity with respect to the  $^{11}\text{C}$  ion mean velocity  $\left[ \left( \overline{v_{11\text{C}}} - \overline{v_{7\text{Be}}} \right) / \overline{v_{11\text{C}}} \right]$  and angular deviation of the  $^7\text{Be}$  fragments  $\theta_{7\text{Be}}$  as a function of the depth in the target (in rad), respectively. Calculations are performed by using equations (18) and (19) with the electrostatic potential of 250 kV, a length of 5 m and a plate distance of 1 m, as reported for the Wien filter at the GANIL spectrometer (Anne and Mueller, 1992). The velocity spectra of  $^{11}\text{C}$  ions and  $^7\text{Be}$  fragments at the exit of the wedge-shaped degrader are shown in (b).

## 4 THE MONTE CARLO CODE SHIELD-HIT

The Monte Carlo code SHIELD-HIT<sup>15</sup> has been used extensively throughout this study. The code allows to simulate the interaction and the transport of hadrons and nuclei of arbitrary mass and charge in macroscopic targets in the energy range up to 2 GeV/u. The geometry of the target is defined with the so called *combinatorial geometry* and arbitrary chemical and isotopic composition of materials in target zones is allowed.

SHIELD-HIT allows to implement Stopping Power Tables from the ICRU reports of proton and alpha particles (ICRU, 1993), and of heavier atoms (ICRU, 2005) having an energy cut-off of 25 keV/u. Alternatively, a modified version of the Bethe-Block equation (Bethe *et al.*, 1938) in combination with Lindhard-Scharff model (Lindhard and Scharff, 1961) allow to extend the energy range down to 10 keV/u. The modified Bethe-Block equation does not take into account the shell corrections, but it accounts for the interaction with target atoms in the low energy region resulting in the electron capture and loss by the projectile (Geithner *et al.*, 2006) through the *effective charge* (Hubert *et al.*, 1989). The crossing point between the Bethe-Block and the Lindhard-Scharff functions is calculated as the point where both the functions and their derivatives are equal (Geithner *et al.*, 2006). The transport of neutrons from 14.5 MeV down to thermal energies is based on the 28-group neutron data ABBN (Abagyan *et al.*, 1981) and handled by the Low Energy Neutron Transport (LOENT) code (Latysheva and Sobolevsky, 2008). The energy loss of particles can be simulated either by the Gaussian or Vavilov (Vavilov, 1957) models, while the multiple scattering can be described by Gaussian or Molière models (Bethe, 1953). The choice of the model is left to the user.

In the thesis two versions of the Monte Carlo code were used: SHIELD-HIT07 and SHIELD-HIT10<sup>16</sup>. In papers I and III the version 07 was utilized, whereas in paper II and IV the more recent version SHIELD-HIT10 was used.

The main difference between the two versions is in the parameterization of the angular distribution of elastic nucleon-nucleon scattering in the intranuclear cascade. The parameterization in SHIELD-HIT07 was found to overestimate the scattering in the forward direction and underestimate the energy of the recoil nucleon (Sobolevsky, 2011). This modification has been reported not to affect significantly the results of SHIELD-HIT simulations (Sobolevsky, 2011).

Furthermore, the multiple scattering is described in SHIELD-HIT07 only in the Gaussian approximation. The Molière model was implemented in the more recent versions. The code was used to score the production of <sup>11</sup>C ions produced by the fragmentation of a primary <sup>12</sup>C ion beam to investigate the optimal choice of

---

<sup>15</sup> <http://www.inr.ru/shield/>

<sup>16</sup> In the papers, SHIELD-HIT+ and SHIELD-HIT10+ refer to the modified version of SHIELD-HIT07 and SHIELD-HIT10, respectively. In the modified versions, the possibility of scoring the double differential fluence in energy and angle was implemented (Kempe and Brahme, 2010a; Hultqvist *et al.*, 2012).

target material for maximizing the production of positron emitter isotopes that could be used for treatment and monitoring the dose delivery distribution. The investigation is conducted by scoring particle fluence and fluence double differential in energy and angle.

#### 4.1 NUCLEAR MODELS AND FERMI BREAK-UP

Total and inelastic cross sections for hadron-nucleus and nucleus-nucleus interactions are calculated in SHIELD-HIT with the Baranshekov-Polansky parameterization (Barashenkov and Polanski, 1994), included in the code CROSEC integrated in SHIELD-HIT. SHIELD-HIT uses fits based on the quasi-optical model of nuclear cross sections (above about 200MeV) and semi-empirical formulas at lower energies. Specifically, for the hadron-nucleus cross sections, the code uses a database of tables, which includes 18 reference materials<sup>17</sup> and for the missing nuclei an interpolation with  $A^{2/3}$  is performed.

To separate the channels of nuclear reactions the Many Stage Dynamical Model generator is used, which was developed in a collaboration between the Institute for Nuclear Research of the Russian Academy of Science (INR RAS, Moscow) and the Joint Institute for Nuclear Research (JINR, Dubna) (Botvina *et al.*, 1987; Botvina *et al.*, 1990; Botvina *et al.*, 1997). The MSDM generator is also Monte Carlo based itself, it forces the inelastic interactions between the incoming ion and the target nuclei to occur, and it describes all the different steps of the nuclear reaction in an exclusive approach. The outgoing number of generated fragments is scored by the MSDM code, differential in energy and angle. For example, to calculate single channel inelastic cross section, the fraction of resulting fragment  $N_i/N_0$  (where  $N_0$  is the number of simulated primaries) should be then multiplied by the total inelastic cross section calculated with the Baranshekov-Polansky parameterization.

The MSDM model follows subsequent stages of the inelastic nuclear interaction process, which are: fast cascade, coalescence, pre-equilibrium decay of residual nuclei and finally equilibrated de-excitation of the residual nucleus.

In the fast cascade stage, the nuclear interactions are considered as a series of two-body collisions between the nuclear constituents and/or produced hadrons. The direct knock-out of nucleons is possible at this stage. For energies below 1 GeV the Dubna Cascade model is used (Toneev and Gudima, 1983), while for higher energies an extension of the Quark-Gluon String Model is used (Amelin *et al.*, 1990a; Amelin *et al.*, 1990b). In the coalescence stage, more complex particles (such as  $^2\text{H}$ ,  $^3\text{H}$ ,  $^3\text{He}$ ,  $^4\text{He}$  nuclei) may be formed through the coalescence of nucleons that are close in the momentum space after the fast cascade phase.

Since the residual nucleus at the end of the cascade is not in the equilibrium state, its evolution toward the equilibrium is described through the pre-equilibrium model developed by (Gudima *et al.*, 1975).

---

<sup>17</sup> ( $^1\text{H}$ ,  $^2\text{H}$ ,  $^4\text{He}$ ,  $^9\text{Be}$ ,  $^{14}\text{N}$ ,  $^{16}\text{O}$ ,  $^{22}\text{Na}$ ,  $^{26}\text{Al}$ ,  $^{28}\text{Si}$ ,  $^{40}\text{Ca}$ ,  $^{56}\text{Fe}$ ,  $^{64}\text{Cu}$ ,  $^{96}\text{Mo}$ ,  $^{112}\text{Cd}$ ,  $^{119}\text{Sn}$ ,  $^{184}\text{W}$ ,  $^{207}\text{Pb}$ ,  $^{238}\text{U}$ ).

The final step of de-excitation is described by different models. For light nuclei having  $A \leq 16$ , a modified version of the Fermi break-up model is used (Botvina *et al.*, 1987), whereas for medium and heavy nuclei different models are used according to their excitation energy. When  $E^* < 2$  MeV/u, the de-excitation is described by an evaporation process including, for heavy nuclei, fission competition (Botvina *et al.*, 1987; Bondorf *et al.*, 1995). If the excited nuclei have  $E^* > 2$  MeV/u, they can decay in several excited fragments and a statistical model of multifragmentation is used to describe the process (Botvina *et al.*, 1990).

In paper I, the total inelastic cross sections for carbon ions in H and C target were compared with experimental data and calculation published by (Böhlen *et al.*, 2010) with the FLUKA (Ferrari *et al.*, 2005; Battistoni *et al.*, 2007) and GEANT4 (Agostinelli *et al.*, 2003; Allison *et al.*, 2006) Monte Carlo codes. In paper II, the capability of the SHIELD-HIT code to simulate the nuclear fragmentation of carbon ions in tissue-like materials was more extensively tested on the level of total and partial charge-changing cross sections as well as for fragment yields in intermediate and thick water targets. Comparisons made with available experimental results evidenced a general overestimation of the production of Li and Be fragments, while the production of He fragments was underestimated.

A modification of the value of the parameter  $k$ , which determines the so called *freeze-out* volume in the modified Fermi break-up model, was introduced to achieve a better agreement with the experimental results available in the literature. In the modified Fermi break-up model, it is assumed that the excited nucleus decays into several small clusters. The nuclear system expands and fragments are formed during this expansion. The expansion stops and the fragments are considered as completely formed when the freeze-out volume is reached. Fragments are then considered to be free. The freeze-out volume  $V$  is parameterized as  $V = V_0(1+k)$ , where  $V_0$  is the volume of the nucleus in the non-excited state. The parameter  $k$  is of the order of one to tens and should be adjusted by comparison with experimental data. Values from 1 to 30 were tested and the value  $k=10$  was chosen as a reasonable compromise,  $k=1$  being default in SHIELD-HIT. An increase in the value of  $k$  results in an increased multiplicity of the fragments and a decrease of their masses, as shown by (Botvina *et al.*, 1987). This motivated the choice of the increase in the value of  $k$ . More details on the Fermi break-up model are given in section 2.3 of paper II and references therein. Even though a better agreement with experimental data was achieved by this modification in the nuclear models, it should be underlined that more comparisons with experimental data, particularly for particles other than carbon, would be highly beneficial.

## 4.2 UNCERTAINTIES IN THE PRODUCTION YIELDS OF THE FRAGMENTS DUE TO NUCLEAR MODELS IN SHIELD-HIT

In Figure 19, the fluence build-up of fragments generated in a pure liquid hydrogen target and in a PMMA target are shown for default value of the parameter  $k=1$  and for the modified value  $k=10$  in the Fermi break-up model. As

expected, the yield of light fragments is reduced by modifying the parameter, whereas the yield of heavier fragments is increased. Specifically, the  $^{11}\text{C}$  ion fluence build-up is negligibly affected by the change in  $k$  (difference are about 1-2%), since the knock-out of one neutron from the primary  $^{12}\text{C}$  ion beam takes place mainly in the cascade stage.

The yield of the  $^3\text{He}$  and  $^7\text{Be}$  fragments, which were found to be the most contaminating in the produced  $^{11}\text{C}$  ion beam, diminishes as value of  $k$  increases. Therefore, since default values of the parameter  $k$  were used in paper IV, a lower level of contamination may be expected if an increase value of  $k$  is used.

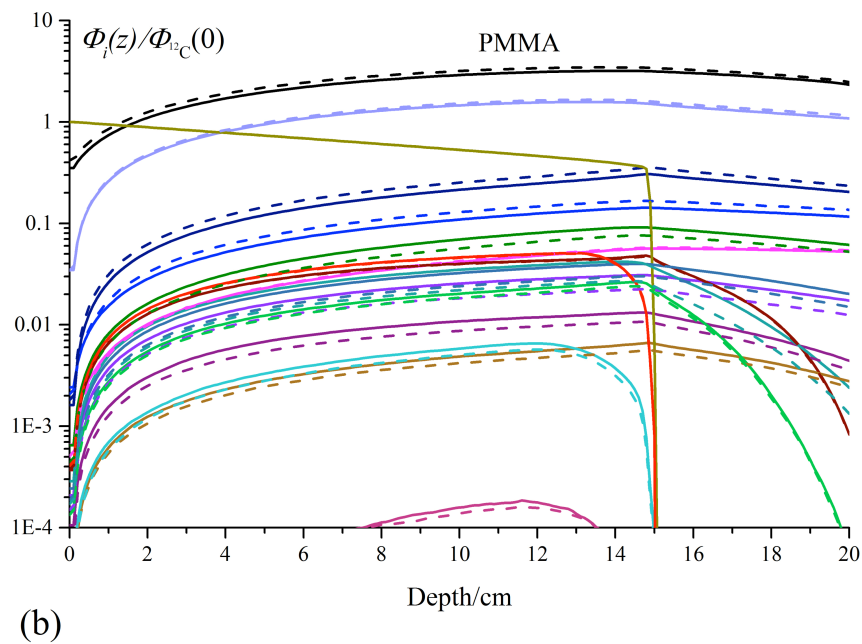
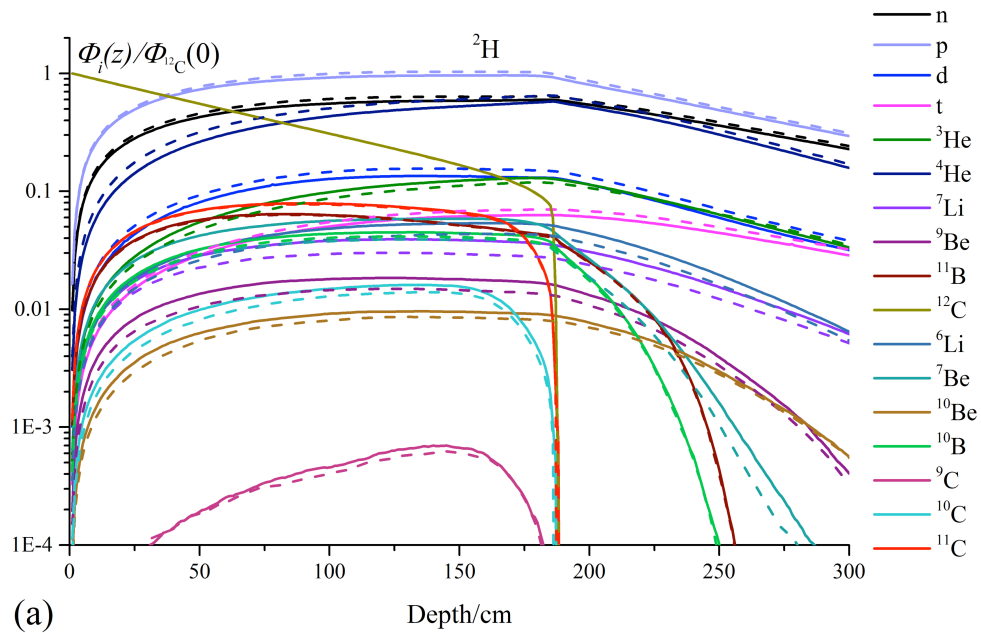


Figure 19 Fluence build-up of fragments in a pure liquid hydrogen target (a) and a PMMA target (b) for both the default value of the parameter  $k$  ( $k=1$ , solid lines) and the modified value of  $k$  ( $k=10$ , dashed lines) in the Fermi break-up model.

## 5 DISCUSSION AND CONCLUSIONS

An accurate verification of the delivery of the treatment is one of the key issues not least in modern adaptive and biologically optimized radiation therapy with external beams. The importance is particularly high when sub mm accuracy light ions beams are used. In order to fully exploit their potential for delivering a highly conformal biologically optimized dose to the target volume, the accurate control of the dose delivery is essential, since potential misalignments may entail severe overdosage to the normal tissues and/or underdosage to the target volume.

The uncertainties in the conversion of CT measured-HUs into stopping power values of ions in the tissue during treatment planning are still a matter of concern, which unavoidably requires the additional support of the clinical treatment verification.

PET imaging is at present the only clinically implemented imaging technique which allow accurate verification of treatment delivery for ion therapy (Parodi, 2012; Strååt *et al.*, 2013b). The verification of the treatment in clinical routine was so far limited to beam setup, possible error in the calibration of CT-HUs into stopping power data and range verification (Parodi, 2012). Even though the theoretical framework for the exploitation of dose delivery verification is already available, practical and technological issues mainly related to the low activity signal registered and biological clearance of the activity may influence its applicability in some tissues. Different technologies and methods are under development. For instance, new possibilities of particle detection have been explored, such as Time of Flight PET, prompt gamma or charged particle imaging,  $\gamma$ -PET etc. (Dauvergne *et al.*, 2009; Testa, 2011; Lang *et al.*, 2013).

The use of positron emitter beams for treatment is probably the optimal solution to increase the activity signal registered by PET imaging at least one order of magnitude (Tomitani *et al.*, 2003; Brahme, 2009). Another order of magnitude increase in the  $\beta^+$ -activity signal may be achieved by using In-beam PET with  $^{10}\text{C}$  ions as compared to an irradiation with  $^{11}\text{C}$  ions, as seen in Table 1. One of the main limiting factors for the use of radioactive beams for treatment is related to the difficulties associated with their production and purification.

This thesis is focused on the in-flight fragmentation method for the production of  $^{11}\text{C}$  positron emitter beams from a primary  $^{12}\text{C}$  ion beam with the aim of maximizing the production efficiency. The main steps from the production of the beam (papers I and III) to the purification from other contaminating fragments (paper IV) were described. A  $^{11}\text{C}$  ion beam with an intensity equal to about 5% of the primary  $^{12}\text{C}$  ion intensity with a radial spread less than 1 cm in diameter, energy and angular spread equal to about 1% and 1°, respectively, and an expected contamination from other fragments of about 1% may be achievable.

Specifically, the novel technique proposed makes use of a combined production target made of 20 cm of liquid hydrogen to maximize the  $^{11}\text{C}$  ion beam production (papers I and III) and a decelerator system consisting of plane parallel slabs, whose thicknesses may be combined to reduce the ion beam energy to the value needed for reaching different tumor depths. The present optimal selection of the

production target is the result of a comprehensive characterization of the secondary  $^{11}\text{C}$  ion beam in terms of energy, angular, radial spread in different materials and in a composite target with a variable liquid hydrogen section (paper III). The study was not only limited to the  $^{11}\text{C}$  ion beam, but it also included other possible contaminating fragments produced in the target. Production yields, mean energy, mean magnetic rigidity, mean velocity of the ions as a function of the depth in the target were presented in paper IV. Furthermore, detailed spectra analysis in the energy, magnetic rigidity and velocity domain for selected depths of interest were also shown (paper IV).

A beam line design, including a variable wedge-shaped degrader able to almost eliminate the energy spread of the  $^{11}\text{C}$  particles and a TOF Radio Frequency driven velocity filter to separate the  $^{11}\text{C}$  ions from undesired fragments, was developed.

The analysis presented in paper I, III and IV were conducted with the Monte Carlo code SHIELD-HIT. Analytical models of transport of ions in matter have been used throughout the work and guided, supported and helped interpreting the Monte Carlo results.

Paper II was focused on testing and further benchmarking of SHIELD-HIT with experimental data available for carbon ion beam irradiation in different targets of interest in the medical field.

The natural continuation of this work would, primarily, consist in the full simulation of the whole  $^{11}\text{C}$  beam line optics and in the related radiation protection studies, particularly addressed to accurately calculate the required neutron shielding in the treatment room. The possible extension of the results to the production of other positron emitter beams with shorter half-life and lower mass, e.g.  $^8\text{B}$  ions, would be highly desirable, particularly in view of their increased clinical value, due to of their lower LET in the entrance channel and fragmentation tail region compared to carbon ions, and potential for *real time* imaging, due to their fast decay ( $\sim 0.7$  s).

Further benchmark of the Monte Carlo code SHIELD-HIT both on the level of cross sections and thick target yields would be highly beneficial for ions other than carbon. In particular, comparisons with experimental data apt to test the nuclear models responsible for the production of different isotopes of the same ion would be of particular importance in the medical field.

In conclusion, the work presented in this thesis contributes to the developments of accurate treatment verification which is one of the key steps towards comprehensive biologically optimized adaptive treatments, as illustrated in Figure 3.

## **6 ACKNOWLEDGEMENTS**

I wish to express my gratitude to all the people who helped me to complete this thesis.

First and foremost, I would like to thank my supervisor and co-author Prof. Anders Brahme for giving me the opportunity of starting this Ph.D. project. Thank you for your guidance, support, for the constant encouragement throughout this challenging journey. Thank you for generously sharing with me your knowledge, your endless stream of ideas and your enthusiasm for light ion therapy. Thank you for always being available despite the long distance and for our long phone calls in the last months at any time, any day of the week.

I would like to express my deep and sincere gratitude to my co-supervisor Assoc. Prof. Iuliana Toma-Dasu. Thank you for your care and for always being supportive whenever I needed help from the very first day I arrived at MSF. Thank you for your insightful comments and suggestions on my manuscripts and thesis.

Dr. Johanna Kempe, co-supervisor of my Ph.D. project, I really appreciate the friendly way I could discuss with you about analytical models of ion transport in matter. Thank you.

I would like to thank Prof. Nikolai Sobolevsky, who I never had the opportunity to meet in person, but to whom I am really indebted. Thank you for answering all my questions about SHIELD-HIT from the beginning of my Ph.D. to the very last days.

Prof. Hooshang Nikjoo, thank you for giving me the opportunity of attending the meetings of the Radiation Biophysics Group. Thank you for the time you dedicate to the scientific growth of the Ph.D. students at MSF.

I wish to thank my co-authors who have not already been mentioned: Assoc. Prof. Irena Gudowska, thank you for the time you dedicated to me; Dr. Martha Hultqvist, thank for making the Monte Carlo data analysis a pleasant time; Prof. Alexander Botvina, thank you for the fruitful collaboration.

Assoc. Prof. Bo Nilsson, thank you for letting me share the office with you and for making me feel welcome at MSF. As a student, I could really feel your passion and dedication for teaching.

Prof. Dževad Belkić, I gratefully acknowledge the time you dedicated to proof-reading my work.

Prof. Manjit Dosanjh, I feel privileged to have had the opportunity of being part of the PARTNER project. Thank you for your hard work in building such a friendly scientific network.

I wish to thank all the other Supervisors at the Medical Radiation Physics division, who have not already been mentioned. I learned something from each and every one of you: Assoc. Prof. Margareta Edgren, Assoc. Prof. Bengt Lindt, Prof. Pedro Andreo, Prof. Karen Belkić, Assoc. Prof. Albert Siegbahn, Prof. Lennart Lindberg, Dr. Annelie Meijer.

Lil Engström, thank you for your care and smile, and for making me feel welcome from the very first day. Marianne Eklund, thank you for your kind help with the administrative work.

My former and current colleagues: Thiansin Liamsuwan, Reza Taleei, Chitralekha Mohanty, Martha Hultqvist, Kristin Wiklund, Johanna Kempe, Björn Andreassen, Katarzyna Zielinska-Chomej, Patrick Vreede, Eleftheria Alevronta, Johan Staaf, Laura Antonovic, Minna Wedenberg, Sara Strååt, Till Tobias Böhlen, Lucilio Matias, Tommy Sundström, Helena Sandström, Emely Lindblom, Hamza Benmakhlof, Bahram Andisheh, Shirin Rahmanian, Nicoletta Protti, Alfredo Metere.

All my PARTNER-friends. I hope we will have the chance to meet again somewhere in the globe!

Last but not least, I would like to thank my family for giving me the courage and strength to find my way.

Mirko, thank you for walking by my side.

This research project was supported by a Marie Curie Initial Training Network Fellowship of the European Community's Seventh Framework Programme under contract number (FP7/2007-2013) under grant agreement n° 215840-2.

## 7 REFERENCES

- Abagyan L P, Bazazyants N O, Nikolaev M N and Tsibulya A M 1981 *Neutron Group Constants for Reactors and Shielding Calculations* (Moscow: Atomizdat) 1-231
- Agostinelli S, et al. 2003 G4 - a simulation toolkit *Nucl. Instr. Meth. Phys. Res. A* **506** 250-303
- Allison J, et al. 2006 GEANT 4 developments and applications *IEEE Trans. on Nucl. Sci.* **53** 270-8
- Alonso J R and Castro J R 2002 Light-ion therapy in the U.S.: From the Bevalac to ?? *Lawrence Berkeley National Laboratory* (<http://www.escholarship.org/uc/item/1gj8j45t>)
- Alonso J R, Chatterjee A and Tobias C A 1979 High purity radioactive beams at BEVALAC *IEEE Trans. on Nucl. Sci.* **NS-26** 3003-5
- Alonso J R and Krebs G 1984 Relativistic radioactive heavy ion beams at Bevalac *LBL-17829; CONF-8404154-2*
- Amelin N S, Gudima K K, Siviklokov S Y and Toneev V D 1990a Further development of the quark-gluon string model for describing high-energy collisions with nuclear target *Yad. Fiz.* **52** 272-82
- Amelin N S, Gudima K K and Toneev V D 1990b Ultrarelativistic nucleus-nucleus collisions within a dynamical model of independent quark-gluon strings *Yad. Fiz.* **51** 1730-43
- Anferov V 2003 Energy degrader optimization for medical beam lines *Nucl. Instr. Meth. Phys. Res. A* **496** 222-7
- Anne R and Mueller A C 1992 LISE 3: a magnetic spectrometer-Wien filter combination for secondary radioactive beam production *Nucl. Instr. Meth. Phys. Res. B* **70** 276-85
- Antonovic L, Brahme A, Furusawa Y and Toma-Dasu I 2013 Radiobiological description of the LET dependence of the cell survival of oxic and anoxic cells irradiated by carbon ions *Journal of Radiation Research* **54** 18-26
- Attanasi F, et al. 2008 Experimental validation of the filtering approach for dose monitoring in proton therapy at low energy *Phys Med* **24** 102-6
- Attanasi F, et al. 2010 Characterization of an In-Beam PET Prototype for Proton Therapy With Different Target Compositions *Nuclear Science, IEEE Transactions on* **57** 1563-9
- Attanasi F, Knopf A, Parodi K, Paganetti H, Bortfeld T, Rosso V and Del Guerra A 2011 Extension and validation of an analytical model for in vivo PET verification of proton therapy-a phantom and clinical study *Phys. Med. Biol.* **56** 5079-98
- Bacquias A, Föhr V, Henzlova D, Kelic-Heil A, Ricciardi M V and Schmidt K H 2012 Dispersion of longitudinal momentum distributions induced in fragmentation reactions *Physical Review C* **85** 24904-12
- Barashenkov V S and Polanski A 1994 Electronic guide for nuclear cross-sections *Communication of JINR E2-94-417, Dubna*

- Barendsen G W, Koot C J, Van Kersen G R, Bewley D K, Field S B and Parnell C J 1966 The Effect of Oxygen on Impairment of the Proliferative Capacity of Human Cells in Culture by Ionizing Radiations of Different LET *Int. J. Radiat. Biol. Relat. Stud. Phys. Chem. Med.* **10** 317-27
- Battistoni G, Muraro S, Sala P, Cerutti F, Ferrari A, Roesler S, Fassò A and Ranft J 2007 The FLUKA code: description and benchmarking *Proc. Hadronic Shower Simulation Workshop (Fermilab, 6-8 September 2006) (AIP Conf. Proc.)* **896** 31-49
- Bethe H A 1953 Molière theory of multiple scattering *Phys. Rev.* **89** 1256-66
- Bethe H A, Rose M and Smith L P 1938 The multiple scattering of electrons *Proceedings of the American Philosophical Society* **78** 573-85
- Bimbot A 1988 Production of 400 MeV/u radioactive ion beams for therapy purposes *Proceedings of the EULIMA Workshop on the Potential Value of light ion therapy* 443-68
- Bimbot R 1995 Nuclear physics with radioactive beams *Appl. Radiat. Isot.* **46** 537-42
- Bimbot R, Della-Negra S, Aguer P and Bast G 1985 Production of secondary radioactive beams from 44 MeV/u Ar projectiles *Zeitschrift für Physik A Atoms and Nuclei* **322** 443
- Bimbot R, et al. 1986 Heavy ion secondary beams *Journal de Physique Colloque* **47** 241-3
- Blumenfeld Y 2008 Review of accelerators for radioactive beams *Proc. EPAC08, Genova (Italy)* 41-5
- Blumenfeld Y, Nilsson T and Van Duppen P 2013 Facilities and methods for radioactive ion beam production *Phys. Scr.* **T152** 014023
- Bom V, Joulaeizadeh L and Beekman F 2012 Real-time prompt gamma monitoring in spot-scanning proton therapy using imaging through a knife-edge-shaped slit *Phys. Med. Biol.* **57** 297-308
- Bondorf J P, Botvina A S, Iljinov A S, Mishustin I and Sneppen K 1995 Statistical multifragmentation of nuclei *Phys. Rep.* **257** 133-221
- Botvina A S, Dementyev A V, Smirnova O N, Sobolevsky N M and Toneev V D 1997 MSDM - Multi Stage Dynamical Model *International Codes and Model Intercomparison for Intermediate Energy Activation Yields. NSC/DOC(97)-1, NEA/P&T No 14 (Paris: OECD)* 307
- Botvina A S, Iljinov A S and Mishustin I N 1990 Multifragment break-up of nuclei by intermediate-energy protons *Nuclear Physics A* **507** 649-73
- Botvina A S, Iljinov A S, Mishustin I N, Bondorf J P, Donangelo R and Sneppen K 1987 Statistical simulation of the break-up of highly excited nuclei *Nuclear Physics A* **475** 663-86
- Bragg W 1905 On the  $\alpha$ -particles of radium and their loss of range in passing through various atoms and molecules *Philos. Mag.* **10** 318-40
- Brahme A 2003 Biologically Optimized 3-Dimensional In Vivo Predictive Assay-Based Radiation Therapy Using Positron Emission Tomography-Computerized Tomography Imaging *Acta Oncologica* **42** 123-36
- Brahme A 2004 Recent advances in light ion radiation therapy *International Journal of Radiation OncologyBiologyPhysics* **58** 603-16

- Brahme A 2009 Potential developments of light ion therapy: The ultimate conformal treatment modality *Radiological sciences* **52** 8-31 (<http://www.nirs.go.jp/info/report/rs-sci/pdf/200902.pdf>)
- Brahme A 2010 Optimal use of light ions for radiation therapy *Radiological sciences* **53** 35-61 (<http://www.nirs.go.jp/publication/rs-sci/pdf/201008.pdf>)
- Brahme A 2011 Accurate Description of the Cell Survival and Biological Effect at Low and High Doses and LET's *J. Radiat. Res.* **52** 389-407
- Brahme A 2012 *Technical Basis of Radiation Therapy: Practical Clinical Applications*, ed H Seymour, et al. (Springer) pp 218-51
- Böhlen T T, Cerutti F, Dosanjh M, Ferrari A, Gudowska I, Mairani A and Quesada J M 2010 Benchmarking nuclear models of FLUKA and GEANT4 for carbon ion therapy *Phys. Med. Biol.* **55** 5833-47
- Chapman J D, Blakely E A, Smith K C, Urtasun R C, Lyman J T and Tobias C A 1978 Radiation Biophysical Studies with Mammalian Cells and a Modulated Carbon Ion Beam *Radiation Research* **74** 101-11
- Chatterjee A, Alpen E, Tobias C A, Llacer J and Alonso J R 1981 High energy beams of radioactive nuclei and their biomedical applications *Int. J. Radiation Oncology Biol. Phys.* **7** 503-7
- Chatterjee A, Saunders W, Alpen E, Alonso J R, Scherer J and Llacer J 1982 Physical measurements with high-energy radioactive beams *Radiation Research* **92** 230-44
- Combs S E, et al. 2013 Towards clinical evidence in particle therapy: ENLIGHT, PARTNER, ULICE and beyond *J. Radiat. Res.* **54** i6-i12
- Crespo P 2005 Optimization of In-Beam Positron Emission Tomography for Monitoring Heavy Ion Tumor Therapy, PhD thesis, Von Fachbereich Physik, Technischen Universität Darmstadt
- Dauvergne D, Battaglia M, Montarou G and Testa E 2009 New methods of real-time control imaging for ion therapy. In: *NIRS-ETOILE symposium on carbon ion therapy*, pp 1-7
- Donets D E, et al. 2010 Electron string ion source applied for formation of primary radioactive carbon ion beams *Proceedings of IPAC'10, Kyoto, Japan*
- Dufour J P, Del Moral R, Emmermann H, Hubert F, Jean D, Poinot C, Pravikoff M S and Fleury A 1986 Projectile fragments isotopic separation: application to the LISE spectrometer at Ganil *Nucl. Instr. Meth. Phys. Res. A* **248** 267-81
- Enghardt W 2004 Charged hadron tumour therapy monitoring by means of PET *Nucl. Instr. Meth. Phys. Res. A* **525** 284-8
- Enghardt W, et al. 1999 Positron emission tomography for quality assurance of cancer therapy with light ion beams *Nuclear Physics A* **654** 1047c-50c
- Enghardt W, et al. 1991 In-beam PET imaging experiments at FRS *GSI Scientific Report*
- Enghardt W, Parodi K, Crespo P, Fiedler F, Pawelke J and Ponisch F 2004 Dose quantification from in-beam positron emission tomography *Radiotherapy and Oncology* **73** S96-S8

- EULIMA 1988 The potential value of light ion beam therapy. ed P Chauvel and A Wambersie (Nice,France) (<http://bookshop.europa.eu/en/proceedings-of-the-eulima-workshop-on-the-potential-value-of-light-ion-beam-therapy-pbEUNA12165/>)
- Ferrari A, Sala P, Fassò A and Ranft J 2005 FLUKA: a multi-particle transport code *CERN Yellow Report 2005-10, INFN/TC 05/11, SLAC-r-773*
- Fiedler F, Crespo P, Parodi K, Sellesk M and Enghardt W 2006 The feasibility of In-Beam PET for therapeutic beams of  $^3\text{He}$  *IEEE Transactions on nuclear science* **53** 2252-9
- Fiedler F, Kunath D, Priegnitz M and Enghardt W 2011 *Ion beam therapy. Fundamentals, technology, clinical applications*, ed U Linz (Springer) pp 527-43
- Fiedler F, Priegnitz M, Jülich R, Pawelke J, Crespo P, Parodi K, Pönisch F and Enghardt W 2008 In-beam PET measurements of biological half-lives of  $^{12}\text{C}$  irradiation induced  $\beta^+$ -activity *Acta Oncologica* **47** 1077-86
- Furusawa Y, Fukutsu K, Aoki M, Itsukaichi H, Eguchi-Kasai K, Ohara H, Yatagai F, Kanai T and Ando K 2000 Inactivation of Aerobic and Hypoxic Cells from Three Different Cell Lines by Accelerated  $^3\text{He}$ -,  $^{12}\text{C}$ - and  $^{20}\text{Ne}$ -Ion Beams *Radiation Research* **154** 485-96
- Geissel H, et al. 1992 The GSI projectile fragment separator (FRS): a versatile magnetic system for relativistic heavy ions *Nucl. Instr. Meth. Phys. Res. B* **70** 286-97
- Geissel H, Schwab T, Armbruster P, Dufour J P, Hanelt E, Schmidt K-H, Sherrill B and Munzenberg G 1989 Ions penetrating through ion-optical systems and matter- Non-Liouvillian phase-space modelling *Nucl. Instr. Meth. Phys. Res. A* **282** 247-60
- Geissel H, Weick H, Scheidenberger C, Bimbot R and Gardes D 2002 Experimental studies of heavy-ion slowing down in matter *Nucl. Instr. Meth. Phys. Res. B* **195** 3-54
- Geithner O, Andreo P, Sobolevsky N, Hartmann G and Jäkel O 2006 Calculation of stopping power ratios for carbon ion dosimetry *Phys. Med. Biol.* **51** 2279-92
- Goldhaber A S 1974 Statistical Models of fragmentation processes *Physics Letters B* **53** 306-8
- Goldhaber A S and Heckman H H 1978 High energy interactions of nuclei *Ann. Rev. Nucl. Part. Sci.* **28** 161-205
- Greiner D E, Lindstrom P J, Heckman H H, Cork B and Bieser F S 1975 Momentum distributions of isotopes produced by fragmentation of relativistic  $^{12}\text{C}$  and  $^{16}\text{O}$  projectiles *Physical Review Letters* **35** 152-5
- Gudima K K, Ososkov G A and Toneev V D 1975 Model for Pre-Equilibrium Decay of Excited Nuclei *Sov. J. Nucl. Phys.* **21** 260
- Hadamard J 1902 Sur les problèmes aux dérivées partielles et leur signification physique *Bull. Univ. Princeton* 49-52
- Haettner E 2006 Experimental study on carbon ion fragmentation in water using GSI therapy beams Master's Thesis, Kungliga Tekniska Hogskolan Stockholm (Sweden)

- Hall E J and Giaccia A J 2006 *Radiobiology for the Radiologist* (Lippincott Williams & Wilkins)
- Helmbrecht S, Santiago A, Enghardt W, Kuess P and Fiedler F 2012 On the feasibility of automatic detection of range deviations from in-beam PET data *Phys. Med. Biol.* **57** 1387-97
- Henriquet P, et al. 2012 Interaction vertex imaging (IVI) for carbon ion therapy monitoring: a feasibility study *Phys. Med. Biol.* **57** 4655-69
- Hirayama R, et al. 2009 Contributions of direct and indirect actions in cell killing by high-LET radiations *Radiation Research* **171** 212-8
- Hojo S, Honma T, Muramatsu M, Sakamoto Y and Sugiura A 2008 Development of gas pulsing system for electron cyclotron resonance ion source *Review of Scientific Instruments* **79** 02A306
- <http://clinicaltrials.gov/>
- <http://enlight.web.cern.ch/>
- <http://ptcog.web.psi.ch/ptcentres.html>
- <http://www.cancerartforce.eu/>
- <http://www.inr.ru/shield/>
- <http://www.klinikum.uni-heidelberg.de>
- <http://www.srim.org/>
- Hubert F, Bimbot R and Gauvin H 1989 Semi-empirical formulae for heavy ion stopping powers in solids in the intermediate energy range *Nucl. Instr. Meth. Phys. Res. B* **36** 357
- Hultqvist M, Lazzeroni M, Botvina A S, Gudowska I, Sobolevsky N and Brahme A 2012 Evaluation of nuclear reaction cross sections and fragment yields in carbon beams using the SHIELD-HIT Monte Carlo code. Comparison with experiments. *Phys. Med. Biol.* **57** 4369-85
- IAEA-TECDOC-1560 2007 Dose Reporting in Ion Beam Therapy *Proceedings of a meeting organized jointly by the International Atomic Energy Agency and the International Commission on Radiation Units and Measurements, Ohio (USA), 18–20 March 2006*
- ICRU 1984 Radiation Dosimetry: Electron Beams with Energies Between 1 and 50 MeV *International Commission on Radiation Units and Measurements Report 35* (Bethesda, Maryland, USA)
- ICRU 1992 Photon, Electron, Proton and Neutron Interaction Data for Body Tissues *International Commission on Radiation Units and Measurements Report 46* (Bethesda, Maryland, USA)
- ICRU 1993 Stopping Powers and Ranges for Protons and Alpha Particles *International Commission on Radiation Units and Measurements Report 49* (Bethesda, Maryland, USA)
- ICRU 1998 Fundamental Quantities and Units for Ionizing Radiation *International Commission on Radiation Units and Measurements Report 60* (Bethesda, Maryland, USA)
- ICRU 2005 Stopping of Ions Heavier Than Helium *International Commission on Radiation Units and Measurements Report 73* (Bethesda, Maryland, USA)
- Iseki Y, Kanai T, Kanazawa M, Kitagawa A, Mizuno H, Tomitani T, Suda M and Urakabe E 2004 Range verification system using positron emitting beams for heavy-ion radiotherapy *Phys. Med. Biol.* **49** 3179-95

- Ito A, Nakano H, Kusano Y, Hirayama R, Furusawa Y, Murayama C, Mori T, Katsumura Y and Shinohara K 2006 Contribution of indirect action to radiation-induced mammalian cell inactivation: dependence on photon energy and heavy-ion LET *Radiation Research* **165** 703-12
- Janek S, Svensson R, Jonsson C and Brahme A 2006 Development of dose delivery verification by PET imaging of photonuclear reactions following high energy photon therapy *Phys. Med. Biol.* **51** 5769-83
- Jäkel O 2011 *Ion Beam Therapy. Fundamentals, Technology, Clinical Applications*, ed U Linz (Springer) pp 489-502
- Kanazawa M, et al. 2002 Application of an RI-beam for cancer therapy: In-vivo verification of the ion-beam range by means of positron imaging *Nuclear Physics A* **701** 224c-52c
- Kanazawa M, et al. 2004a Secondary beam course for medical use at HIMAC *NIRS-M(Nat Inst Radiol Sci)* **173** 189-90
- Kanazawa M, et al. 2004b Present status of secondary beam courses in HIMAC *Nuclear Physics A* **746** 393c-6c
- Kang J, Hong B H, An D H, Jung I S and Kang K U 2012 Magnet Design of the Superconducting Cyclotron for Carbon Therapy *IEEE Transactions on Applied Superconductivity* **22** 4401104
- Kempe J 2007 Absorbed dose and quality distribution in light ion radiation therapy with  $\beta^+$ -emitters. In: *Workshop of Heavy Charged particles in Biology and Medicine*, , (Heidelberg, Germany) p 110
- Kempe J 2008 Development of analyticla transport methods for biologically optimized light ion therapy, PhD thesis, Medical Radiation Physics, Stockholm University
- Kempe J and Brahme A 2008 Energy-range relation and mean energy variation in therapeutic particle beams *Med. Phys.* **35** 159-70
- Kempe J and Brahme A 2010a Analytical theory for the fluence, planar fluence, energy fluence, planar energy fluence and absorbed dose of primary particles and their fragments in broad therapeutic light ion beams *Physica Medica* **26** 6-16
- Kempe J and Brahme A 2010b Solution of the Boltzmann equation for primary light ions and the transport of their frgments *Physical Review Special Topics - Accelerators and Beams* **13** 104702-13
- Kempe J, Gudowska I and Brahme A 2007 Depth absorbed dose and LET distributions of therapeutic  $^{1}\text{H}$ ,  $^{4}\text{He}$ ,  $^{7}\text{Li}$ , and  $^{12}\text{C}$  beams *Med. Phys.* **34** 183-92
- Kitagawa A, Endo M, Hosaka M, Kanai T, Kanazawa M and Koda S 2001 Radioactive beam project at HIMAC. In: *Proceedings of the Second Asian Particle Accelerator Conference, Beijing, China*, pp 800-2
- Kitagawa A, et al. 2012 Status of ion sources at National Institute of Radiological Sciences *Review of Scientific Instruments* **83** 02A332
- Kraft G 2000 Tumortherapy with ion beams *Nucl. Instr. Meth. Phys. Res. A* **454** 1-10
- Lang C, Habs D, Parodi K and Thirolf P G 2013 Sub-millimeter nuclear medical imaging with reduced dose application in positron emission tomography using  $\beta\gamma$  coincidences *Pre-print*. (<http://arxiv.org/pdf/1305.4261.pdf>)

- Latysheva L N and Sobolevsky N M 2008 LOENT- the code for Monte Carlo simulation of neutron transport in complex geometries *INR RAS 1200/2008*
- Li Q, Furusawa Y, Kanazawa M, Kanai T, Kitagawa A, Aoki M, Urakabe E, Sato K and Wei Z 2006 Enhanced biological effect induced by a radioactive  $^{9}\text{C}$ -ion beam at the depths around its Bragg peak *Nucl. Instr. Meth. Phys. Res. B* **245** 302-5
- Li Q, Kanai T and Kitagawa A 2003 A model to evaluate the biological effect induced by the emitted particles from a  $\beta$ -delayed particle decay beam *Phys. Med. Biol.* **48** 2971-86
- Lindhard L and Scharf M 1961 Energy dissipation by ions in the keV region *Phys. Rev.* **124** 128-30
- Lindroos M 2004 Review of ISOL-type radioactive beam facilities *Proc. EPAC04 Lucerne (Switzerland)* 45-9
- Litzenberg D W, Roberts D A, Lee M Y, Pham K, Vander Molen A M, Ronningen R and Beccetti F D 1999 On-line monitoring of radiotherapy beams: Experimental results with proton beams *Med. Phys.* **26** 992-1006
- Llacer J, Chatterjee A, Alpen E, Saunders W, Andreea S and Jackson H C 1984a Imaging by injection of accelerated radioactive particle beams *IEEE Transactions on Medical Imaging MI-3* 80-90
- Llacer J, Chatterjee A, Alpen E, Saunders W, Andreea S and Jackson H C 1984b Imaging by injection of accelerated radioactive particle beams *IEEE Trans. on Nucl. Sci. MI-3* 80-90
- Llacer J, Chatterjee A, Jackson H C, Lin J C and Zunzunegui M V 1979 An imaging instrument for positron emitting heavy ion beam injection *IEEE Trans. on Nucl. Sci. NS-26* 637-47
- Ma C C M 2012 *Proton and carbon ion therapy*, ed C C-M Ma and T Tony Lomax (CRC press) pp 1-12
- Mancusi D, et al. 2009 Calculation of energy-deposition distributions and microdosimetric estimation of the biological effect of a  $^{9}\text{C}$  beam *Radiation and Environmental Biophysics* **48** 135-43
- Meierbachtol K, Morrissey D J, Mosby M and Bazin D 2012 Evolution of the momentum distribution with mass loss in projectile fragmentation reactions *Physical Review C* **85** 034608-6
- Min C H, Kim C H, Youn M Y and Kim J W 2006 Prompt gamma measurements for locating the dose falloff region in the proton therapy *Applied Physics Letters* **89** 183517
- Mizuno H, et al. 2003 Washout measurement of radioisotope implanted by radioactive beams in the rabbit *Phys. Med. Biol.* **48** 2269-81
- Morrissey D J 1989 Systematics of momentum distributions from reactions with relativistic ions *Phys Rev C* **39** 460-70
- Müller H and Enghardt W 2006 In-beam PET at high-energy photon beams: a feasibility study *Phys. Med. Biol.* **51** 1779
- Müzenberg G 1992 The separation techniques for secondary beams *Nucl. Instr. Meth. Phys. Res. B* **70** 265-75
- Nishio T, Sato K, Kitamura H, Murakami K and Ogino T 2005 Distributions of  $\beta^+$  decayed nuclei generated in the CH<sub>2</sub> and H<sub>2</sub>O targets by target nuclear

- fragment reaction using therapeutic MONO and SOBP proton beam *Med. Phys.* **41** 1070-82
- Noda K, et al. 2011 Recent progress on new treatment research project at HIMAC *Nucl. Instr. Meth. Phys. Res. B* **269** 2924-7
- Noda K, et al. 2007 New accelerator facility for carbon-ion cancer-therapy *J. Radiat. Res.* **48** Suppl. A43-A54
- Noda K, et al. 2000 Electron cooler for medical and other application at HIMAC *Nucl. Instr. Meth. Phys. Res. A* **441** 159-66
- Nummela S, Dendooven P, Heikkilä P, Huikari J, Nieminen A, Jokinen A, Rinta-Antila S, Rubchenya V and Äystö J 2002 Wien filter for cooled low-energy radioactive ion beams *Nucl. Instr. Meth. Phys. Res. A* **481** 718-30
- Oelfke U, Lam G K Y and Atkins M S 1996 Proton dose monitoring with PET: quantitative studies in Lucite *Phys. Med. Biol.* **41** 177-96
- Parodi K 2004 On the feasibility of dose quantification with in-beam PET data in radiotherapy with  $^{12}\text{C}$  and proton beams, PhD thesis, University of Dresden
- Parodi K 2012 PET monitoring of hadrontherapy *Nuclear Medicine Review* **15** C37-C42
- Parodi K and Bortfeld T 2006 A filtering approach based on Gaussian-powerlaw convolutions for local PET verification of proton radiotherapy *Phys. Med. Biol.* **51** 1991-2009
- Parodi K, Bortfeld T and Haberer T 2008 Comparison between in-beam and offline positron emission tomography imaging of proton and carbon ion therapeutic irradiation at synchrotron- and cyclotron-based facilities *International Journal of Radiation Oncology Biology Physics* **71** 945-56
- Parodi K and Enghardt W 2000 Potential application of PET in quality assurance of proton therapy *Phys. Med. Biol.* **45** N151-N6
- Parodi K, Enghardt W and Haberer T 2002 In-beam PET measurements of  $\beta^+$  radioactivity induced by proton beams *Phys. Med. Biol.* **47** 21-36
- Parodi K, et al. 2007 Patient study of in vivo verification of beam delivery and range, using positron emission tomography and computed tomography imaging after proton therapy *International Journal of Radiation Oncology Biology Physics* **68** 920-34
- Parodi K, Ponisch F and Enghardt W 2005 Experimental study on the feasibility of in-beam PET for accurate monitoring of proton therapy *IEEE Transactions on nuclear science* **52** 778-86
- Pawelke J, et al. 1996 The investigation of different cameras for in-beam PET imaging *Phys. Med. Biol.* **41** 279-96
- Ponisch F, Parodi K, Hasch B G and Enghardt W 2004 The modelling of positron emitter production and PET imaging during carbon ion therapy *Phys. Med. Biol.* **49** 5217-32
- Priegnitz M, Mockel D, Parodi K, Sommerer F, Fiedler F and Enghardt W 2008 In-beam PET measurement of  $^{7}\text{Li}^{3+}$  irradiation induced  $\beta^+$ -activity *Phys. Med. Biol.* **53** 4443-53
- Raju M R 1980 *Heavy particle radiotherapy* (Academic press)

- Remmeli S, Hesser J, Paganetti H and Bortfeld T 2011 A deconvolution approach for PET-based dose reconstruction in proton radiotherapy *Phys. Med. Biol.* **56** 7601-19
- Richard M H, et al. 2012 Design Study of the Absorber Detector of a Compton Camera for On-Line Control in Ion Beam Therapy *IEEE Transactions on nuclear science* **59** 1850-5
- Roellinghoff F, et al. 2011 Design of a Compton camera for 3D prompt- $\gamma$  imaging during ion beam therapy *Nucl. Instr. Meth. Phys. Res. A* **648** S20-S3
- Rossi B ed 1952 *High-energy particles* (New York Prentice-Hall, Incorporated)
- Schall I, et al. 1996 Charge-changing nuclear reactions of relativistic light-ion beams ( $5 \leq Z \leq 10$ ) passing through thick absorbers *Nucl. Instr. Meth. Phys. Res. B* **I17** 221-34
- Schardt D, Elsässer T and Schulz-Ertner D 2010 Heavy-ion tumor therapy: Physical and radiobiological benefits *Reviews of Modern Physics* **82** 384-426
- Schultz-Ertner D and Tsujii H 2007 Particle radiation therapy using proton and heavier ion beams *Journal of Clinical Oncology* **25** 953-64
- Schwender J 2011 Degree of Bachelor, KTH, School of Engineering Sciences (SCI), Stockholm (Sweden)
- Scifoni E, Tinganelli W, Weyrather W K, Durante M, Maier A and Kramer M 2013 Including oxygen enhancement ratio in ion beam treatment planning: model implementation and experimental verification *Phys. Med. Biol.* **58** 3871-95
- Shakirin G, Braess H, Fiedler F, Kunath D, Laube K, Parodi K, Priegnitz M and Enghardt W 2011 Implementation and workflow for PET monitoring of therapeutic ion irradiation: a comparison of in-beam, in-room, and off-line techniques *Phys. Med. Biol.* **56** 1281-98
- Shirai T, Furukawa T, Mizushima K and Noda K 2009 Cooling stacking experiments at HIMAC *Proceedings of the conference COOL09, Lanzhou (China)* 154-6
- Sihver L and Mancusi D 2009 Present status and validation of HIBRAC *Radiation Measurements* **44** 38-46
- Sihver L, Matthiä D, Koi T and Mancusi D 2008 Dose calculations at high altitudes and in deep space with GEANT4 using BIC and JQMD models for nucleus-nucleus reactions *New Journal of Physics* **10** 105019
- Sihver L, Tsao C H, Silberberg R, Kanai T and Barghouty A F 1993 Total reaction and partial cross section calculations in proton-nucleus ( $Z_t \leq 26$ ) and nucleus-nucleus reactions ( $Z_p$  and  $Z_t \leq 26$ ) *Phys Rev C* **47** 1225-36
- Sobolevsky N 2011 Personal Communication
- Sommerer F, Cerutti F, Parodi K, Ferrari A, Enghardt W and Aiginger H 2009 In-beam PET monitoring of mono-energetic  $^{16}\text{O}$  and  $^{12}\text{C}$  beams: experiments and FLUKA simulations for homogeneous targets *Phys. Med. Biol.* **54** 3979-96
- Staaf J 2013 Personal Communication
- Straåt S, Andreassen B, Jonsson C, Noz M E, Maguire Jr G Q, Nafstadius P, Naslund I, Schoenahl F and Brahme A 2013a Clinical application of in vivo treatment delivery verification based on PET/CT imaging of positron

- activity induced at high energy photon therapy *Phys. Med. Biol.* **58** 5541–53
- Straåt S, Jacobsson H, Noz M E, Andreassen B, Näslund I and Jonsson C 2013b Dynamic PET/CT measurements of induced positron activity in a prostate cancer patient after 50-MV photon radiation therapy *EJNMMI Research* **3** 1-7
- Straåt S J 2012 Verification of high energy photon therapy based on PET/CT imaging of photonuclear reactions, PhD thesis, Medical Radiation Physics Department, Stockholm University (Sweden)
- Suda M, et al. 2000 Medical application of the positron emitter beam at HIMAC *Proceedings of the conference EPAC2000, Vienna (Austria)* 2554-6
- Tanabe T, et al. 1991 Electron cooling experiments at INS *Nucl. Instr. Meth. Phys. Res. A* **307** 7-25
- Tarasov O B 2004 Analysis of momentum distribution of projectile fragmentation products *Nuclear Physics A* **734** 536
- Tashima H, Yamaya T, Yoshida E, Kinouchi S, Watanabe M and Tanaka E 2012 A single-ring OpenPET enabling PET imaging during radiotherapy *Phys. Med. Biol.* **57** 4705–18
- Testa E, Bajard M and Chevallier M 2009 Dose profile monitoring with carbon ions by means of prompt-gamma measurements *Nucl. Instr. Meth. Phys. Res. B* **267** 993-6
- Testa M 2011 Physical measurements for ion range verification in charged particle therapy, PhD thesis, University of Lyon (France)
- Testa M, et al. 2010 Real-time monitoring of the Bragg-peak position in ion therapy by means of single photon detection *Radiat. Environ. Biophys.* **49** 337-43
- Tobias C A 1985 The future of heavy-ion science in biology and medicine *Radiation Research* **103** 1-33
- Tobias C A, Benton B E, Capp M P, Chatterjee A, Cruty M R and Henke R P 1977 Particle radiography and autoactivation *International Journal of Radiation Oncology Biology Physics* **3** 33-44
- Tobias C A, Chatterjee A and Smith A R 1971 Radioactive fragmentation of N<sup>7+</sup> ion beam observed in beryllium target *Phys. Lett. A* **37** 119-20
- Tobias C A, Lawrence J H, Born J L, McCombs R K, Roberts J E, Anger H O, Low-Bear B V A and Huggins C B 1958 Pituary Irradiation with High-Energy Proton Beams - A preliminary Report *Cancer Research* **18** 121-34
- Tomitani T 2013 Personal Communication
- Tomitani T, et al. 2003 Washout studies of <sup>11</sup>C in rabbit thigh muscle implanted by secondary beams of HIMAC *Phys. Med. Biol.* **48** 875–89
- Toneev V D and Gudima K K 1983 Particle emission in light and heavy ion reactions *Nucl. Phys. A* **400** 173-89
- TRS-461 2008 Relative Biological Effectiveness in Ion Beam Therapy *International Atomic Agency, Vienna*
- Tsujii H and Kamada T 2012 A review of update clinical results of carbon ion therapy *Japanese Journal of Clinical Oncology* **42** 670-85
- Tsujii H, et al. 2008 Clinical advantages of carbon-ion radiotherapy *New Journal of Physics* **10** 075009

- Van Goethem M J, Van Der Meer R, Reist H W and Schippers J M 2009 Geant4 simulations of proton beam transport through a carbon or beryllium degrader and following a beam line *Phys. Med. Biol.* **54** 5831-46
- Ward J F 1998 Nature of Lesions Formed by Ionizing Radiation *DNA Damage and Repair Contemporary Cancer Research* **2** 65-84
- Vavilov V P 1957 Ionization losses of high-energy heavy particles *Soviet Physics JETP* **5** 749-51
- Wien K 1999 100 years of ion beams: Willy Wien's canal rays *Brazilian Journal of Physics* **29** 401-14
- Wilson R R 1946 Radiological use of fast protons *Radiology* **47** 487-91
- Yamaya T 2013 Personal Communication
- Yamaya T and Inaniwa T 2010 OpenPET: a new geometry enabling PET imaging during radiation therapy. In: *Proc. Japanese-European Joint Symp. on Ion Cancer Therapy and NIRS-KI Joint Symp. on Ion-Radiation Sciences (Stockholm, Sweden)* pp 129–33
- Yamaya T, et al. 2011 Development of a small prototype for a proof-of-concept of OpenPET imaging *Phys. Med. Biol.* **56** 1123-37
- Yamaya T, et al. 2012a A small prototype of a single-ring OpenPET *IEEE Nuclear Science Symposium and Medical Imaging Conference Record (NSS/MIC)* 2205-007
- Yamaya T, et al. 2012b Washout effects in rats during in-beam imaging by small Open PET prototype *The Journal of Nuclear Medicine* **53** 490